Microwave whispering-gallery resonators for nanolitre liquid sensing

Dissertation zur Erlangung des akademischen Doktorgrades in Physik

vorgelegt der

Fakultät für Physik der Technischen Universität Dortmund

von

Olena N. Shaforost

Januar 2009

angefertigt im:
Forschungszentrum Jülich
Institut für Bio- und Nanosysteme

Betreuer:
Priv. Doz. Dr. Norbert Klein

Zusammenfassung

Im Rahmen dieser Dissertation wurde ein neues Verfahren zur Untersuchung von wässrigen Lösung mit elektromagnetischer Strahlung im Mikro- und Millimeterwellenbereich entwickelt, dass eine hohe Relevanz für biologische Anwendungen aufweist. Whispering-Gallery-Moden in kreiszylinderförmigen dielektrischen Scheiben aus verlustarmen einkristallinen Materialien wie Saphir oder Quartz ermöglichen sehr hohe Gütefaktoren, weil die elektromagnetischen Felder sehr stark im Inneren der Zylinder konzentriert sind, und Abstrahlungsverluste vernachlässigbar sind. Basierend auf diesem Resonatortyp wurden drei verschiedene Ansätze zur Flüssigkeitssensorik entwickelt, analysiert und im Hinblick auf die Bestimmung der komplexen dielektrischen Permittivität von Flüssigkeiten optimiert.

Als erste Methode wurden Whispering-Gallery-Resonatoren aus Saphir für den Frequenzbereich 35-37 Gigahertz für Untersuchungen an kleinen Tropfen aus biochemischen Flüssigkeiten entwickelt und optimiert, die Volumina der Tropfen liegen im Bereich von 100 Pikoliter bis hin zu einigen Nanoliter. Mit Hilfe eines mit einer Genauigkeit von einigen Mikrometer verstellbaren Mikroinjektionssystems konnten die zu untersuchenden Tropfen an beliebigen Stellen auf die Oberfläche des Saphir-Resonators appliziert werden. Das an der Oberfläche vorhandenen evaneszente Feld führt zu einer durch den Tropfen induzierten Reduktion des Gütefaktors und zu einer Änderung der Resonanzfrequenz, die von der komplexen Permittivität der Flüssigkeit abhängen. Die optimale Tropfenposition auf der Resonatoroberfläche, die dem Maximum der elektrischen Feldstärke entspricht, wurde experimentell ermittelt.

Es wurden zwei Möglichkeiten der Resonatoranregung für Frequenzen im Ka – Band (26.5 – 40 Gigahertz) untersucht und optimiert. Zum einen wurden die Resonatoren in halboffenen Metallgehäusen angeordnet, und es wurden stehwellenartige Whispering-Gallery-Moden mit Hilfe von in der Gehäusewand fixierten koaxialen Koppelschleifen angeregt. Als zweite Methode wurden laufwellenartige Whispering-Gallery-Moden in Resonatoren ohne Abschirmgehäuse durch dielektrische „image guide“- Wellenleiter angeregt. Im Vergleich zu den stehwellenartigen Resonanzen besteht der Vorteil darin, dass die elektrische Feldstärke nahezu unabhängig vom Azimuthwinkel ist, was die Positionierung der Tropfen erheblich erleichtert. Weiterhin ist es vorteilhaft, dass dieses Anregungsschema auch für höhere Frequenzen bis in dem Terahertzbereich verwendet werden kann. Als erste Demonstration wurden auf diese Weise Whispering-Gallery-Resonanzen in Quartzscheiben bei einer Frequenz von 170 Gigahertz angeregt, die erzielten Gütefaktoren betragen etwa 30.000.

Die experimentellen Resultate bezüglich der durch die Tropfen verursachten Änderung der Resonanzfrequenz und des reziproken Gütefaktors zeigen eine quantitative Übereinstimmung mit den Ergebnissen einer Störungsrechnung in Verbindung mit numerischen Feldsimulationen für den ungestörten Resonator. Insbesondere lassen sich die durch den Real- und Imaginärteil der komplexen dielektrischen Permittivität verursachten Effekte voneinander separieren. Beide Messgrößen weisen – entsprechend den Vorhersagen der Störungsrechnung – eine nahezu lineare Abhängigkeit vom Tropfenvolumen auf.

Aufgrund der hohen Gütefaktoren konnten Tropfen bis zu 100 Pikoliter Volumen mit dieser Methode untersucht werden.

Tropfen aus destillierten Wasser wurden mit Tropfen aus wässrigen Lösungen von Äthanol, Natriumchlorid, Glukose und Albumin verglichen. Für alle gelösten Substanzen ergaben sich signifikante Unterschiede zu Wasser für Konzentrationen oberhalb von 5%. Mit Hilfe von Störungsrechnungen konnte gezeigt werden, dass das vom Tropfenvolumen nahezu unabhängige Verhältnis von Frequenzverschiebung und Änderung des reziproken Gütefaktors proportional zum dielektrischen Verlusttangens der Flüssigkeit ist. Da letzterer proportional zur Relaxationszeit für die Orientierungspolarisation der molekularen Dipole ist, die bei wässrige Lösungen organischer Moleküle mit zunehmender Konzentration der Lösungen zunimmt, stellen hochgenaue Konzentrationsmessungen eine interessante Perspektive für die Whispering-Gallery-Resonatormethode dar.

Als erster Schritt in Richtung einer praktischen mikrofluidischen Sensoranwendung wurden - als zweite Messanordnung - Whispering-Gallery-Resonanzen in einer Saphirscheibe bei 11 Gigahertz untersucht. Dazu wurde eine „Flipchip“- Konfiguration bestehend aus einer Quartzscheibe, die mit einer Bohrung zu Aufnahme von 400 Nanoliter Testflüssigkeit versehen war, und der Saphirscheibe eingesetzt, um hochgenaue Messungen an Flüssigkeiten durchzuführen. Die durchgeführten Kalibriermessungen an unterschiedlichen Flüssigkeiten ermöglichen es, mit dieser Methode den Real- und Imaginärteil der dielektrischen Permittivität über einen weiten Wertebereich zu bestimmen, entsprechend den Erwartungen aus der Störungstheorie. Aufgrund des hohen Gütefaktors von mehr als 100.000 für den ungestörten Resonator stellte sich die durch die Flüssigkeit verursachte Änderung des reziproken Gütefaktors als ein direktes Maß für die Relaxationszeit heraus. Aus der Messung der Temperaturabhängigkeit ergab sich die korrekte Temperaturabhängigkeit der Relaxationszeit von Wasser, die durch thermische Anregung bestimmt ist. Es wurde gezeigt, dass sich mit dieser Methode die Konzentration von wässrige Glucoselösungen mit 0.2 % Auflösung bestimmen lässt.

Als dritte Messanordnung, die auf eine Referenzmethode für die Bestimmung der komplexen dielektrischen Permittivität von Flüssigkeiten abzielt, wurde eine sog. „radially-two-layered“-Struktur, die aus einem dielektrischen Ring besteht, der zwischen zwei hochleitenden Metallplatten eingeklemmt ist, untersucht. Die zu untersuchende Flüssigkeit wird dabei ins Innere des dielektrischen Rings, der aus Saphir besteht, gefüllt, so dass die Flüssigkeit einen dielektrischen Zylinder ausbildet, der die gleiche Höhe wie der Saphirring aufweist. Für solche Whispering-Gallery-Moden, bei denen das elektrische Feld parallel zur Zylinderachse verläuft, reduziert sich die Wellengleichung sowohl für den leeren als auch für gefüllte Resonator zu einer eindimensionalen transzendenten Gleichung, so dass die komplexe Permittivität aus dem Modenspektrum und den Gütewerten mit hohen Genauigkeit und ohne Kalibrierung bestimmt werden kann. Bei dieser Methode, die für Frequenzen von 36-38 Gighertz entwickelt wurde, ist ein Flüssigkeitsvolumen von weniger als einem Milliliter erforderlich. Messungen mit dieser Technik sowie breitbandige Messungen mit einer Koaxialsonde wurden als Referenzmessungen für die Charakterisierung wässrigen Flüssigkeiten eingesetzt. Die Resultate wurden mit den Experimenten an Tropfen

(35-37 Gigahertz) und den Messungen mit der Flip-Chip Konfiguration bei 11 Gigahertz verglichen.

Zusammenfassend gesagt, wurde im Rahmen dieser Dissertation eine neues Verfahren zur hochempfindlichen Analyse von Flüssigkeiten mit Volumina im Nanoliterbereich entwickelt und verifiziert. Daraus ergeben sich herausfordernde Perspektiven für Sensoranwendungen in den Bereichen Chemie, Biologie und Medizin.

Abstract

Within this thesis, a novel approach for the investigation of aqueous solutions interacting with electromagnetic radiation at micro-to-millimetre wave frequencies was developed and employed with relevance to biological applications. Whispering-gallery modes in cylindrically shaped dielectric disks machined from low-loss single crystalline materials such as sapphire or quartz allow for very high quality factors, because the electromagnetic fields are strongly confined inside the dielectric disk such that radiation losses can be neglected. Based on this resonator type, three different liquid sensing approaches were developed, analysed and optimized with emphasis on the determination of the complex dielectric permittivity of liquids.

As a first method, whispering-gallery sapphire resonators at 35-37 gigahertz were developed and optimized for the investigation of small droplets of biochemical liquids with volumes ranging from 100 picolitres up to about a few nanolitres. Employing a micrometer controlled microinjection system, droplets could be spotted at arbitrary positions on the surface of the sapphire disk. At the surface of the disk, an evanescent field emerges, such that the droplet induces a slight change of the resonance frequency and a reduction of the inverse quality factor depending on complex dielectric permittivity of the liquid under test. The optimum spotting position on the resonator surface corresponding to the maximum electric field was determined experimentally.

Two types of resonator excitation schemes were investigated and optimized for the Ka frequency band (26.5 – 40 Gigahertz). At first, resonators were embedded in a semi-open metal shielding cavity and excited in a standing wave regime by coaxial loop antennas fixed at the walls of the cavity. Secondly, dielectric disks without shielding cavity were investigated, comprising excitation of whispering-gallery running waves by dielectric image guides. In contrast to standing wave loop excitation, the electric field strength of the running whispering gallery waves is nearly independent of the azimuthal angle, which is of great advantage for the positioning of very small samples. In addition, this scheme can be extended up to the terahertz frequency range. As a first demonstration, whispering gallery resonances were excited in a quartz disk resonator at 170 Gigahertz with quality factors of order of 30000.

The results on droplet induced changes of resonant frequency and inverse quality factor were found to be in quantitative agreement with perturbation theory in conjunction with numerical field simulation of the unperturbed resonator. In particular it was found, that the effect of real and imaginary part of permittivity could be separated. Both measured quantities were found to be nearly linear dependent on the droplet volume, as expected by perturbation theory. Due to the very high quality factor, droplets down to 100 picoliters volume could be analysed by this technique.

Droplets of distilled water were compared with aqueous solutions of ethanol, sodium chloride, glucose and albumin. For all solutes, the measured results were clearly different from water for concentrations above 5%. Within perturbation theory it was found, that the ratio of droplet induced change of inverse quality factor and droplet induced frequency shift,

being nearly independent of the droplet volume, is proportional to the loss tangent of the liquid. Since the loss tangent is proportional to the relaxation time of orientational polarisation of the molecular dipoles, which decreases with increasing concentration in aqueous solution of organic molecules, the whispering gallery mode resonator method provides an interesting perspective for accurate concentration determination of highly diluted aqueous solutions.

As a first step towards practical microfluidic sensor applications, a second measurement scheme based on whispering gallery resonances in a sapphire disk at a frequency of 11 Gigahertz was investigated. A flip-chip configuration composed of a thin quartz disk with a small hole filled with 400 nanolitres of a test liquid and the sapphire resonator disk was employed for highly accurate measurement on liquids. Calibration measurements on various test liquids enable the determination of real and imaginary parts of dielectric permittivity over a wide range of values, in accordance with analysis by perturbation theory. Due to the high quality factor of the unperturbed resonator of more than 100 000, the measured liquid induced change of the resonant amplitude was found to be proportional to the relaxation time. Temperature dependent measurements revealed the correct temperature dependence of the relaxation time due to thermal excitation. It was found, that the concentration of aqueous solutions of glucose can be resolved with an accuracy of 0.2 % by this technique.

As third approach aiming towards a reference method for permittivity measurements, the so-called radial-two-layered resonator structure composed of a dielectric ring clamped between two highly conducting metal plates was investigated. The liquid under test was filled inside the dielectric ring machined from sapphire, such that a liquid cylinder of the same height as the ring emerges. For those types of whispering gallery modes comprising electric fields parallel to the cylinder axis, the wave equation for the empty and the filled resonator reduces to a one dimensional algebraic transcendental equation, such that the complex permittivity could be calculated from the mode spectrum and quality factors with high accuracy without any calibration. This method developed for frequencies of 36-38 Gigahertz requires a liquid volume of less than one millilitre. Measurements by this techniques plus additional coaxial probe broadband measurements up to 20 Gigahertz were applied as reference methods for the characterizing of aqueous liquids. The results were compared both with the nanolitre droplet experiments (35-37 Gigahertz) and with measurements at 11 Gigahertz performed with the flip-chip configuration.

In summary, by this thesis a novel approach for highly sensitive liquid analysis for volumes in the nanolitre range has been developed and verified, with challenging perspectives for practical sensor applications in chemistry, biology and medicine.

Introduction

Electromagnetic waves are a common tool for spectroscopic investigation of solid, liquid and gaseous materials with a wide range of applications in physics, chemistry and life science, but also for security systems, process and quality control and inspection of food and pharmaceutical products [1]. From the lowest bands at kilohertz frequencies towards gamma radiation, various properties can be probed. In case of molecular samples, the kilohertz – to – gigahertz frequency bands in conjunction with magnetic fields yield structural information by nuclear magnetic resonance (NMR) spectroscopy. Infrared and Raman spectroscopy yield detailed information on individual chemical bonds [2], optical and UV spectroscopy on electronic excitations mostly for the individual atoms, and x-rays on the average atomic numbers, mass density and molecular structure [3]. The range between about one gigahertz and a few terahertz is very specific to collective excitations of a substance: between about five hundred gigahertz and five terahertz the observation of collective vibrational modes of the molecular solids reveals details of the molecular structure and chemical bonds [4]. At lower frequencies, for liquid samples the degree of freedom of molecular relaxation reveals information on the intermolecular forces and structure [5].

The investigation of liquids by electromagnetic waves in the micro- to millimeter wave bands represents a great challenge for the fundamental understanding of their dielectric and conducting properties. The structure of its molecular components, their intermolecular bonds, and the electrical conductivity induced by dissolved ions expresses itself in the frequency and temperature dependence of the complex dielectric function, which contains a rich spectrum of information including various relaxation processes, orientational polarisation of the molecules, and frequency dependence of the ionic conductivity. For aqueous solutions, where the pronounced relaxation peak due to orientational polarization of molecular dipole formed by the water molecule leads to a strong absorption over the whole micro- and millimetre wave range [6], the observed deviations from the properties of pure distilled water – as the most relevant reference liquid [7], [8] – are very specific to the dissolved species, to their concentration, and modifications of the water itself as a result of the dissolving process.

Although broadband studies covering the largest possible frequency range represent the ultimate solution with emphasis on exploiting the full information included in the electromagnetic response of a liquid, the relative simplicity of the spectra allows to identify the main features of a spectrum by precise measurements at a few selected frequencies. In conjunction with the high losses imposed by the dipole relaxation for water in the higher microwave frequency bands above ten gigahertz, even extremely small amounts of liquids can be analyzed, provided that resonant systems of high quality factor can be utilized as sensing elements.

In the frame of this thesis, extremely sensitive approaches for the investigation of the dielectric properties of liquids in the frequency range from ten to forty gigahertz have been developed and analyzed, with a strong potential to be further extended for the terahertz range in the future. Cylindrically shaped dielectric resonators made from low-loss single crystals were developed, optimized and finally utilized for high precision measurements on liquids

down to volumes of picolitres. Employing so-called whispering gallery modes, the dielectric resonators can be operated in semi-open metallic shielding or even without any shielding. The evanescent fields occurring near the surface of the dielectric cylinders provide an ideal platform for the investigation of extremely small amounts of a liquid either as droplets or liquids in volumes defined by closed cavities, such as microfluidic systems. Due to the simplicity of the sensing arrangement, various applications ranging from concentration measurements on biological liquids such as glucose, monitoring of liquids in chemical, pharmaceutical and food industry, investigation of human tissue and investigation towards label free DNA analysis will become possible in the future.

This thesis is organized as follows: Chapter 1 provides a brief introduction to the theory of dielectric properties of matter with emphasis on liquids, including models to describe the static dielectric properties by the different mechanism of polarisation. A particular emphasis is devoted to models describing the dynamic complex dielectric function, which contains relaxation and conduction processes. Finally, the literature data base for water as a reference liquid is shortly reviewed.

In Chapter 2, an overview about microwave methods to measure the dielectric properties of liquids is given with emphasis on narrowband resonant and broadband transmission line or free space techniques. The broadband techniques can be operated both in time and frequency domain.

In Chapter 3 the applied method of whispering gallery resonators as sensing element for the investigation of liquids is introduced. Two approaches are discussed in details and their accuracy and sensitivity is analyzed: One approach to perform reference measurement on liquids based on a specially designed resonator / liquid cell geometry being made such that a rigorous solution of Maxwell's equations can be utilized to deduce the complex permittivity of the test liquid directly from the resonator characteristics. The other approach is about measurements on droplets down to 100 picolitres volume, the analysis is based on a combination of numerical field simulations in conjunction with electromagnetic perturbation theory.

Chapter 4 deals with results in aqueous solution of ethanol, NaCl, glucose and albumin by the two whispering gallery mode techniques described in Chapter 3. The application of rigorous solution on the one hand and perturbation technique on the other hand indicates the measuring capability of the approaches. In particular, the analytical capability for the investigation of nanolitre droplets is clearly demonstrated.

In Chapter 5, a first WGM based sensing system realized by a combination of a WGM resonator with a microfluidic quartz wafer is demonstrated, which can be calibrated to determine the complex dielectric permittivity of a 400 nl liquid sample at frequency around 10 GHz. Based on highly sensitive measurements of changes of the resonator losses, the concentration of extremely diluted solutions of organic molecules in water can be determined. As an approach towards terahertz integrated WGM resonator biosensors, first numerical fields simulations on resonator arrays and experiments on WGM resonators at 170 GHz will be discussed.

Chapter 1: Theoretical aspects of dielectric response in liquid media

In this thesis, the interaction of electromagnetic radiation in the microwave range with liquids is investigated. The microwave spectrum extends from a frequency f of 1 GHz to 300 GHz, the corresponding wavelength λ ranges from 30 cm to 1 mm. The microwave range includes centimeter waves (f = 3 — 30 GHz, λ = 10 — 1 cm) and millimeter waves (f = 30 — 300 GHz, λ = 10 — 1 mm. The most developed range for a large variety of applications lies within the 1 to 40 GHz range. Frequency and wavelength are connected by

$$c = \lambda \cdot f \tag{1.1}$$

with c being equal to the velocity of light, which is $2.998 \cdot 10^8$ m/s for propagation in vacuum.

The existence of electromagnetic radiation spectrum was predicted by J.C. Maxwell, who defined the visible light to be only a particular case of the variety of electromagnetic waves in nature which have all other possible frequencies. In 1864 Maxwell proposed a system of partial differential equations, which are the general basis to describe the propagation of electromagnetic waves in media and to analyze the experimental results.

1.1 Maxwell's equations in a linear medium

In their differential form, the Maxwell equations are given by:

$$\vec{\nabla} \times \vec{E} = -\frac{\partial \vec{B}}{\partial t} \qquad \vec{\nabla} \vec{B} = 0 \qquad \vec{\nabla} \times \vec{H} = \frac{\partial \vec{D}}{\partial t} + \vec{j} \qquad \vec{\nabla} \vec{D} = \rho \tag{1.2}$$

In these equations $\boldsymbol{E}$ and $\boldsymbol{H}$ are the electric and magnetic field strengths, $\boldsymbol{D}$ is the dielectric displacement due to the polarization of the material exposed to the field (the effective electric field inside a dielectric material) and $\partial \boldsymbol{D}/\partial t$ is the corresponding displacement current, $\boldsymbol{B}$ is the magnetic induction, $\boldsymbol{j}$ is the electric current density due to charge transport, and ρ is the electric charge density. The cited equations are different compared to Maxwell's equations in vacuum; consequently with electric displacement $\boldsymbol{D}$ instead of the electric field strength $\boldsymbol{E}$, and magnetic induction $\boldsymbol{B}$ associated with the magnetic field strength $\boldsymbol{H}$, being introduced to account for modifications by the medium. These macroscopic quantities describe averaged microscopic material properties such as electric dipoles, magnetic moments, polarization charges, and moving charges.

The effective electric field of a linear dielectric medium is composed of the electric field strength $\boldsymbol{E}$ and the induced electrical polarization $\boldsymbol{P}$ by

$$\vec{D} = \varepsilon_0 \vec{E} + \vec{P} = \varepsilon_0 \vec{E} + \chi_e \varepsilon_0 \vec{E} = \varepsilon_0 (1 + \chi_e) \vec{E} = \varepsilon_0 \varepsilon_r \vec{E} \tag{1.3}$$

where $\varepsilon_0 = 8.854 \cdot 10^{-12}$As/Vm is the permittivity of the vacuum, χ_e is the dielectric susceptibility of the medium, and $\varepsilon_r = 1 + \chi_e$ is the relative dielectric constant of a dielectric

medium. As it will be explained in this chapter, the complex frequency dependent function $\varepsilon^*(\omega)=\varepsilon_0 \cdot \varepsilon_r(\omega)$ is called dielectric function of complex electrical permittivity of the medium.

Correspondingly, the magnetic field strength $\boldsymbol{H}$ is connected to the magnetic induction $\boldsymbol{B}$ by the permeability μ

$$\vec{B} = \mu_0 \vec{H} + \vec{M} = \mu_0 \vec{H} + \chi_m \mu_0 \vec{H} = \mu_0 (1 + \chi_m) \vec{H} = \mu_0 \mu_r \vec{H} \tag{1.4}$$

where $\mu_0 = 1.256 \cdot 10^{-6}$ Vs/Am is the permeability of the vacuum, $\boldsymbol{M}$ is the magnetization vector, χ_m is the magnetic susceptibility of the medium, and $\mu_r = 1 + \chi_m$ is the relative permeability of a magnetic medium.

One more equation is assumed to apply, which describes Ohm's law, i.e. current density proportional to the electric field $\boldsymbol{E}$

$$\vec{j} = \sigma \vec{E} \tag{1.5}$$

where σ is the conductivity of the material (in units of Ωm).

The relations (1.3), (1.4), and (1.5) are so-called constitutive relations which are taken from molecular theories of polarization, magnetism and electrical conductivity of the media. In the following, we limit ourselves to the linear response; ε, μ, and σ do not depend on the electromagnetic field strength. For dielectric materials, except ferroelectrics, this holds true up to moderate field levels. As it will be discussed later, heating by dissipation occurs at much lower field level than any nonlinearity will appear.

In general, μ and ε are 2nd order tensors (explicitly for any anisotropic crystal), but in homogenous isotropic media such as liquids they can be simplified to be scalar. Energy dissipation due to conducting ions, molecular reorientation, kinetic processes, etc., which occur in the sample, can be represented with the help of complex field vectors $\boldsymbol{E}$, $\boldsymbol{D}$, $\boldsymbol{H}$, $\boldsymbol{B}$ and $\boldsymbol{P}$. In general form, the material properties are then represented with help of frequency-dependent complex permittivity, permeability and conductivity.

$$\varepsilon^*(\omega) = \varepsilon'(\omega) - i\varepsilon''(\omega) \quad \mu^*(\omega) = \mu'(\omega) - i\mu''(\omega) \quad \sigma^*(\omega) = \sigma'(\omega) - i\sigma''(\omega) \tag{1.6}$$

In case of μ and ε, their frequency-dependent real (subscript′) and imaginary parts (subscript″) correspond to the dispersion and absorption of electromagnetic energy in the sample when it is subjected to a field of angular frequency $\omega=2\pi f$.

For metals, the frequency dependence of specific conductivity is very small and can be satisfactory approximated by neglecting of the imaginary part of $\sigma^*(\omega)$, $\sigma''(\omega)=0$. σ'' is non zero only for the case of the superconductive state and for normal conducting metals at very high frequencies [9]. Magnetic materials such as iron (ferrites), cobalt, nickel and their alloys have appreciable magnetic properties. For the liquids investigated in this thesis the relative permeability is very close to unity, and μ will be equal to μ_0 throughout this work. All the liquids under investigation have dielectric properties and – some of them – conducting properties.

1.2 The wave equation in isotropic lossy dielectric media

In case of charge and current density being equal to zero, Maxwell equations yield the wave equation:

$$\vec{\nabla}^2\begin{pmatrix}\vec{E}\\ \vec{H}\end{pmatrix}-\frac{1}{c^2}\frac{\partial^2}{\partial t^2}\begin{pmatrix}\vec{E}\\ \vec{H}\end{pmatrix}=\left(\frac{d^2}{dx^2}+\frac{d^2}{dy^2}+\frac{d^2}{dz^2}-\frac{1}{c^2}\frac{\partial^2}{\partial t^2}\right)\begin{pmatrix}\vec{E}\\ \vec{H}\end{pmatrix}=0 \tag{1.7}$$

where $\boldsymbol{E}= \boldsymbol{E}_0\exp(-i\omega t)$ and $\boldsymbol{H}= \boldsymbol{H}_0\exp(-i\omega t)$ describe time harmonic electric and magnetic fields with angular frequency ω.

For a wave propagating in vacuum in *z*-direction the fields are proportional to $\exp[i(k_z z-\omega t)]$, such that only a differential equation for the transverse coordinates *x* and *y* remains.

$$\left[(\frac{\partial^2}{\partial x^2}+\frac{\partial^2}{\partial y^2}-k_z{}^2)+k_0{}^2\right]\begin{pmatrix}\vec{E}\\ \vec{H}\end{pmatrix}=0 \tag{1.8}$$

In case of a plane wave the fields do not vary in *x* and *y* direction, hence $k_z = k_0 = \omega/c$. In case of a waveguide with *z*-independent cross section, Eq. (1.8) has to be solved to find the eigenvalues $k_x^{m,n}$ and $k_y^{m,n}$ in case of Cartesian coordinates *x*,*y*,*z* or $k_\rho^{m,n}$ in $k_\phi^{m,n}$ in case of cylindrical coordinates ρ, ϕ, *z* for the different propagation modes with integer indices *m*, *n*, taking into account the boundary conditions for the electric and magnetic fields at the waveguide walls. For this case the propagation constant is determined by

$$k_z=\sqrt{k_0{}^2-k_x^{m,n\,2}-k_y^{m,n\,2}} \tag{1.9}$$

(for Cartesian coordinates), indicating the existence of a cut-off frequency (k_z=0) for each propagation mode below which wave propagation is prohibited and a wavelength $2\pi/k_z$ being longer than the plane wavelength $2\pi/k_0$.

For a wave propagating in an isotropic lossy medium the generalized complex permittivity

$$\eta^*(\omega)=\varepsilon^*(\omega)-i\frac{\sigma}{\varepsilon_0\omega}\qquad \eta'(\omega)=\varepsilon'(\omega)\qquad \eta''(\omega)=\varepsilon''(\omega)-i\frac{\sigma}{\varepsilon_0\omega} \tag{1.10}$$

has to be considered, where the functions $\eta'(\omega)$ and $\eta''(\omega)$ represent the frequency dependence of global dispersion and absorption of the sample. In order to describe the losses of a wave propagating in a medium, often the loss tangent $\tan\delta$

$$\tan\delta(\omega)=\frac{\eta''(\omega)}{\eta'(\omega)}=\frac{\omega\varepsilon_0\varepsilon''(\omega)+\sigma}{\omega\varepsilon_0\varepsilon'(\omega)} \tag{1.11}$$

is used to describe power absorption. The resulting wave equation is

$$\left[\left(\frac{\partial^2}{\partial x^2} + \frac{\partial^2}{\partial y^2} - k_z{}^2 \right) + \eta * k_0{}^2 \right] \begin{pmatrix} \vec{E} \\ \vec{H} \end{pmatrix} = 0 \tag{1.12}$$

In case of a plane wave, the wave number k_z in Eq. (1.12) is replaced by the complex wavenumber $k_0 \cdot \eta^{*1/2}$ with respect to propagation in vacuum. Therefore, the plane solution corresponds to an exponentially damped sine wave:

$$\begin{pmatrix} \vec{E} \\ \vec{H} \end{pmatrix} \propto \exp(ik_0 \sqrt{\eta^*} z) = \exp(ik_0 nz) \cdot \exp(-k_0 \kappa z) \tag{1.13}$$

The quantity

$$\tilde{n} = \sqrt{\eta} = n + i\kappa \tag{1.14}$$

is the complex refractive index, with n being the usual refractive index and κ being the extinction coefficient, which describes the absorption length of a plane wave propagating in a lossy medium. The quantities n and κ are related to the real and imaginary part of the generalized complex permittivity by:

$$n = \sqrt{\frac{\sqrt{\eta'^2 + \eta''^2} + \eta'}{2}} \approx \sqrt{\eta'} \quad (\text{for } \eta'' << \eta') \tag{1.15}$$

and:

$$\kappa = \frac{\eta''}{\sqrt{2 \cdot (\sqrt{\eta'^2 + \eta''^2} + \eta')}} \approx \frac{1}{2} \frac{\eta''}{\eta'} = \frac{1}{2} \tan\delta \, (\text{for } \eta'' << \eta') \tag{1.16}$$

For a low-loss dielectric medium $\eta'' << \eta' \approx \varepsilon'$, the wavelength in a medium is reduced by the square root of permittivity with respect to the vacuum, and the absorption length is roughly given by 2 times the wavelength divided by the loss tangent, for example 200 times λ in case of $\tan\delta$ = 0.01. In case of water in the frequency range of our investigation (10-40 GHz), $\tan\delta$ is close to unity, such that the exact formulas (Eq. (1.15) and (1.16)) have to be employed for the calculation of wavelength and absorption length.

In case of a filled or partially filled dielectric waveguide a rigorous solution of the wave equation leads to explicit dependences of the complex propagation constant k_z on the generalized complex permittivity.

1.3 Theoretical models for the static permittivity of liquids

In this section we describe theoretical models for the complex dielectric function of liquids. In contrast to solids, the molecules have the degree of freedom of rotation, which is of particular importance for liquids composed of polar molecules such as water. Therefore,

relaxation phenomena occur at microwave frequencies, which are very specific for the molecular composition of the individual liquid.

At first, non-conducting liquids are considered, i.e. liquids with negligible influence of conducting ions. In this case, the generalized complex permittivity is η^* equal to the complex permittivity ε^*. The effect of conducting ions is partially accounted for by Eq. (1.10), however, as discussed in [10], the presence of ions also induces a significant alteration of the complex dielectric function $\varepsilon(\omega)$ of the liquid.

On a microscopic level, the individual electric dipole moment $\boldsymbol{p}$ of each molecule contributes to the macroscopic electric polarization $\boldsymbol{P}$ of the liquid. The interaction of the alternating electric field with the dipole moments of each molecule, which also depends on the intermolecular forces, determines the complex dielectric function of the liquid.

In case of a liquid composed of only one species of molecules, the macroscopic polarization is related to the dipole moment of the individual molecule $\boldsymbol{p}$ by

$$\vec{P} = N\langle \vec{p} \rangle \tag{1.17}$$

where N is the number of molecules per volume. The time averaging of the dipole moment is rather important, because it implies the statistical effects of the thermal motion of molecules and provides information on the timescale of molecular relaxation upon reorientation, which is enforced by the applied alternating electric field.

In general, a molecular dipole moment can be described as

$$\vec{p} = \int \vec{r}\rho(\vec{r})d^3r, \tag{1.18}$$

with $\rho(\boldsymbol{r})$ being the molecular charge distribution. For the simplified case of two isolated point charges $+q$ and $-q$ separated by a vector $\boldsymbol{l}$, Eq. (1.18) becomes following

$$\vec{p} = q\vec{l} \tag{1.19}$$

Induced polarization

Neglecting the effects of orientational polarization, the two physical effects contributing to the dipole moment of the molecule are, stretching and rotation. Polarization only by **stretching** occurs for *non-polar molecules*. Non-polar molecules are molecules where the "centers-of-gravity" of the negative and positive charges are at the same point (see Fig. 1.1 (a)). In absence of an applied field non-polar molecules do not possess a dipole moment.

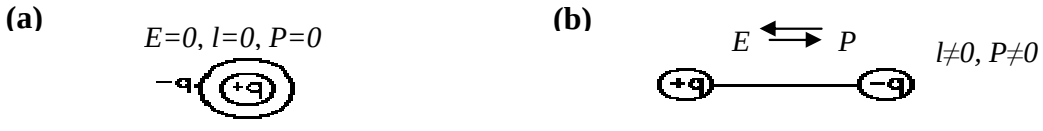

Figure 1.1 Polarization by stretching (a) without and (b) with applied electric field *E*.

When the molecule is subjected to an electric field, an electronic re-distribution occurs in the molecule due to a slight displacement of the electron orbitals. This effect is called *electronic polarization*. In contrast, *atomic polarization* occurs when the positively charged nucleus of an atom are displaced. In molecules, since the degree of displacement depends on the electronic environment of the individual atom, the effect of atomic polarization is to stretch, compress, or bend chemical bonds. Atomic and electronic polarization possess different relaxation times.

Polar molecules, like water, are molecules which possess a permanent dipole moment due to the natural non-uniform distribution of electrons. Because of the asymmetric structure, the centers-of-gravity of the negative and positive charges are not at the same place. Therefore, the polar molecules are already strongly stretched naturally; there exists a permanent charge separation within a polar molecule.

Without external field, the polar molecules in a liquid are randomly oriented. An applied electric field yields a polarization consisting of two parts: additional **stretching** of the molecule in an electric field (like for non-polar molecules) and **rotation.** Here, an applied electric field will polarize the material by orienting the dipole moments of polar molecules. The orientation process may involve an overall rotation of the molecule around its centre of mass; or, especially in long flexible molecules such as polymers, a charged section of a molecule which will be twisted with respect to neutral sections of the molecule. An overview of the dielectric response of polymers is given in [5].

Orientational polarization by **rotation** is much more common in liquids and gases then in solids, because the dipoles can be moved freely.

The total polarization $\boldsymbol{P}$ is represented by the sum of the induced or permanent dipole moments. In order to calculate the corresponding permittivity of the medium, it is important to know how $\boldsymbol{P}$ depends on the external applied electric field $\boldsymbol{E_{ext}}$. In case of induced dipole moments the polarization is proportional to the local electric field at the position of the individual molecule,

$$\vec{P} = N\vec{p} = N\alpha\vec{E}_{local} \tag{1.20}$$

the proportionality constant α is called of the polarizability of the molecule. In the most general case, α is a tensor, for nonlinear dielectric media $\boldsymbol{P}$ contains higher order terms of the electric field (Eq. 1.8b, p. 2, in [5]).

The local electric field $\boldsymbol{E_{loc}}$ is the sum of the external field plus the so-called Lorentz field, which results from the polarization of the molecules surrounding the particular molecule for which the polarization is calculated.

$$\vec{E}_{local} = \vec{E}_{ext} + \frac{\vec{P}}{3\varepsilon_0} \tag{1.21}$$

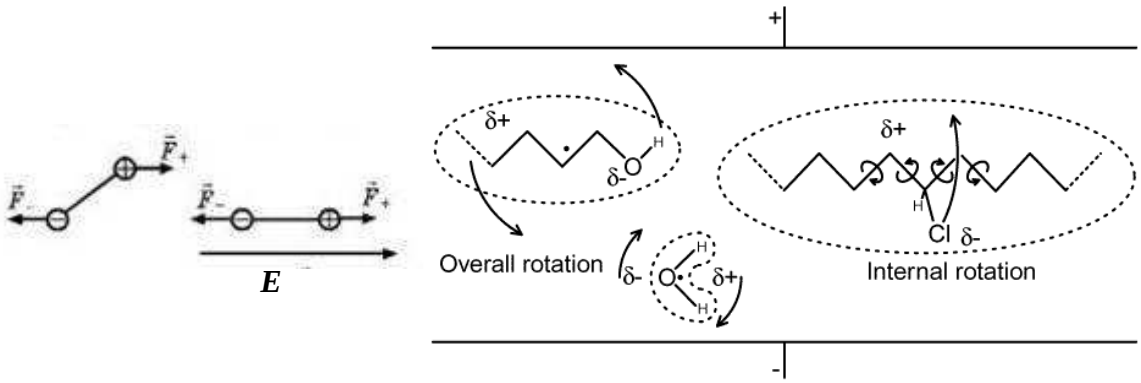

Figure 1.2 Polarization by rotation.

The factor 1/3 in Eq. (1.21) accounts for the spherical shape of an imaginary shell around the particular molecule, which is charged by the polarization imposed by the surrounding molecules [11].

Combining Eqs. (1.20) with (1.21) and expressing $\boldsymbol{P}$ by the permittivity ε_s (static permittivity) according to Eq. (1.3) yield the Clausius-Mossotti relation,

$$\frac{\varepsilon_s - 1}{\varepsilon_s + 2} = \frac{N\alpha}{3\varepsilon_0} \tag{1.22}$$

first derived by Mossotti in 1850, then by Lorenz in 1869, and refined by Clausius in 1879.

Orientational polarization

The polarization we have discussed up to now is the stretching type induced atomic or electronic polarization. However, if the molecules possess a permanent ground state dipole moment, these molecules will tend to reorient in the applied field. The alignment of the dipoles will be disrupted by thermal motion that tends to randomize the orientation of the dipoles. The orientational polarization will then be an ensemble average of dipole moments aligned in the field according to Eq. (1.17). If the permanent dipole moment is $\boldsymbol{p}$, then the interaction energy with the field is $W = \boldsymbol{pE} = |\boldsymbol{p}|\,|\boldsymbol{E}|\cos\theta$, where θ is the angle between the dipole and the field direction. Thus, the polarization is given by

$$\vec{P} = N\langle \vec{p} \rangle = N\vec{p}\langle \cos\theta \rangle \tag{1.23}$$

The indicated average is an average over a Boltzmann distribution, where the ratio of dipole interaction energy $pE\cos\theta$ and thermal energy kT (k=1.38·10^{-23} J/K =Boltzmann constant) determine the effective dipole moment at a temperature T.

$$\langle \cos\theta \rangle = \frac{\int_0^{\pi} \cos\theta \exp\left[\frac{pE\cos\theta}{kT}\right] \sin\theta d\theta}{\int_0^{\pi} \exp\left[-\frac{pE\cos\theta}{kT}\right] \sin\theta d\theta} \tag{1.24}$$

The solution

$$\langle \cos\theta \rangle = \coth(u) - \frac{1}{u}; \qquad u = \frac{pE}{kT} \tag{1.25}$$

is known as the Langevin function. It approaches $u/3$ for $u << 1$ and 1 when u is large. For liquids at room temperature, the limit $u << 1$ can be applied. As an example, the dipole moment for the water molecule is $6.3 \cdot 10^{-30}$ C·m = 1.86 D (1D= 1 Debye = $4 \cdot 10^{-18}$ esu·cm = $3.355 \cdot 10^{-30}$ C·m) [6], even at a very high electric field 1 kV/cm (in comparison to fields used in the microwave experiments performed and described in successive chapters), $u=pE/kT$ = $4.3 \cdot 10^{-4}$ at T = 300 K. Thus, the total polarization can be expressed as the sum of the induced and orientational polarization as:

$$\vec{P} = N\left(\alpha + \frac{p^2}{3kT}\right)\vec{E}_{loc} \tag{1.26}$$

Combining Eq. (1.26) with the Clausius-Mosotti relation (Eq. (1.22)) yields to the Debye equation for the static permittivity of a liquid:

$$\frac{\varepsilon_s - 1}{\varepsilon_s + 2} = \frac{N}{3\varepsilon_0}\left[\alpha + \frac{p^2}{3kT}\right] \tag{1.27}$$

Eq. (1.27) works reasonably well for many organic liquids such as alcohols, however, it fails for water. The reason for the failure is the Lorentz local field correction, which explicitly leads to the values of the local field in Eq. (1.21) and consequently results in the Clausius Mossotti relation (Eq. (1.22)) and Debye equation (Eq. (1.27)), starts from a cavity surrounding a molecule which is large compared to the molecular dimension. Therefore, the local interaction between adjacent dipoles is not considered. In case of organic molecules with localized polar groups such as alcohol, the influence of the dipole-dipole interaction is rather weak, because the OH-groups of adjacent molecules are separated from each other due to the large size of the molecule.

As an extension of the Lorentz model, two more advanced models have been developed to solve the local field problem, the Onsager model and the Kirkwood model. Both models attempt to account for the local interactions of the molecules in an applied electric field. They are continuum approaches, i.e. like in the Lorentz model, a molecule is assumed to be inside a cavity, and outside that cavity the medium is treated as a continuum dielectric with dielectric constant ε_r. The models mainly differ by the definition of the cavity. In the Lorentz model a cavity being much larger than the molecule size is assumed. The Onsager model focuses on the creation of a cavity around a single molecule of interest which radius a being of the order of the molecule size, or explicitly $a = (3/4\pi N)^{1/3}$, with N being the number of molecules per volume. In the Lorentz theory it is assumed that the dipole moment $\boldsymbol{p}$ is not affected by the solvation shell. For water, which has a gas phase dipole moment of 1.86 D, the dipole moment in the liquid phase is 2.3–2.4 D. Obviously, the neighboring water molecules have a large effect inducing a dipole moment in the liquid of more than 25% larger than the gas

phase dipole moment. In contrast, within the Onsager model it is assumed that the local field $\boldsymbol{E_{local}}$ is composed of a cavity field $\boldsymbol{E_c}$ and a reaction field $\boldsymbol{E_r}$

$$\vec{E}_{local} = \vec{E}_c + \vec{E}_r \tag{1.28}$$

The cavity field is produced by the external field in the spherical cavity:

$$\vec{E}_c = \frac{3\varepsilon_s}{2\varepsilon_s + 1}\vec{E}_{ext} \tag{1.29}$$

Notice that the cavity field is always larger than the external field, in analogy to the Lorentz local field. However, whereas the Lorentz local field increases proportional to ε_s, the Onsager cavity field increases only from 1 to 1.5 as ε_s approaches infinity.

The reaction field is proportional to the dipole moment of the molecule in the cavity

$$\vec{E}_r = \frac{\varepsilon_s - 1}{2\varepsilon_s + 1}\frac{\vec{p}}{a^3\varepsilon_0} = g\vec{p} \tag{1.30}$$

The reaction field is always parallel to the permanent dipole moment, therefore only the cavity field can exert a torque on the dipole and cause it to align in the applied field. By separating these two effects, the Onsager model results in the following expression for the static permittivity ε_s:

$$\frac{(\varepsilon_s - \varepsilon_\infty)(2\varepsilon_s + \varepsilon_\infty)}{\varepsilon_s(\varepsilon_\infty + 2)^2} = \frac{N}{9kT\varepsilon_0}p^2 \tag{1.31}$$

In Eq. (1.31), ε_∞ is the infinite frequency dielectric constant (usually taken from refractive index measurements in the optical range).

In contrast to the Lorentz model, Eq. (1.31) provides a better description of the dielectric constant of dense fluids [6], but it does not take into account local forces.

According to the Kirkwood model, the static permittivity is expressed by the Kirkwood-Fröhlich equation derived in chapter 1, 3 of [6]

$$\frac{(\varepsilon_s - \varepsilon_\infty)(2\varepsilon_s + \varepsilon_\infty)}{\varepsilon_s(\varepsilon_\infty + 2)^2} = \frac{N}{9kT\varepsilon_0}gp_0^2 \tag{1.32}$$

with p_0 being the dipole moment of an isolated water molecule. The Kirkwood-Fröhlich equation only differs from Eq. (1.31) by the g-factor or correlation parameter g. This parameter represents the ratio between the dipole moment p^* of a sphere when the central molecule is held in fixed alignment and p_0 . The temperature dependent correlation function $g(T)$ was calculated for various structural models of water taking into account details of the hydrogen bonds, giving reasonable agreement with experimental results Chapter.3.3 in [6].

Within the Kirkwood model, non-linear effects can also be described. The use of the Langevin function L($\boldsymbol{pE}/kT$) in higher order of approximation yields the expression

$$\varepsilon_s(E) = \varepsilon_\infty + \frac{7N\pi(\varepsilon_\infty + 1)p_0^{\,2}}{54\varepsilon_0 kT}\left[1 - \frac{49E^2 p_0^{\,2}(\varepsilon_\infty + 2)^2}{540k^2T^2}\right] \tag{1.33}$$

which is valid for relatively low fields, which means $E \leq 5\cdot10^6$ V/m, at which ε_s has dropped from 80 at E=0 to about 50. However, at microwave frequencies such a field would already cause dramatic heating, since the power P = ½ $Z_L^{-1}E^2$ corresponding to such a high field would be $2.5\cdot10^{11}$! Watts for a field generated in a transmission line with a line impedance of Z_L=50 Ω. Even in high Q resonator experiments, where the required power is reduced by the Q factor, the change of ε_s by the temperature change induced by strong heating at microwave frequencies (see next section) would strongly exceed the direct field dependence predicted by Eq. (1.33).

1.4 Theoretical models for the frequency dependence of the complex dielectric function of liquids

The discussion above about the polarization of non-conducting systems indicates the existence of two contributions to the polarization $\boldsymbol{P}$ with quite different origins, namely the strongly temperature- and frequency-dependent orientational polarization $\boldsymbol{P}_{or}$ stemming from the alignment of the molecular dipole moments against thermal motion, and the intramolecular induced polarization $\boldsymbol{P}_{ind}$, which is nearly temperature- and frequency-independent up to optical frequencies.

$$\vec{P} = \vec{P}_{or} + \vec{P}_{ind} \tag{1.34}$$

These facts are used experimentally for the separate determination of $\boldsymbol{P}_{\mathrm{or}}$ and $\boldsymbol{P}_{\mathrm{ind}}$:

$$\vec{P}_{or} = \varepsilon_0(\varepsilon_S - \varepsilon_\infty)\vec{E} \qquad \vec{P}_{ind} = \varepsilon_0(\varepsilon_\infty - 1)\vec{E} \tag{1.35}$$

The static permittivity ε_s includes the orientational polarization, the optical permittivity ε_∞ and denotes the optical polarization, which includes atomic and electronic contribution of the induced polarization. Fig 1.3 shows the typical structure of the dispersion $\varepsilon'(f)$ and the absorption $\varepsilon''(f)$ curves of a simple non-conducting liquid with a single energy absorbing relaxation process in the microwave (MW) region at about 10 GHz and two resonant transitions in the IR and UV regions corresponding to atomic and electronic induced polarization.

The first plateau from 0 to about 0.1 GHz is the range of **static** permittivity, where $\varepsilon_s=\varepsilon'(f)=\varepsilon'(0)=\varepsilon^*$ and $\varepsilon''(f)$ = 0. The steep negative slope of $\varepsilon'(f)$ is situated in the frequency region where dipole orientation increasingly lags behind the applied field. This relaxation process, where $\varepsilon'(f)$ decreases from ε_s to ε_∞, reduces the orientational polarization from its equilibrium value to zero. The energy dissipated during the relaxation process is represented by the absorption curve $\varepsilon''(f)$. There is a maximum in the $\varepsilon''(f)$ curve at the frequency at which ε' versus log f exhibits an inflection. The quantity $\Delta\varepsilon = \varepsilon_s - \varepsilon_\infty$ is called the *dispersion amplitude* of the relaxation process.

When the direction of the field is changing sufficiently fast, the molecular forces impeding the dipole orientation dominate, and the dipoles become unable to follow the changes; at these frequencies the orientation of permanent dipoles no longer contributes to the dielectric constant. The relaxation region is followed by a plateau at ε_∞ where, again, no significant energy dissipation takes place, i.e $\varepsilon''(f)= 0$. The induced polarization does not change during the relaxation process and on the plateau at ε_∞ where the total polarization $\boldsymbol{P}(f)$ equals $\boldsymbol{P}_{\text{ind}}$. The resonant transitions due to atomic $\boldsymbol{P}_{\text{at}}$ and electronic $\boldsymbol{P}_{\text{el}}$ displacements further reduce $\varepsilon(f)$ stepwise from ε_∞ to unity

Fig. 1.3 shows a plateau in the UV region at n^2_D (n_D: refractive index of the sample at the wavelength of the Na_D line) which is often used in the classical theories instead of the correct value of ε_∞ for the calculation of $\boldsymbol{P}_{\text{ind}}$ (estimated precision 10 to 15%).

The simple model liquid depicted by Fig. 1.3 reflects the major features of the high permittivity spectra. As far as real electrolyte solutions are concerned it is still incomplete, because it considers only a single relaxation process in the solution and, especially does not consider the dielectric loss in electrolyte solutions caused by electric conductivity.

1.4.1 Debye relaxation

As the simplest model for the time evaluation of the orientational polarization $\boldsymbol{P}_{or}$, it is assumed that increase of orientational polarization $\boldsymbol{P}_{or}$ is proportional to the polarization itself.

$$\frac{d\vec{P}_{or}}{dt} = \frac{\vec{P}_{or}}{\tau} \tag{1.36}$$

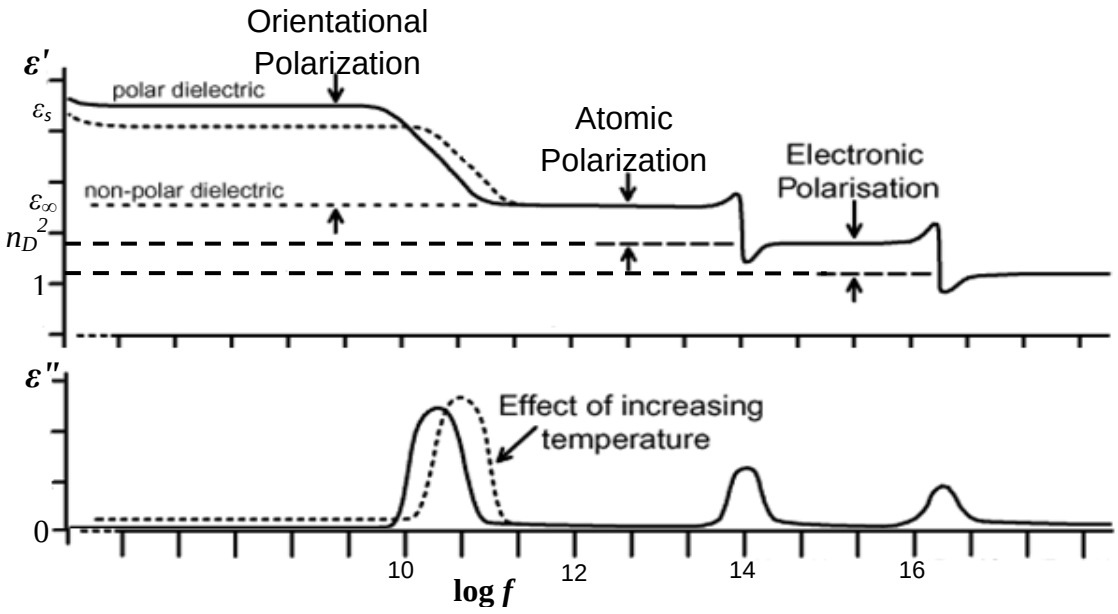

Figure 1.3 Dielectric dispersion $\varepsilon'(f)$ and absorption $\varepsilon''(f)$ spectra for a polar liquid with a single Debye relaxation process in the MW region and two resonant transitions in the IR and UV range.

The relaxation time τ describes the time required for a reoriented dipole aligned in an electric field to return to the vicinity of its normal position after removal of the electric field (or the time required for dipoles to become oriented in an electric field). For the case that a field is switched on at t=0, the solution of Eq. (1.36) is

$$\vec{P}(t) = \vec{P}_{in} + \vec{P}_{or}(1 - \exp(-t/\tau)) \tag{1.37}$$

indicating that the polarization evolves with time from the induced polarization at t=0 towards the sum of induced and orientational polarization within the relaxation time τ.

Within linear response theory, the time evolution of the polarization is related to the time dependent dielectric function by:

$$\vec{P}(t) = \vec{P}_{in} + \varepsilon_0 \int_{-\infty}^{t} \varepsilon(t-t') \frac{d\vec{E}(t')}{dt'} dt' . \tag{1.38}$$

Inserting $\boldsymbol{E}(t)=\boldsymbol{E}_0\exp(-i\omega t)$ and comparing of the time derivative of Eq. (1.37) with that of Eq. (1.38) leads to (employing $\boldsymbol{P}=(\varepsilon^*(\omega)-\varepsilon_\infty-1)\boldsymbol{E}$)

$$(\varepsilon^*(\omega) - \varepsilon_\infty - 1)\tau^{-1}\vec{E}(t) - i\omega(\varepsilon^*(\omega) - \varepsilon_\infty - 1)\vec{E}(t) = -\varepsilon_0\varepsilon_s i\omega\vec{E}(t) + \varepsilon_0\varepsilon_\infty i\omega\vec{E}(t) \tag{1.39}$$

and hence to the following expression for the complex dielectric function of a liquid:

$$\varepsilon^*(\omega) = \varepsilon_\infty + \frac{\varepsilon_s - \varepsilon_\infty}{1 - i\omega\tau} . \tag{1.40}$$

Separation of the complex dielectric function ($\varepsilon^*(\omega)$) in real and imaginary part results in the following expressions:

$$\varepsilon'(\omega) = \varepsilon_\infty + \frac{\varepsilon_s - \varepsilon_\infty}{1 + \omega^2\tau^2} \qquad \varepsilon''(\omega) = (\varepsilon_s - \varepsilon_\infty)\frac{\omega\tau}{1 + \omega^2\tau^2} \tag{1.41}$$

Eqs. (1.40) and (1.41) are known as the Debye or the Debye-Drude equations, following their derivations in Debye's classic book "Polar Molecules" [12], the corresponding results for $\varepsilon'(\omega)$ and $\varepsilon''(\omega)$ of water are illustrated in Fig. 1.4.

Cole-Cole diagram

The complex permittivity can also be represented graphically in a Cole-Cole diagram (Argand diagram) in the complex ε'', ε' plane (Fig. 1.5). The imaginary part ε'' is plotted on the vertical axis and the real part ε' on the horizontal axis with frequency as an independent parameter. A material comprising a single relaxation according to the Debye relation will appear as a semicircle stretching from $\varepsilon'=\varepsilon_s$, $\varepsilon''=0$ in the low-frequency limit to $\varepsilon'=\varepsilon_\infty$, $\varepsilon''=0$ in the high-frequency limit with the peak of the loss factor occurring at $\omega_c=1/\tau$.

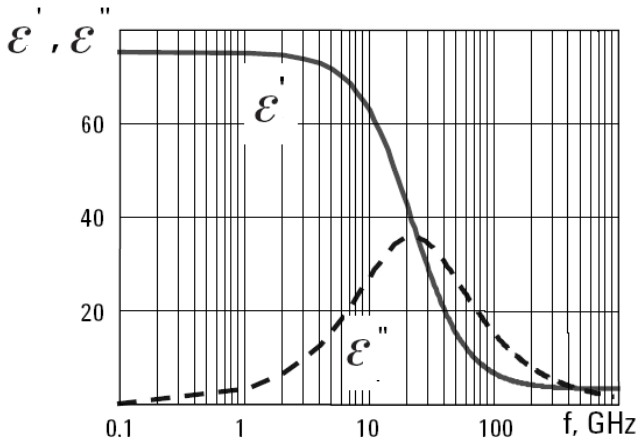

Figure 1.4 Relaxation of water at 30°C according to the Debye equations (Eq. 1.41).

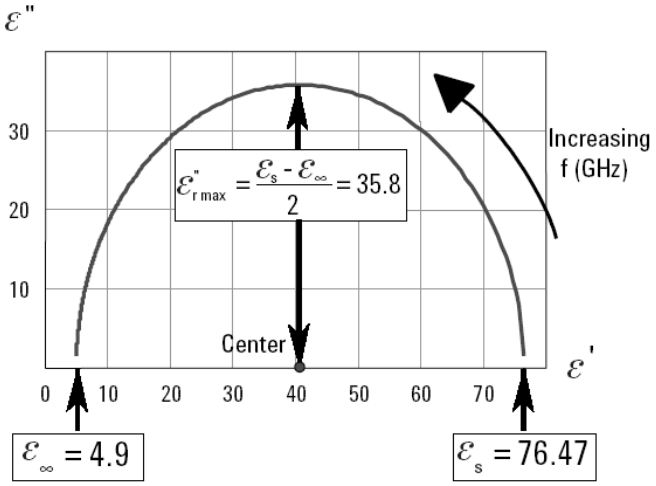

Figure 1.5 Cole-Cole diagram of the data shown in Fig. 1.4.

1.4.2 Non-Debye relaxation models

The Debye model is essentially the only one which starts from clearly defined hypotheses and deduces the dependence of complex permittivity on frequency on the material parameters in a rigorous way. For many liquids this model can be used to approximate experimental data, in particular for water. In addition, it represents more or less reliable approximation for simple non-auto associating solvents. However, the relaxation behavior of a variety of real systems can be reproduced with the help of the Debye model only within limited frequency regions. In order to deal with the more complicated relaxation behavior which is usually observed in case of broader frequency coverage, the analysis of the experimental data is based on a combination of several distinct relaxation processes. In particular, in certain liquids, such as mixtures and solutions, some dipoles relax with one characteristic rate, some with another. In such cases, a discrete sum or even a distribution of relaxation times can be employed to fit the data within Debye theory. Over the years, different models for dielectric relaxation functions were developed which allow to fit experimental data.

Models based on combination of distinct Debye processes

For liquids composed of non-hydrogen-bonded molecules, only one relaxation process is usually observed. Hydrogen-bonded liquids reveal a superposition of several clearly distinct relaxation processes. The slow process characterized by τ_D is cooperative in nature. τ_D is relatively long, since it is associated primarily with a rotation relaxation within a hydrogen bonded cluster, and reduces considerably with temperature as hydrogen bonds are weakened or broken. Early investigations over a limited frequency ranges successfully represented the permittivity of water with a single Debye process of relaxation time $\tau_1=\tau=\tau_D$=8.3 ps at 25°C, experimental data at frequencies above 50 GHz revealed an additional high frequency relaxation process with τ_2=1.0 ps and 2% relative amplitude, which is connected to hydrogen-bond formation and decomposition, as graphically illustrated by

–H:X– → –H + :X–.

The relaxation process originates from the reorientation of mobile water molecules without or with single H-bonds and of asymmetrically two-bonded molecules. Therefore, τ_2 is small in comparison to τ_1 and less temperature dependent, which is primarily determined by the translational vibrations (near 200 sm^{-1}) within the hydrogen bonded cluster. A double step Debye relaxation process (D_1 + D_2)

$$\varepsilon^*(\omega)=\varepsilon_\infty+\frac{\Delta\varepsilon_1}{1+i\omega\tau_1}+\frac{\Delta\varepsilon_2}{1+i\omega\tau_2} \tag{1.42}$$

with $\varepsilon_s=\varepsilon_1=\varepsilon_\infty+\Delta\varepsilon_1+\Delta\varepsilon_2$; $\Delta\varepsilon_1=\varepsilon_2-\varepsilon_s$; $\Delta\varepsilon_2=\varepsilon_\infty-\varepsilon_2$; $\varepsilon_2=\varepsilon_{\infty 1}$ provides the best approximation for the complex permittivity of water and other polar liquids at frequencies up to 1 THz. For mono-alcohols the superimposition of three Debye processes (D_1 + D_2 + D_3) yields an appropriate description of the dielectric behavior (Fig. 1.6). These substances, which are able to associate into winding chains, exhibit a relaxation time τ_1 due to the interaction of these chains, a relaxation time τ_2 attributed to the rotation of monomers and molecules situated at the chain ends, and a relaxation time τ_3 due to the hindered rotation of molecules within the H-bonded system.

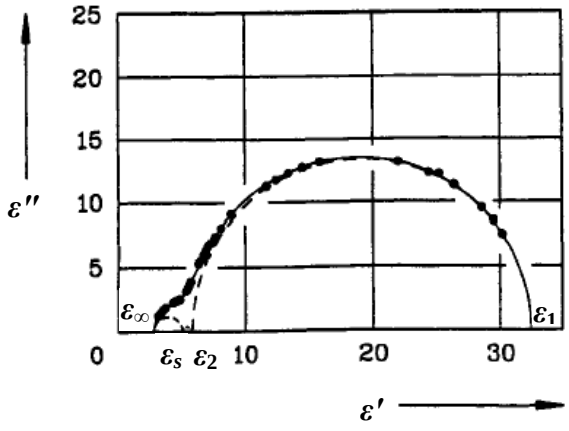

Figure 1.6 Argand diagram calculated from a fit of three superimposed Debye equations and experimental data of methanol at 25°C [13].

Fig. 1.6 shows an example where a three-step Debye equation corresponding to three relaxation processes in the liquid was employed to fit experimental data.

Models with broad relaxation time distributions

In the following, non-discrete distributed relaxation times will be discussed in order to fit experimental data which do not obey to a single Debye equation or a sum of a few distinct Debye terms. To account for such distribution, a Cole-Cole function (CC) can be employed

$$\varepsilon^*(\omega) = \varepsilon_\infty + \frac{\varepsilon_s - \varepsilon_\infty}{1-(i\omega\tau)^{1-\alpha}}, \tag{1.43}$$

which describes a more or less broad symmetric distribution of relaxation times around τ by use of a distribution parameter α, $0 \leq \alpha < 1$. The corresponding Argand diagram shown in Fig. 1.7 is a semicircle with its center lying below the horizontal ε''-axis, on the line drawn from $\varepsilon''=0$ and $\varepsilon'=\varepsilon_\infty$ and making an angle of $\alpha\pi/2$ with the horizontal axis.

The *Cole-Davidson model* is used for representation of an asymmetrical distribution of relaxation times with high frequency distributions only. The Cole-Davidson function

$$\varepsilon^*(\omega) = \varepsilon_\infty + \frac{\varepsilon_s - \varepsilon_\infty}{(1-i\omega\tau)^{\beta}} \tag{1.44}$$

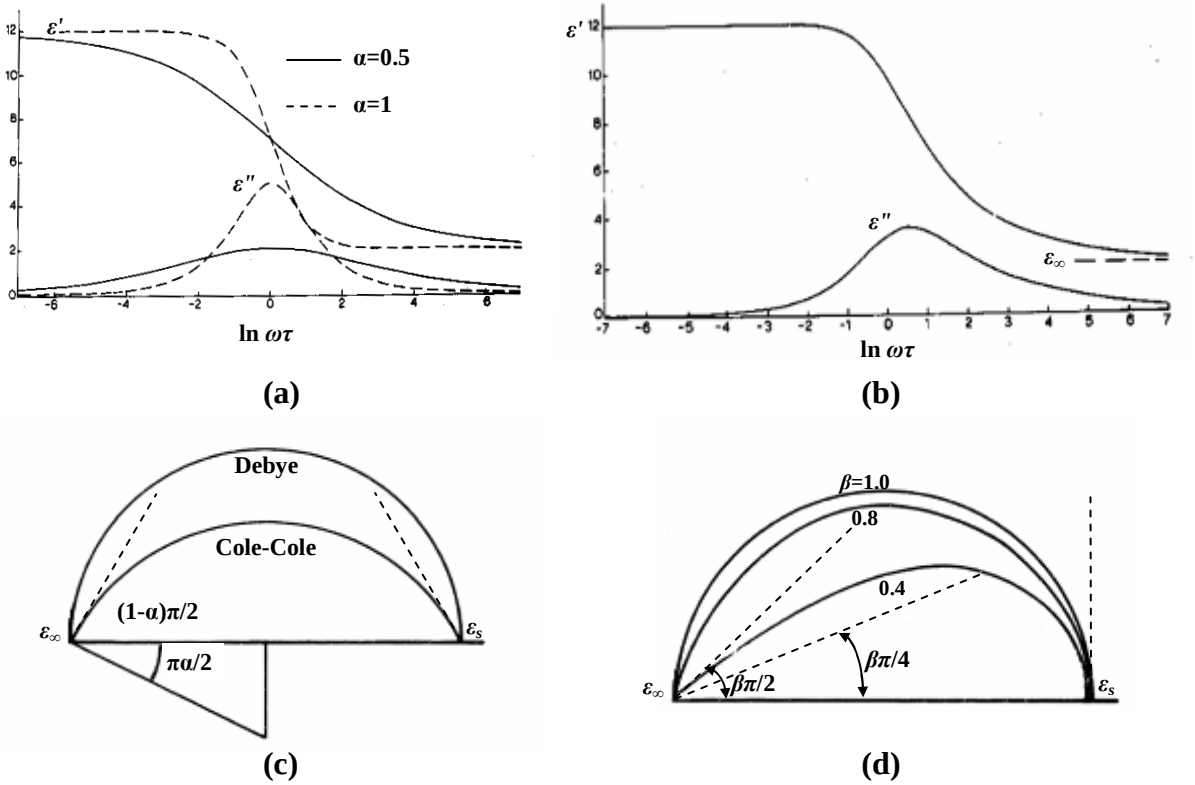

Figure 1.7 (a), (b) $\varepsilon^*(\omega)$ dispersion and loss frequency dependencies; (c), (d) $\varepsilon'(\varepsilon'')$ diagrams for Cole-Cole and Cole-Davidson processes.

includes a distribution parameter β, $0< \beta \leq 1$. The corresponding Argand diagram illustrated in Fig. 1.7 is a skewed arc. The frequency dependence of real and imaginary part of permittivity shown in Fig. 1.7 for the two different approaches illustrate the symmetric (Cole-Cole) and asymmetric (Cole-Davidson) broadening of the relaxation peak.

More generalized empirically equations have been proposed to describe the complex permittivity of polar liquids over a broad frequency range. The model includes Cole-Cole, Cole-Davidson with more or less broad relaxation time distributions around the relaxation time τ_j (characterized by the parameters $\alpha_j>0$ for symmetric and $\beta_j<1$ for asymmetric distributions) as well as single and multiple Debye equations

$$\varepsilon^*(\omega) = \varepsilon_\infty + (\varepsilon_s - \varepsilon_\infty)\sum_{j=1}^{n} \frac{g_j}{\left[1+(i\omega\tau_j)^{1-\alpha_j}\right]^{\beta_j}} \tag{1.45}$$

where n is the number of separable dispersion steps j generated by relaxation times $\tau_{j;}$. The dispersion amplitude

$$g_j = \frac{\varepsilon_j - \varepsilon_{\infty j}}{\varepsilon_s - \varepsilon_\infty} \tag{1.46}$$

represents a weight for each dispersion contribution. Eq. (1.45) contains *Debye process* (D_1) ($\alpha_j=0$, $\beta_j=1$), *Cole-Cole process* (CC) ($0\leq \alpha_j <1$; $\beta_j=1$) and *Cole-Davidson process* ($\alpha_j=0$, $0< \beta_j \leq 1$).

The data listed in Table 1.1 were taken from a survey [13] in which relaxation parameters of commonly used solvents are listed for various solvent classes.

Table 1.1 Dielectric relaxation parameters of selected solvents at 25° C.

Compaund	ε_s	f_{min}-f_{max}, GHz	Equation	τ_1, ps	α_1	β_1	$\varepsilon_2=\varepsilon_{\infty 1}$	τ_2, ps	$\varepsilon_3=\varepsilon_{\infty 2}$	τ_3, ps	$\varepsilon_{\infty 2}=\varepsilon_\infty$	n_D^2
Water	78.36 77.97	0-60 0.9-409	D_1 D_1+D_2	8.27 8.32	0 0	1 1	5.16 6.18	- 1.02	- 4.59	- -	5.16 4.59	1.7765 -
Methanol	32.63 32.47 32.50	0.9-12 0.9-40 0.9-293	CC_1 D_1+D_2 $D_1+D_2+D_3$	50.2 51.0 51.5	0.014 0 0	1 1 1	5.27 5.74 5.91	- 3.3 7.09	- 3.68 4.90	- - 1.12	5.27 3.68 2.79	1.7596 - -
Ethanol	24.35	0.9-89	$D_1+D_2+D_3$	163	0	1	4.49	8.97	3.82	1.81	2.69	1.8473
1-propanol	20.439	0.9-89	$D_1+D_2+D_3$	329	0	1	3.74	15.1	3.20	2.40	2.44	1.9146
2-propanol	19.385	0.9-89	$D_1+D_2+D_3$	359	0	1	3.74	14.5	3.04	1.96	2.42	1.8912
Formamide	109.5	0.9-89	CC_1+D_2	37.3	0.0057	1	7.08	1.16	4.48	-	4.48	2.096
N-methyl-formamide	185.98	0.9-89	D_1+D_2	127	0	1	5.88	3.58	3.79	-	3.79	2.0449
Acetonitrile	35.92 35.96	0.9-40 0.9-89	D_1 CC_1	3.48 3.21	0 0.028	1 1	4.00 2.26	- -	- -	- -	4.00 2.26	1.7800 -
Acetone	20.56l	2.9-24	D_1	3.3	0	1	2	-	-	-	2	1.84
Propylene carbonat	64.96	0.9-89	CD_1	43.1	0	0.9	4.14	-	-	-	4.14	2.0153
Dimetil sulfoxide	46.48	0.9-89	CD_1	20.5	0	0.89	4.16	-	-	-	4.16	2.1831
Pyridine	12.4	0.9-24	D_1	13.3	0	1	2.3	-	-	-	2.3	2.27

Column 1 shows the name; column 2 shows the static solvent permittivity determined by direct measurements at quasistatic frequencies (f < 10MHz) where no energy dissipation

takes place; column 3 shows the range covered by the high frequency equipment, and column 4 indicates the model used for data analysis yielding the results about relaxation parameters in column 5a to 5h. Column 6 shows the quantity n_D^2 from refractometric measurements at optical frequencies.

Influence of ionic conductivity

The introduction of ionic salts into water or other solvents has a significant effect on both its dielectric properties and its structure. Ions which do not possess additional dipole moments from polar groups do not produce proper relaxation process in electrolyte solutions. Nevertheless, they can be recognized by the influence of their volumes and charges on the relaxation process of the solvent.

The concurrent solvent-solvent and ion-solvent interactions in electrolyte solutions generally lead to pronounced changes of the structure compared with the pure solvent. In the relaxation spectra these structural changes result in characteristic changes of the solvent relaxation parameters. Ion pairs and higher ionic aggregates, which possess dipole moments, produce additional relaxation processes.

According to Eq. (1.10) the conductivity σ induced by the dissolved ions add as an additional contribution to the losses expressed by the imaginary part of the generalized permittivity (within the Debye model)

$$\eta''(\omega) = \varepsilon''(\omega) + \frac{\sigma}{\omega\varepsilon_0} = \frac{(\varepsilon_s - \varepsilon_\infty)\omega\tau}{1+\omega^2\tau^2} + \frac{\sigma}{\omega\varepsilon_0}. \tag{1.47}$$

At low frequencies, the losses generated by the influence of electrolytic conduction caused by free ions in the solvent (in biochemical liquids it is usually water) exhibit characteristic $1/f$ frequency dependence. A typical response for combined conduction and relaxation behavior is shown in Fig. 1.8 (a) exibiting the $1/f$ dependence at low frequencies and the Debye relaxation behavior of water at higher frequencies. Fig. 1.8 (b) shows the Argand diagrams taken from [10] for an aqueous solution of a completely dissociated electrolyte compared with that of pure water. The high frequency process (τ_2=1 ps) of water with its very small dispersion amplitude is suppressed for the sake of clarity. Curve 1 is the Argand diagram of the low frequency water process, curve 2 is the representation of the generalized permittivity of the KCl solution (Eq. (1.47)), curve 3 is the Argand diagram corrected for ohmic loss with the help of the conductivity data for the solutions being investigated, obtained independently using a bridge method at quasi static frequencies (200-10000 Hz). The broken line in Fig. 1.8 (b) shows the asymptote of η" for $\omega\rightarrow 0$. A significant feature is the decrease of static permittivity $\varepsilon_s(c)$ of the sample with increase electrolyte concentration. The concentration-dependent decrease of static solvent permittivity is known as the dielectric depression $\Delta\varepsilon$. The physical origin of this depression is that each ion polarizes the surrounding water molecules, which hampers the effect of orientational polarization by the microwave field (see Eq. (1.33)).

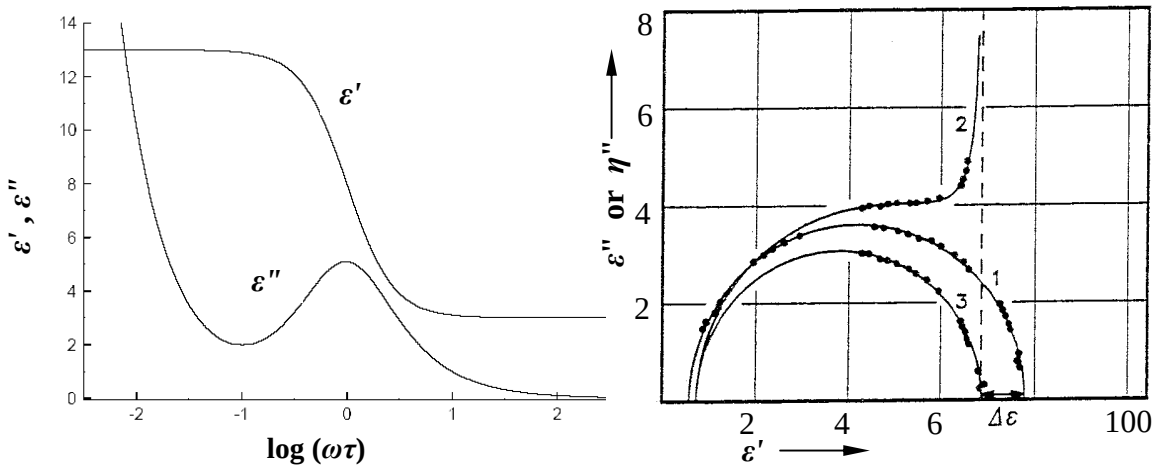

(a) (b)

Figure 1.8 (a) Schematic plots of ε' and ε'' -vs- log$\omega\tau$ for a sample exhibition relaxation and conduction behavior. (b) Argand diagrams of the main relaxation process of a completely dissociated electrolyte, KCl-water solution of c=0.7931 mol dm^{-3} (curve 2: η'' -vs- ε') compared with diagram for pure water (curve 1: ε'' vs ε') at 25°C. Curve 3 for KCl solution was obtained after conductivity correction, $\Delta\varepsilon$: permittivity depression.

1.5 Influence of temperature and viscosity of the medium

There are two factors which mitigate against the alignment of polar molecules in an electric field. One factor being responsible for this incomplete polarization is that the orientating effect of the field is in competition with the randomizing effect of thermal motion. The temperature variation of the inverse microscopic relaxation time will then be approximately exponential, according to the equation

$$\tau = \frac{h}{kT}\exp\left(-\frac{\Delta S^*}{R}\right)\exp\left(\frac{\Delta H^*}{RT}\right) \tag{1.48}$$

where ΔS^* is the molar entropy and ΔH^* the molar enthalpy of thermal activation for the relaxation process. Provided that ΔS^* and ΔH^* are temperature independent, a graph of $\ln(\tau\cdot T)^{-1}$ or $\ln(f_c/T)$, against T^{-1} should be a straight line with negative slope, from which ΔH^* can be calculated, which can give some clues about the molecular energy involved in the relaxation process.

Another factor which affects the molecule orientation is the viscosity of the medium. In effect, a molecule may need to push other molecules out of the way in order to change its orientation. Constant collisions cause internal friction such that molecules turn more slowly and approach exponentially to the final state of orientation within the relaxation time constant τ. When the field is switched off, the sequence is reversed and random distribution is restored with the same time constant τ. This fact means that the relaxation behavior depends on the internal structure of the liquid.

From Debye theory for liquids consisting of spherical molecules of radius a with viscosity η, the relaxation time is determined:

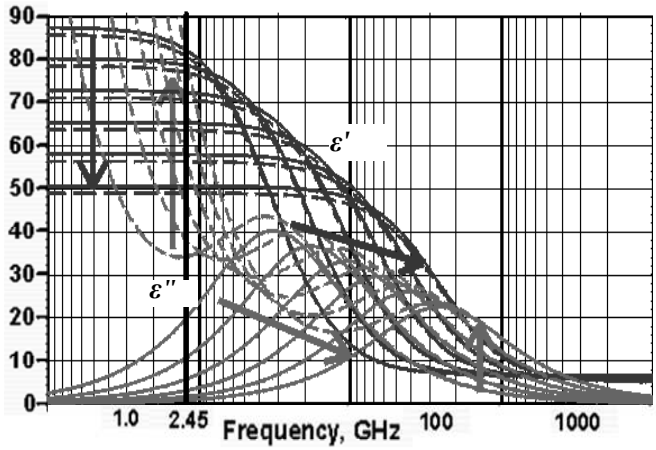

Figure 1.9 Real and imaginary part of dielectric permittivity between 0°C and 100°C obtained for pure water (solid lines) and dilute salt-water solution (dashed lines). The arrows show the effect of increasing temperature or increasing water activity.

$$\tau = \frac{4\pi\eta a^3}{kT} \tag{1.49}$$

Since the viscosity exhibits a thermal activated temperature behavior, Eq. (1.49) results in the same temperature dependence for τ than Eq. (1.48). At low temperatures, the relaxation time of dipole molecules is high because of high viscosity of polar dielectric and low thermal mobility of molecules. With increasing temperature, the relaxation time decreases because the viscosity decreases, and the molecular orientation relieves. This leads to an increase of intensity of dipole-relaxation polarization, which, after passing through a maximum, decreases again with reciprocal temperature due to the thermal motion of molecules.

In particular, for large molecules like proteins, which are large in comparison to the dimensions of the water molecule, the description by a microscopic quantity like the viscosity is justified. However, it even gives the right order of magnitude for the relaxation time of pure water.

The behavior of the complex dielectric function of pure and salty (saline) water is shown in Fig. 1.9 for a variety of temperatures. As the temperature of pure water increases, both the strength and the range of the hydrogen bonds decrease. This lowers both the static dielectric constant and changes the optical permittivity slightly, makes the movement dipole easier and consequently allows the water molecule to oscillate at higher frequencies. In addition, a temperature increase reduces the drag for the rotation of the water molecules, such that the friction and hence the dielectric loss become lower. Note that ε_∞ does not change significantly with temperature.

For pure water, the temperature dependence of the complex permittivity of water can be described by the Debye relation (Eq. (1.41)) with temperature dependence for the static permittivity according to the Kirkwood-Fröhlich equation (Eq. (1.32)) and the thermal activated behavior of the relaxation time according to Eq. (1.48).

In the case of salty water, the ions lead to the depression of static permittivity, as discussed before. At the lower frequencies, the ions are able to respond and move with the changing potential such that frictional heat is produced, which increases the loss factor according to Eq. (1.47). Since the ion conductivity increases with increasing temperature, the losses increase with increasing temperature as it is shown by the dashed lines in Fig. 1.9 (b), in contrast to pure water (solid lines). This explains why salty foods nicely heats in a microwave oven.

1.6 Dielectric data base for water

Water is the basis of life; it is the medium which supports it. The outstanding properties of water have fascinated and likewise intrigued physicist and physical chemists for a long time. During the past decades interest in this unique liquid has grown rapidly with emphasis on microcopic understanding of the intermolecular interactions in pure water and aqueous solutions.

Due to the understandable popularity of water a large data base about experimental permittivity data exists. The microwave dielectric properties of water have been critically evaluated several times during the past decades, more recent reviews are given by [6-8], [14,15]. Therefore, water is an obvious reference for the electromagnetic determination of the biochemical liquids such as being investigated in the framework of this thesis as well as other materials containing “moisture”.

The water molecule is strongly polar, possesses a relatively large dipole moment because the molecule is asymmetric (V-shaped), the lowest-energy electronic configuration provides an angle of 105° between the chemical bonds connecting the oxygen atom to the two hydrogen atoms. This gives rise to a strong orientation effect, and a corresponding ε' of 80 at low frequencies.

Water is also slightly conductive, even in its pure form, due to spontaneous formation of the ions H_3O^+ and OH^- (the H^+ ion cannot exist independently in the solution and attaches itself to a water molecule to become H_3O^+). Water also becomes much more conductive in the presence carbon dioxide, due to the reaction:

$$3H_2O + CO_2 \rightarrow 2H_3O^+ + CO_3^{2-}$$

The conduction processes, being ionic in nature, involve charged particles which are vastly heavier than electrons. Conductivity is therefore limited by the restricted mobility of the charge carriers. According to Eq. (1.41), the absorption declines initially as the frequency is increased, reaching a minimum at about 1MHz with $\tan\delta \approx 0.005$, above 1 MHz it increase steadily as the frequency moves into the dispersion region for orientation polarization (Table 1.2). Water is intrinsically dissociated; so that even de-ionized water cannot be treated as a dielectric at frequencies much below 1 MHz.

One of the best general sources of experimental and theoretical information concerning water, up to 1972 was a treatise of Hasted [6], where he gave a summary of all the known dielectric properties of water.

For all currently available experimental permittivity data authors usually proposed an interpolation function that precisely represents their own data mostly at standard atmospheric pressure and temperatures in the range of $0 \leq T \leq 100$°C. However, surprisingly, there are relatively few general propositions for the permittivity of pure water over wide frequency and temperature ranges. Those that exist fall into one of two categories: frequencies less than 100 GHz [7,8,16] or frequencies above 100 GHz [17,18].

Kaatze [14,16] analyzed a number of data values from the literature and introduced new data in his laboratory. He fitted the data for the frequency range 1-58 GHz and the temperature range 0-60°C to a Debye function.

At frequencies above the abovementioned loss minimum at about 1 MHz, values of ε' and ε'' can be calculated from the Debye equation Eq. (1.41), with accuracy better than being obtainable by interpolation from tabulated values measured at distinct frequencies. Values of the Debye parameters ε_s, ε_∞ and τ were chosen to give the best fit with internally consistent data.

The data in Table 1.2 clearly show the decline in ε' and the corresponding increase in $\tan\delta$ as the frequency is increased.

Table 1.2 Dielectric data for distilled water at 20°C [19].

Frequency / Hz	ε'	$\tan\delta$	$\varepsilon^* = \varepsilon' + i\varepsilon'\tan\delta$
1M	80	0.005	$80 + i0.4$
1G	80	0.056	$80 + i4.45$
3G	78	0.166	$78 + i12.98$
10G	60.62	0.54	$60.62 + i32.79$
35 G	19.9	1.46	$19.9 + i29.06$

There are hundreds of published data that enable one to estimate the Debye parameters at 25°C and over frequency range 0-30 GHz it is interpolated very closely (to within less than 1 %) by a single Debye function. However, it is not true that the extrapolation of this function to the frequency range 30-100 GHz maintains the 1 % accuracy. At 90 GHz, the differences between the extrapolated values and independently measured permittivity values are approximately 10%.

Ellison et al. [7] analyzed over a thousand permittivity values from 60 different sources in the world literature. For fixed temperatures, they fitted the data to single Debye functions in selected frequency ranges that covered the interval 0-100 GHz. The temperature dependences of the various Debye parameters were interpolated by ad hoc polynomials. The resulting interpolation procedure was rather fastidious, and certainly did not correspond closely to a physical reality. However, it had the merit of representing all the data to within the limits of experimental uncertainty.

There are experimental reasons to suspect that a second relaxation process occurs around 170 GHz in water at 25°C and that the permittivity data should be represented by the sum of Debye functions. The second relaxation was predicted from theoretical model by Haggis et al [20]. It was also inferred from and invoked to interpret a variety of experimental data. Buchner et al. [19] attempted to formulate a theoretical model of the second relaxation process. For an adequate fit to the experimental data, it was necessary to invoke a second relaxation process in the permittivity model. At 20°C the second relaxation frequency is about 120 GHz, at 15°C it is about 97 GHz and at 10°C it is about 56 GHz. This means that for T>20°C and for frequencies less than about 70 GHz the influence of the second relaxation will be small. However, for temperatures less than about 10° C the effects of this second relaxation will probably be noticeable for frequencies larger than 20 GHz.

In his recent work [15] Ellison (2007) used all the currently available experimental permittivity data for pure water to derive an interpolation function that precisely represents $\varepsilon^*(f, T)$ at standard atmospheric pressure, for frequencies and temperatures in the range $0 \leq f \leq$ 25 THz and $0 \leq T \leq 100$°C. The permittivity data were presented in terms of relaxations and resonance processes. They described three relaxation processes in the microwave region and two resonances in the far infrared.

For our study it is practical to choose models which would adequately and with high accuracy describe reference water data in the frequency range up to 40 GHz and temperatures from the freezing point to 35° C in order to calibrate our measurement technique and emplying relative measurements to characterize water based solutions of our interest. The interpolation functions derived in the work of Ellison (2007) are too general and too complicated for our particular case, such that we paid our attention to more simple considerations of two works of Kaatze [8] (single step Debye model) and Buchner et al. [19] (involving two Debye processes). The results obtained from the simulations with the aid of Matchcad 2001 Professional based on both abovementioned models and the tabulated parameters listed in [8,19] are shown in the Fig. 1.10 for different temperatures.

The calculated results shown on Fig. 1.10 indicate a good agreement between both utilized models up to frequencies of 30 GHz in the range of our operating temperatures (15-25°C). At frequencies above 30 GHz the second relaxation process cannot be neglected. Therefore, for the calibration of our measurement systems, the two step relaxation model will be applied, which truly describes the behavior of complex dielectric permittivity for water in the selected frequency range.

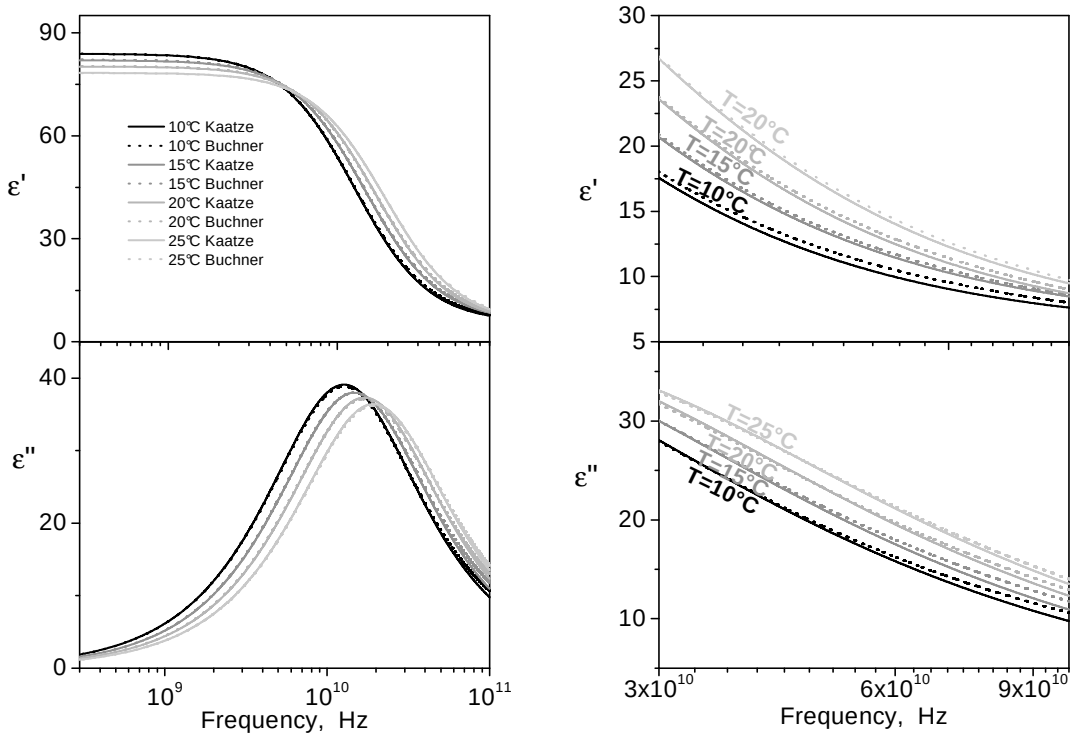

(a) (b)

Figure 1.10 Comparison of calculated dielectric dispersion, $\varepsilon'(f)$, and loss spectrum, $\varepsilon''(f)$, of water on the base of 1 relaxation step [8], solid lines, and 2 relaxation step [19] Debye models, dotted lines, at different temperatures. The results are shown for frequency ranges (a) 0-100 GHz, (b) 30-100 GHz.

Chapter 2: Measurement methods for dielectric properties of different substances including liquids at micro-to-millimeter waves

Today, many different approaches have been developed for the microwave - millimeter wave region which allow to measure the complex dielectric permittivity of liquids and other dielectric substances either at distinct frequencies or over broader frequency range.

The static dielectric constant of a material can be determined by a variety of quasistatic electrical measurements. For liquids, according to the theory of dielectric relaxation mentioned in the previous chapter, it becomes clear that measurements at higher frequencies reveal the decrease of the dielectric permittivity of aqueous solutions with increasing frequency. For water the dielectric relaxation process covers approximately two decades of frequencies. Therefore it was essential to develop methods for experimental determination of the complex permittivity over a wide range of frequencies by using different variants of dielectric spectroscopy, covering nearly 21 orders of magnitude from 10^{-6} to 10^{15} Hz [5]. In order to study systems in such a broad range, a number of different measurement techniques have been developed, each adequate for a special frequency range.

- Low-frequency time domain measurements (10^{-6}–10^{3} Hz);
- Low-frequency frequency domain measurements (10^{-5}–10^{6} Hz);
- Reflective coaxial methods (10^{6}–10^{10} Hz);
- Transmission coaxial method (10^{8}–10^{11} Hz);
- Time and frequency domain quasi-optical methods (10^{9}–10^{12} Hz);
- Fourier-transform methods (10^{11}–10^{15} Hz);

From 10^{-6} to 10^{7} Hz, lumped circuit methods are used, such that a dielectric sample is usually employed as filling material of a capacitor. The sample-capacitor structure is treated as a parallel or serial circuit characterized by its complex electrical impedance $Z^*(\omega)$, expressed in terms of an ohmic resistance $R(\omega)$ and a capacitance $C(\omega)$, which are frequency dependent ($\omega=2\pi f$). The dielectric permittivity $\varepsilon^*(\omega)$, electrical conductivity $\sigma^*(\omega)$ or resistivity $\rho^*(\omega)$ can be derived from the measured $Z^*(\omega)$.

In the range between 10^{7} Hz and 10^{11} Hz so-called “distributed circuit” methods allow to deduce the dielectric function by measuring the complex propagation factor (in reflection or transmission). Waveguide, coaxial, and cavity techniques can be applied. Here the network analysis can be used (frequency domain technique) in which not only reflected wave but also the wave transmitted through a sample are analyzed in terms of phase and amplitude. This allows the frequency range to be extended up to about 100 GHz. However, with increasing frequency and hence decreasing dimensions of coaxial lines or waveguides, the calibration procedure becomes cumbersome.

At frequencies from 10^{-6} Hz to 10^{10} Hz the complex dielectric function $\varepsilon^*(\omega)$ can also be found from measurement of the time dependent dielectric function $\varepsilon(t)$ (time domain measurement system). Both functions are related via a Fourier transformation

$$\varepsilon^*(\omega) - \varepsilon_\infty = \int_{-\infty}^{+\infty} \varepsilon(t) \cdot e^{-i\cdot\omega t} dt \tag{2.1}$$

where $\varepsilon_\infty = \varepsilon'$ ($f \approx 10^{11}$ Hz). The dielectric function $\varepsilon(t)$ can be determined from a measurement of the time dependence of the (d.c.)-polarization current $I(t)$ of a loaded sample capacitor:

$$\varepsilon(t) = \frac{C(t)}{C_0} \text{ and } \frac{d\varepsilon(t)}{dt} = \frac{I(t)}{C_0 U_{Pol}} \tag{2.2}$$

Here U_{Pol} is the polarizing voltage and C_0 is the capacitance of the empty capacitor.

In this case, the experimental approach is simple and less time consuming than measurements in the frequency domain. However, this is possible only on the expense of a reduced accuracy.

Within this thesis, the focus is on frequencies covering the microwave-to-millimeter wave bands. Therefore, in this chapter examples of measurement techniques based on the utilization of network analyzers or frequency domain systems are shown. Such measuring systems also allow a broadband determination of the complex permittivity by various microwave transmission line techniques both in reflection and transmission geometry [21-25].

2.1 Measurement systems

Generally, dielectric measurement techniques can be classified as reflection, transmission or resonant, with open or closed structures for the sensing of the properties of material samples. Closed-structure methods include waveguide or coaxial-line transmission measurements and short-circuited waveguide or coaxial line reflection measurements. Open-structure techniques include free-space transmission measurements and open ended coaxial-line or open-ended waveguide measurements. Resonant structures can include either closed resonant cavities or open resonant structures operated as two port devices for transmission measurements or one-port devices for reflection measurements. The choice of techniques and sample holder design depend upon the nature of the dielectric materials to be measured.

When microwave energy is directed towards a material, part of the energy is reflected, part is transmitted and part is absorbed by the sample. The portion of energy that falls into these three categories have been defined in terms of the scattering parameters and these can be related to the dielectric properties of the sample.

Reflection and transmission of signals due to the interaction with a material under test.

Consider a flat slab of material (MUT=material under test) in space, with a plane wave or another TEM wave (like in a coaxial cable) incident on its surface (Fig. 2.1). There will be

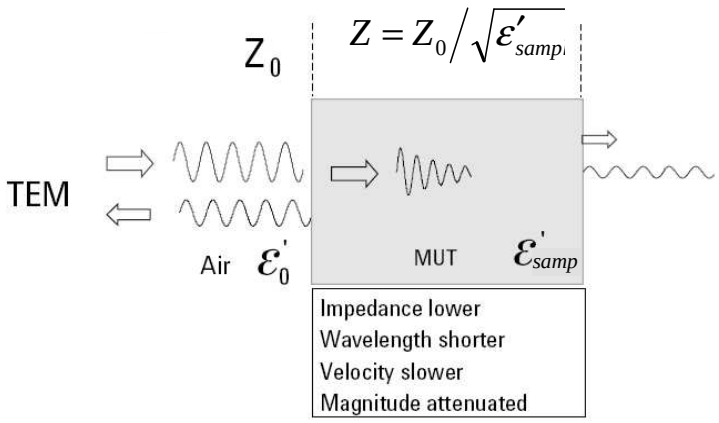

Figure 2.1 Reflected and transmitted signals (from [23]).

incident, reflected and transmitted waves. Since the impedance of the wave in the sample material Z is different (lower) from the free space impedance Z_0, there will be an impedance mismatch by which the reflected wave is created. Part of the energy will penetrate the sample, characterized by ε'_{sample}. Once in the slab, the wave velocity v, is slower than the speed of light c. The wavelength λ_{sample} is shorter than the wavelength λ_0 in free space according to the equations below:

$$Z_0 = \sqrt{\mu_0 / \varepsilon_0}, \quad Z = \frac{Z_0}{\sqrt{\varepsilon'_{sample}}}, \quad \lambda_{sample} = \frac{\lambda_0}{\sqrt{\varepsilon'_{sample}}}, \quad v = \frac{c}{\sqrt{\varepsilon'_{sample}}} \tag{2.3}$$

Since the material will always have some losses, there will be an attenuation or insertion loss (see Eqs. (1.14-1.16)). For simplicity the mismatch on the second border is not considered.

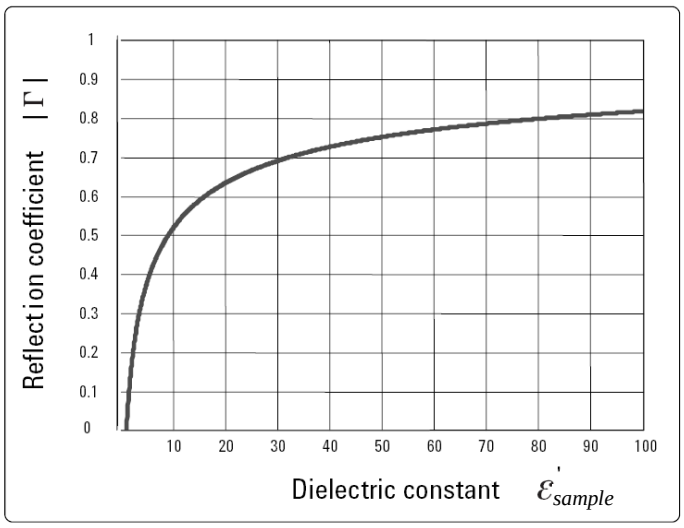

Figure 2.2 Reflection coefficient versus dielectric constant (from [23]).

Fig. 2.2 depicts the relation between the dielectric constant of the sample or MUT and the amplitude of the reflection coefficient $|\Gamma|$ for an infinitely long sample (no reflection from the back of the sample is considered). For small values of the dielectric constant (approximately less than 20), there is a strong change of the reflection coefficient for a small change of the dielectric constant. In this range, dielectric constant measurement using the reflection coefficient will be more sensitive and hence precise. Conversely, for high dielectric constants (for example between 70 and 90) there will be little change of the reflection coefficient and the measurement will have more uncertainty.

S parameter measurements with network analyzer

Vector network analyzers make swept high frequency stimulus-response measurements from 300 kHz to 110 GHz or even 325 GHz. A vector network analyzer consists of a signal source, a receiver and a display (Fig. 2.3). The source launches a signal at a single frequency to the material under test. The receiver is tuned to that frequency to detect the reflected and transmitted signals from the material. The measured response produces the magnitude and phase data at that frequency. The source is then stepped to the next frequency and the measurement is repeated to display the reflection and transmission measurement response as a function of frequency.

A generalized block diagram of a network analyzer in Fig. 2.3 shows the major signal-processing sections. In order to measure the incident, reflected and transmitted signal, four sections are required:

- Microwave signal source for stimulus;

- Signal-separation devices;

- Receivers that down convert and detect the signals;

- Processor/ display for calculating and reviewing the results

A reflection measurement is the ratio of the reflected signal detected at A, over the incident signal detected at R. A transmission measurement is the ratio of the transmitted signal detected at B, over the incident signal detected at R.

The frequency behavior of a microwave device is characterized by its transmission and reflection properties. *S*-parameters (scattering parameters) are a convention for characterizing RF and microwave devices, consisting of reflection and transmission coefficients. Transmission coefficients are commonly referred to as gains or attenuations, reflection coefficients relate to return losses and VSWRs (voltage standing wave ratios).

Conceptually, *S*-parameters describe the linear behavior of a network in terms of voltage wave ratios. Normal convention uses a_n and b_n to represent the amplitudes of the waves given by the voltage of the incoming (incident) and the outgoing (scattered) signal (U^i, U^o) respectively at port n of the device divided by the square root of the wave impedance Z_L of the transmission lines connecting the ports of the network analyzer to the device. Usually, coaxial lines with $Z_L = 50\ \Omega$ are employed.

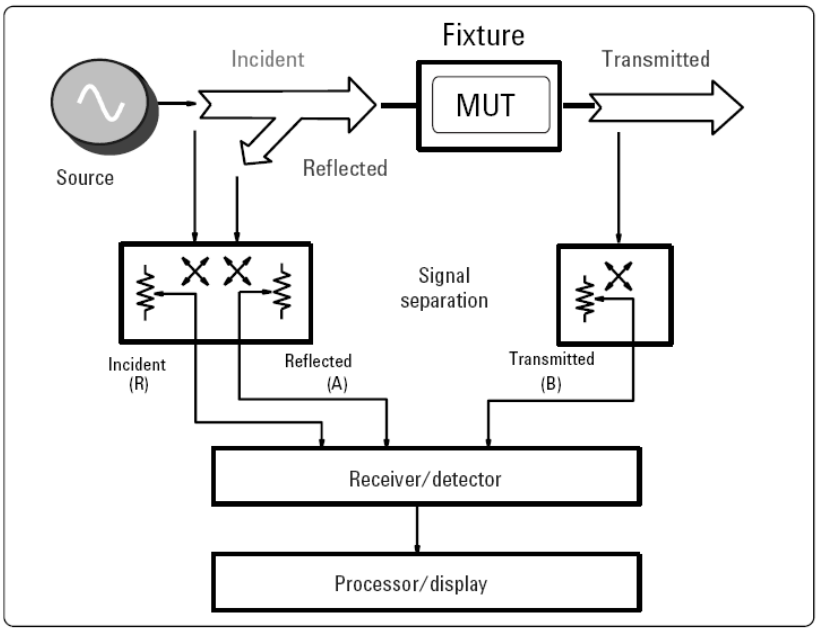

Figure 2.3 Network Analyzer block diagram (from [23]).

$$a_n = \frac{U_n^i}{\sqrt{Z_L}} \qquad b_n = \frac{U_n^o}{\sqrt{Z_L}} \tag{2.4}$$

The diagram in Fig. 2.4 shows the *S*-parameter relationship for a two-port network. Therefore, the transmission properties of the device can be described, when the incoming and outgoing waves are set into relation:

$$\begin{pmatrix} b_1 \\ b_2 \end{pmatrix} = \begin{pmatrix} S_{11} & S_{12} \\ S_{21} & S_{22} \end{pmatrix} \cdot \begin{pmatrix} a_1 \\ a_2 \end{pmatrix} \tag{2.5}$$

For devices with more than two gates, the *S* parameter matrix is replaced by a matrix of the corresponding size. Due to the formulation of the a_n and b_n with a normalization on the wave impedance, the *S* parameters are only determined by the frequency dependence of the device under test, and are independent from the high frequency power of the incoming signal.

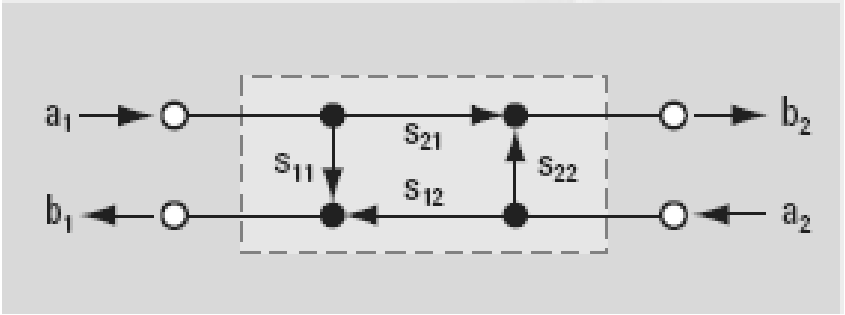

Figure 2.4 Schematic drawing of a two-port device with incoming signals a_1, a_2 and outgoing signals b_1, b_2. The reflection and transmission of the signals through the device are characterized by the *S*-parameters S_{ij}.

The S_{ij} parameters describe the reflection of a signal at port i for $i=j$ and the transmission of a signal from port j to port i for $i \neq j$. The absolute square $\left|S_{ij}\right|^2$ denotes the ratio of the high frequency power for the incoming and outgoing signal:

$$\left|S_{ij}\right|^2 = \frac{P_{in,j}}{P_{out,i}} = \left(\frac{I_{in,j}}{I_{out,i}}\right)^2 = \left(\frac{U_{out,i}}{U_{in,j}}\right)^2 . \tag{2.6}$$

The S parameters are given in dimensionless units of decibel (dB) by $S_{ij}[dB] = 10 \cdot \log(S_{ij})$.

2.2 Comparison of methods

Many factors such as accuracy, convenience, form of materials and sample shape are important with respect to the selecting the most appropriate measurement technique. Some of the significant factors to consider are summarized here:

- Frequency range;
- Expected values of ε_{sample} and μ_{sample};
- Required measurement accuracy;
- Material properties (i.e., homogeneous, isotropic);
- Form of material (i.e., liquid, powder, solid, sheet);
- Sample size restrictions;
- Destructive or nondestructive;
- Contacting or non-contacting;
- Temperature;
- Cost

2.2.1 Coaxial probe

In particular, reflection measurements by open-ended coaxial probes provide a simple and effective technique for broadband characterisation of liquids and semisolid materials at microwave frequencies [25-27].

The open-ended coaxial probe is a cut off section of transmission line which forms a flat plane boundary with the sample. The substance is measured by immersing the probe into a liquid or touching it to the flat face of a solid (or powder) material. This structure creates capacitive fields that “fringe” into the material beyond the conductors (Fig. 2.5(a)). The dielectric properties of the sample will affect the magnitude and phase of the signal reflected

at the boundary. The reflected signal (S_{11}) can be measured and related to sample permittivity ε_{sample} [27].

A vector network analyzer can measure the reflection coefficient of the sample and a computer software algorithm can convert the measured data to dielectric constant versus frequency (Fig. 2.5(b)).

This method is convenient and easy to use; ideal for permittivity measurements of liquid and semisolid materials of relatively high loss, which includes most biological materials, non-destructive for many materials, and requires no sample preparation. It operates over a broad frequency range (200 MHz to 50 GHz) which makes it useful as a trend analysis tool for frequency optimization of a resonant device as being use in the frame of this thesis. Open-ended coaxial probes can be used successfully for permittivity measurements of hard solid materials [27]. But in this case measurement requires a preparation of at least one flat surface and a specially designed "large flange" probe should be applied. In the case of liquids, it is necessary to eliminate air bubbles between the face of the coaxial probe and the sample. There is also uncertainty about the homogeneity of the sample in the vicinity of the probe face.

Before measuring, calibration at the tip of the probe needs to be performed. All parts of the instrument (including the probe) should be mechanically fixed to avoid changes in instrument configuration or cable shape that might affect calibration. Usually, like for a standard S-parameter calibration of coaxial cable ports, calibration is performed by an open end, a short circuit and a matched load (50 Ω resistance for standard calibration). In case of the coaxial liquid probe, short and open ends are similar, but the matched load is replaced by a lossy liquid, usually bidistilled water at a known temperature. Since no liquid with frequency independent properties exists, the well known frequency dependent permittivity of water, which can be translated into frequency dependent load impedance, is employed in the calibration algorithm.

The sample needs to be sufficiently thick to appear "infinite" to the probe, i.e. the evanescent fields at the open end of the coaxial cable should decay almost completely within the sample, which occurs within a distance of the order of a few times the inner diameter of the probe. Typically, this method requires sample thickness of larger than one centimeter, resulting in a minimal required sample volume of a few milliliters in case of a liquid. The coaxial probe measuring technique is not well suited for low loss materials, magnetic materials or when high accuracy is desired. The disadvantages of the method are the limited accuracy compared with other methods (transmission and resonator methods) and the limitation of the thickness of the sample.

Various approaches have been reported recently to reduce the volume of the liquid required for broadband measurement. Murata et al. [28] employed a variable capacitive gap between the inner conductors of two oppositely faced coaxial lines and demonstrated broadband permittivity measurements on thin films of 50 to 300 μm thickness.

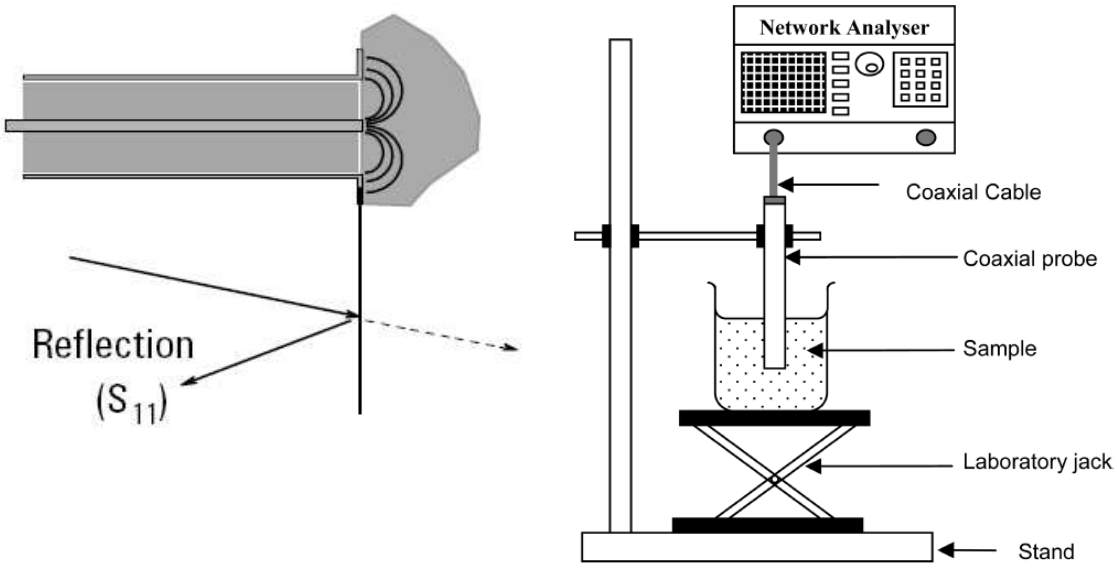

(a) (b)

Figure 2.5 (a) The reflection scheme of the signal; (b) Illustration of the apparatus used for microwave probe liquid measurements (from [23]).

A practical coaxial probe technique for convenient, fast and accurate measurements of thin dielectric materials is presented in a recent paper [29]. The thin dielectric samples, backed by a short circuit, are placed flush with the probe. Here two practical measurement set-ups were specifically developed, for thin solid samples and thin liquid samples.

2.2.2 Transmission line methods

Usually a section of a rectangular waveguide or an air filled coaxial line (Fig. 2.6 (a)) is filled with the MUT being precisely shaped to completely fill its cross-section. Placing of the sample in the transmission line segment causes a change in impedance and propagation characteristics in the loaded section of line. ε_{sample} and μ_{sample} of the sample (even with distinct magnetic properties) are computed by standard impedance transformation [30] from the measurement of the reflected signal (S_{11}) and transmitted signal (S_{21}) of the loaded line by a vector network analyzer (Fig. 2.6 (b)). The transmission line method is best for solid materials that can be precisely machined. Measurements on liquids, powders and gases are also possible but these substances must be properly contained in some specially developed cuvettes. For waveguides, the required sample volume is inversely proportional to the frequency.

Coaxial transmission lines cover a broad frequency range, but a toroidal shaped sample is more difficult to manufacture. Waveguide fixtures extend to the mm-wave frequencies and the samples are more simple to machine, but their frequency coverage is limited to the specified waveguide band. Anisotropic materials can be measured in waveguides.

Although the transmission line method is more accurate than the coaxial probe technique, it is somewhat limited in resolution for low loss materials (depending on sample length). For liquids and any other material, the required length depends on the loss tangent

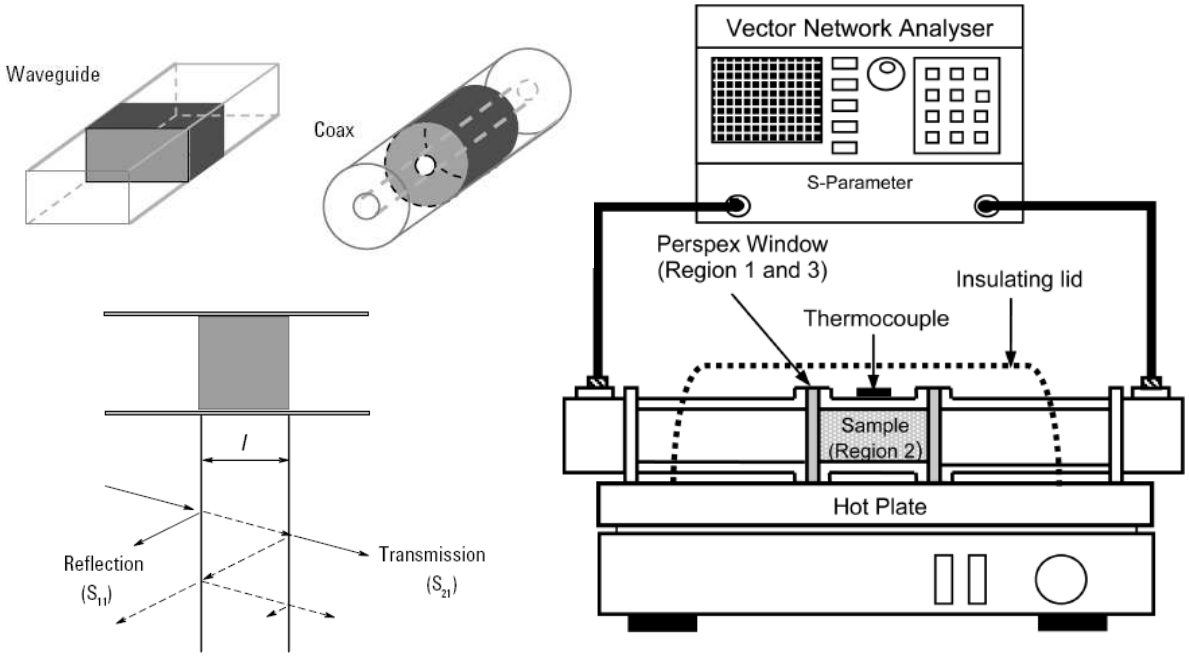

(a) (b)

Figure 2.6 (a) Transmission line method; waveguide and coaxial line case; (b) A practical example of the transmission line (waveguide) setup for microwave measurements under temperature control [23, 31].

which determines the absorption length. At 30 GHz, one cm may give already a very high accuracy for water. Same argument holds for free space measurements.

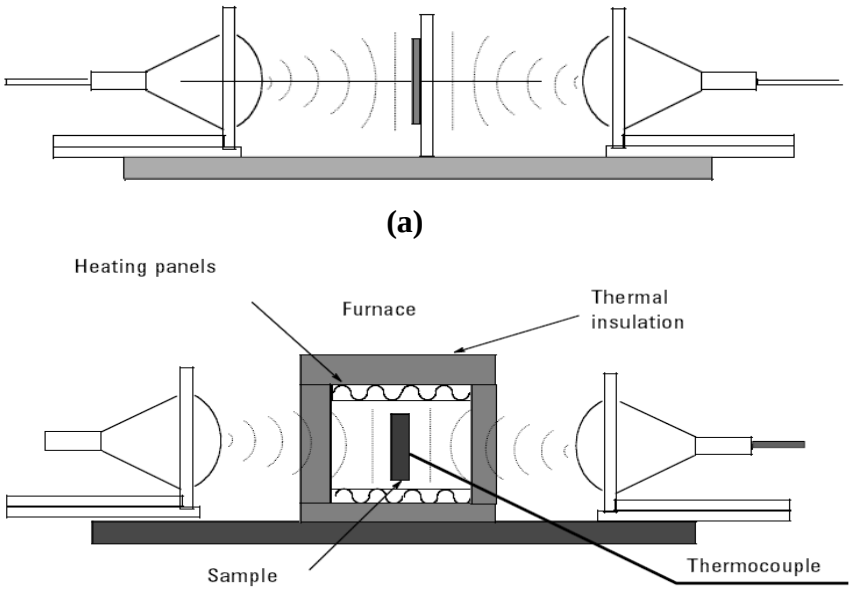

(a)

(b)

Figure 2.7 (a) Free space measurement setup; (b) High temperature measurement in free space [23].

2.2.3 Free space measurements

The free-space methods are also considered as a transmission line technique; instead of a guided wave a quasi-plane wave (for example a sample place in the waist of a Gaussian beam) is employed. A typical free space system consists of a vector analyzer, two antennas facing each other with a sample holder between them. The antennas focus microwave energy at or through a slab of material without the need for a test fixture (Fig. 2.7). This has a potential benefit in comparison with transmission line methods such as a possibility of having material moving in a continuous stream between transmitting horns fitted with focusing lenses. The basic free space materials measurement system is simple and provides the permittivity measurements without contacting the sample, which can be applied to materials to be tested under high temperatures [32] and hostile environments. It is ideal for remote sensing and high temperature applications. The sample can be heated by placing it within a furnace that has “windows” of insulation material that are transparent to microwaves (Fig. 2.7 (b)). Either the transmission thru and/or the reflection off the sample is used to calculate the permittivity.

Uncertainties of the S_{11} measurement using the vector network analyzer are minimized if the sample thickness is close to ¼ λ or ¾ λ where λ is the wavelength in the medium. The required lateral dimensions depend on the spot size of the beam, which increases with increasing wavelength and increasing antenna distance. As a rule of thumb, in case of a Gaussian beam (minimum possible diffraction radius), the illuminated area can be as small as the product of wavelength and antenna distance. The sample should be several times larger in order to avoid uncertainties from diffraction at the sample edges.

The errors in free-space measurement come from multi-reflections between the horn/lens antennas and the surface of the sample.

The free space techniques are inherently broadband and can be used up to the terahertz frequency range. At terahertz frequencies, typically time domain picosecond pulse techniques based on femtosecond lasers and detection by electro optical sampling is employed to measure the dielectric properties of thin sheets (or thin cuvettes in case of liquids) in the range from typically 100 GHz to 2 THz (see for example [4]). Since flat and parallel faces are required, for measurements on liquids the development of flat liquid containers is necessary.

2.2.4 Resonant versus broadband techniques

All the above listed methods are broadband techniques which avoid difficult and time consuming measurements made point-by-point at each frequency in the range of interest.

In comparison to broadband coaxial probe technique and transmission type methods the approaches based on resonator measurements are considered to be the most sensitive ones, because they provide a higher sensitivity due to the multiplicative effect expressed by the quality factor, which is the main characteristic of any resonator. In general, the sample is included as a constituent to the resonator.

Cavity perturbation resonator technique

The resonant method which gains general acceptance is the cavity perturbation technique [33, 34].

Resonant cavities are high Q structures that resonate at certain frequencies. A piece of sample material alters the center frequency (resonant frequency - f_r) and quality factor (Q) of the cavity. A network analyzer is used to measure the resonant frequency and Q of the cavity, both empty and with the sample present. The real part of permittivity can be deduced from measuring the shift of resonant frequency of the loaded cavity; the imaginary part from the change of quality factor (a detailed analysis by perturbation theory will be presented in Chapter 3 in conjunction with the experiments performed in the framework of this thesis). The resonant cavity method has a superior loss resolution, and is therefore suited for low-loss materials.

There are many different types of cavities and methods. The original and most convenient cavity shape is derived from a **rectangular waveguide**. A rectangular waveguide with iris-coupled end plates, operating in TE_{10n}-mode (Fig. 2.8) is employed. The sample is placed in a maximum electric field and for a magnetic measurement, in a maximum of the magnetic field. If the sample is inserted through a hole in the middle of the waveguide length, then an odd number of half wavelengths ($n = 2k + 1$) will bring the maximum electric field to the sample location, such that the dielectric properties of the sample can be measured. An even number of half wavelengths ($n = 2k$) will bring the maximum magnetic field to the sample location and the magnetic properties of the sample can be measured. For dielectric measurements the sample should be shaped and arranged such that the electric field is always parallel to the sample surface (typically a cylinder or slab aligned along a homogeneous electric field) and no field deformation occurs due to the sample (see also Chapter 3).

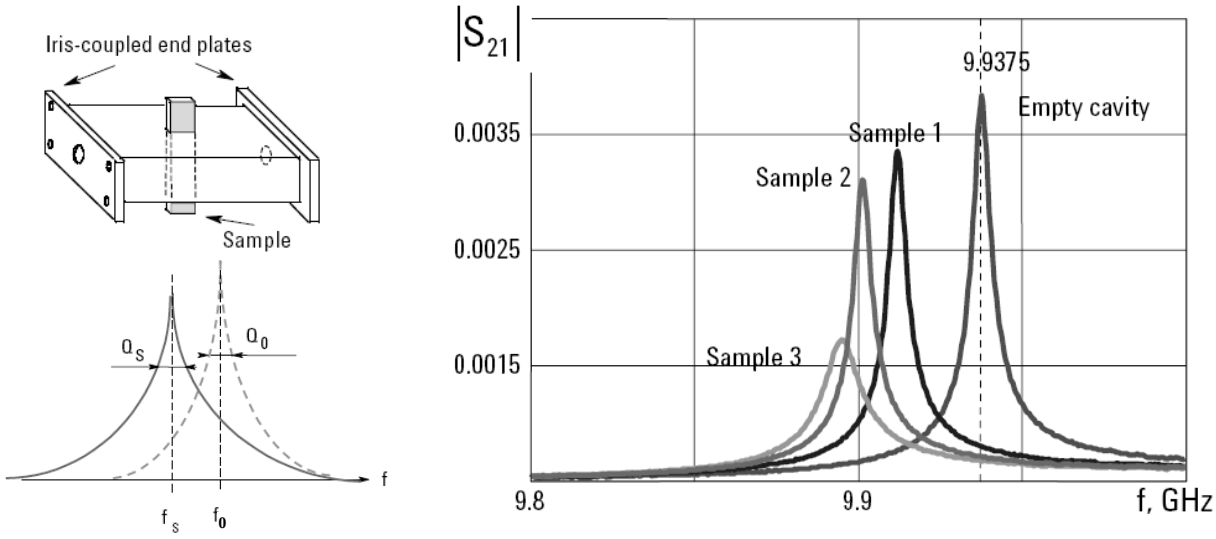

(a) (b)

Figure 2.8 (a) Resonant cavity measurement; (b) Graphs of the empty cavity and three different samples (from [23]).

According to perturbation theory, ε' is determined by the cavity resonant frequency shift and ε'' found from the reduction of cavity Q.

Fig. 2.8(b) shows measurements of three different slab shaped samples employing a rectangular cavity. The three measurements are presented in the same graph for comparison. Due to the sample, the resonant frequency of the empty cavity in the TE_{107} mode shifts to a lower frequency when the sample is inserted in the cavity. When the resonator is loaded with a sample, the resonance curve broadens, which results in a lower quality factor Q. On the y-axis of Fig. 2.8(b) the magnitude of the linear transmission coefficient $|S_{21}|$ is displayed.

In contrast to broadband measurement, the network analyzer does not need any calibration for high-Q resonator measurements.

Although the resonant cavity technique is extremely accurate, it is still subject to errors. The network analyzer must have excellent frequency resolution (1 Hz) to measure very small changes in the Q factor. The sample cross-section dimensions must be known precisely. There is also an additional error due to the approximation in the analysis (perturbation theory). This method has limitations for very low-loss samples due to the comparatively low Q-factor of the empty rectangular waveguide cavity.

A **cylindrical type of cavity** offers higher Q-factors, and therefore requires smaller volumes of the measured liquid. Usually, the liquid specimen is introduced in the following forms:

(i) A rod-shaped solid sample or liquid filled in capillary tube is inserted into an E_{010} (TM_{010}) cylindrical cavity [35-37]. The specimens usually extend over the complete length of the axis of the resonator, as shown in the Fig. 2.9 (a). A single cylindrical cavity has the advantage of higher Q, more simple design and the resonant frequency of the dominant mode is independent of the cavity height. The dominant mode of the resonant cavity is the circularly symmetric TM_{010} mode, which has a maximum axial electric field in the centre of the cavity. The dominant mode TM_{010} (m = 0, n = 1, l = 0), is circularly symmetric since m=0, it has one half field variation across the radius (n = 1) and has no field variation in the axial direction (l = 0).

(ii) A disk-shaped container is inserted into an H_{01n}-mode (TE_{01n}) cylindrical cavity, Fig. 2.9 (b). The diameter of the dielectric specimen is identical to that of the cavity, and is ideally (for minimum uncertainty) an integral number of half-wavelength thick [38,39]. This geometry has proved more fruitful in the 8-40 GHz region when applied for measurements on very-low-loss materials. The requirement for removal of the degenerated TM_{11} mode has led to the construction of these cavities from helical waveguide. The technique can be extended for measurements of liquid dielectrics [40].

Other resonant modes and cavity geometries can be used, as appropriate, for the materials under study, and improvements in experimental techniques for such cavities have been the concern of a number of authors [41-43].

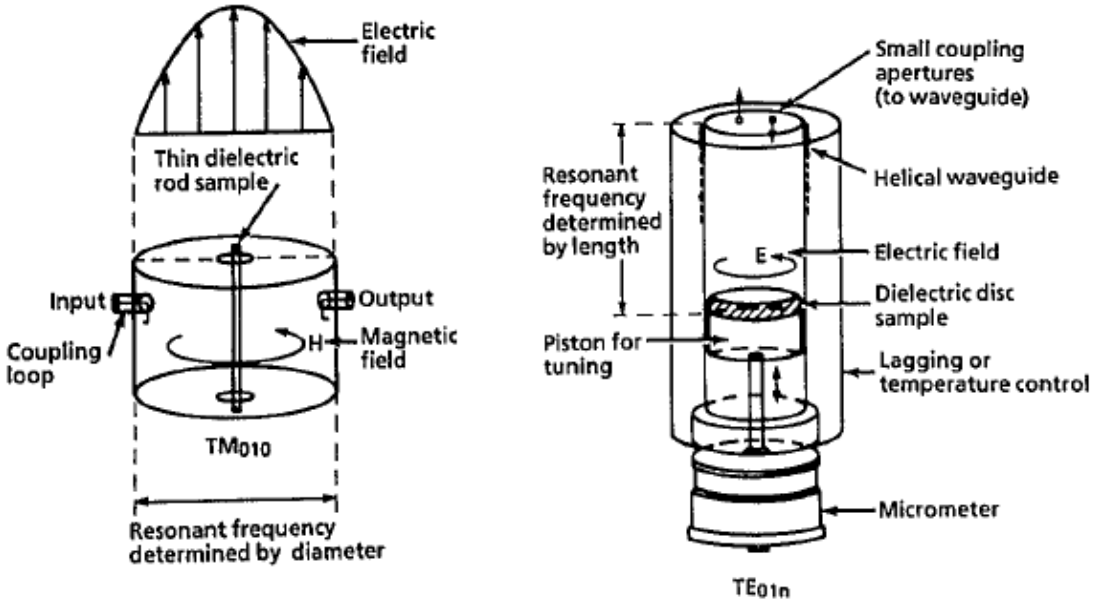

(a) (b)

Figure 2.9 Two cylindrical cavity configurations. (a) The TM_{010} cavity, commonly used for perturbation measurements up to 10 GHz. (b) The TE_{01n} cavity used for low-loss permittivity measurement (8-40 GHz) [22].

Practical difficulties and mathematical approximations can easily increase uncertainties in perturbation measurements to the order of 10 percent for permittivity. The adoption of a more complete description of the cavity fields can be afforded by employing numerical analysis [44].

Resonant methods allow measurements at only one or a few frequencies. This brings a disadvantage. Many workers have been content to work at least at three different microwave frequencies, reasonably widely spaced over the water relaxation band and for aqueous solutions and mixtures the complexities of multiple relaxation can not be adequately unfolded by such microwave studies.

Open resonators

Open resonators, which were developed for millimeter wavelengths, are based on the principle of the Fabry Perot interferometer [45]. This quasi-optical method is most accurate for low loss materials and is superior to the closed cavity resonator in the millimeter bands.

The most sensitive open resonators are of the plane-concave type (a spherical mirror antenna radiates directly onto a plane metal reflector on which is placed a disk dielectric specimen) or bi-concave [46], as shown in the Fig. 2.10. Such structures exhibit TEM resonances in which the electromagnetic fields take the form of a standing-wave Gaussian beam, [47]. The resonant fields have maximum amplitude on the axis and decrease according to a Gaussian function in radial direction. The width of the beam at the waste position (in the center of the resonator for the case of two spherical mirrors with identical radii of curvature, Fig. 2.10b) needs to be smaller than the diameter of the disk in order to avoid diffraction

losses. Similar to the broad band plane wave measurements, the illuminated spot at the waste position has an area of the order of $b \cdot \lambda_0$, where b is the mirror separation and λ_0 is the free space wavelength. The Q-factors which can be achieved are remarkably high – above 150 000 at 35 GHz.

Nowadays, commercially obtainable computer-controlled measurement systems allow many dielectric studies in physics, chemistry and biology to be routinely run. However, even though several types of sensors have been successfully employed in the study of a variety of samples, the construction of specimen cells for particular applications is still a challenging specialist's task. Most methods in use yield the sample properties relative to a reference. The accuracy could be significantly increased by the availability of appropriate sets of reference liquids with their dielectric spectra being precisely known from absolute measurements.

In the framework of this thesis, methods utilizing so-called whispering-gallery mode (WGM) dielectric resonators of different modifications of cylindrical shape comprising local inhomogeneities filled with the liquid under test were developed. The main advantage of WGM resonators: they allow to achieve the highest values of the quality factor and correspondingly, the highest sensitivity to distinguish changes in the resonator parameters due to introduction of even an extremely small amount of liquid into the resonator structure. WGM microcavities have already been successfully applied as miniaturized biosensors in the optical range for the identification and monitoring of proteins, DNA, peptides, and toxin molecules [48-50]. In the microwave-millimetre range the idea of utilizing WGMR-s is still quite fresh and promising. More detailed description of this approach as a new and challenging tool for material characterization is accomplished in the successive chapters.

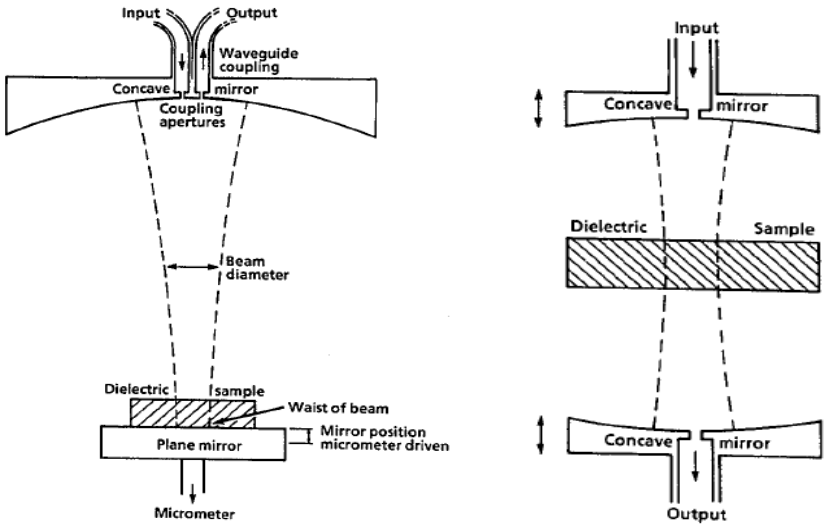

(a) (b)

Figure 2.10 Two geometries of the open-resonator [22]: (a) "hemispherical" and (b) bi-concave.

Chapter 3: Electrodynamic properties of whispering-gallery mode dielectric resonators with liquid inhomogeneities

Whispering galleries have been known in many countries since ancient times. The name itself comes from architectural acoustic, and reflects the fact that sound in closed spaces sometimes propagates not along the shortest path, but rather along concave walls or domes. For instance, in Peking (Beijing), near a famous historical memorial, the Temple of the Sky, there is a miraculous stone wall, which forms an almost closed cylinder. The “miracle” consists in the fact that sound uttered in a low voice in one of the directions along the wall return back after some time to a person who uttered it. This person hears that somebody invisible behind pronounces the same sounds by the person’s voice.

The modern physical explanation of this effect was proposed by Rayleigh on the basis of his own observations made in an ancient gallery located under the dome of St. Paul’s Cathedral in London (Fig. 3.1(a)). Rayleigh found that sound “clutches” to the wall surface and “creeps” along it. The concave surface of the dome does not allow the beam cross section to expand as fast as during propagation in free space. While in the latter case the beam cross section increases and the sound intensity decreases proportionally to the square of distance from a source, the acoustic “ray” in the whispering gallery propagates within a narrow layer adjacent to the wall surface. As a result the sound intensity inside this layer decreases only directly proportionally to the distance, i.e. much slower than in free space.

The relevant physical effect, wave propagation along curved interfaces between two media, is known in other wave processes as well, including light propagation (Fig. 3.1(b)). This gave the name *whispering-gallery waves* for all the cases of wave propagation, which have the same spatial structure as acoustic waves propagating in the so-called “whispering galleries” [51]. In the last decades this type of waves became the object of wide studies due to

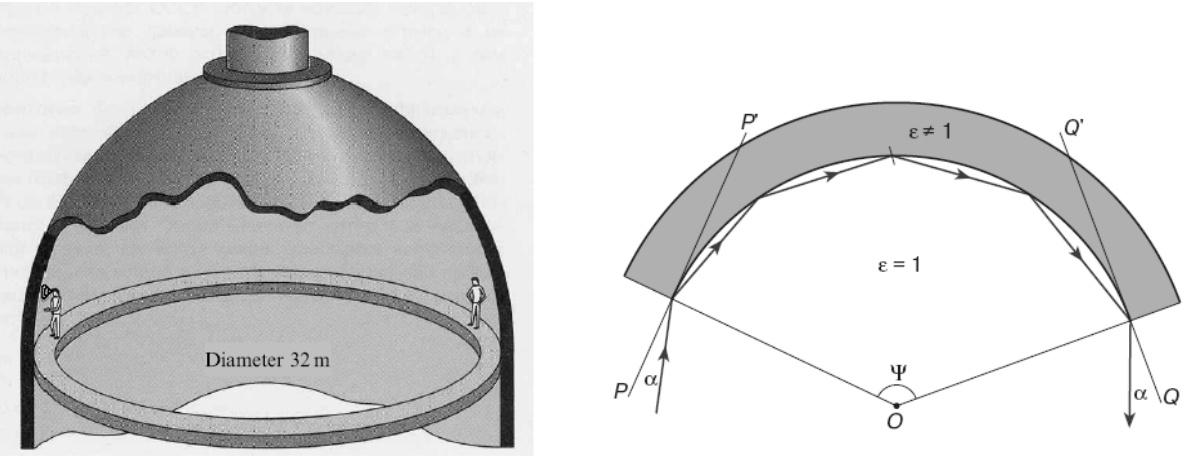

(a) (b)

Figure 3.1 (a) Whispering gallery under the dome of St. Paul’s Cathedral in London. (b) Whispering-gallery mode near the surface of a concave mirror. The arrows show the directions of the entrance and exit of the wave; O is the center of curvature of the mirror; α is the glancing angle; PP' and QQ' are the lines being tangential to the mirror surface [51].

applications in optics as ultrahigh *Q* resonator, for the frequency stabilization of semiconducting lasers, for the microscopic frequency transducers of laser beam. Apart from that, optical whispering-gallery resonators enable highly-sensitive biosensing applications.

One example of whispering-gallery type wave propagation are microwave dielectric resonators of cylindrical or spherical shape.

3.1 Dielectric resonators

A dielectric resonator is a piece of high-dielectric constant material, usually in the shape of a disk or sphere. This dielectric element operates as a miniaturized microwave resonator because of internal reflections of electromagnetic waves at the high dielectric constant material – air boundary. This results in a confinement of electromagnetic energy within and in the vicinity of the dielectric material. At microwave-to-millimeter wave frequencies, dielectric resonators can replace traditional, high-*Q* metal cavity resonators in many applications, because the *Q*-factor of a metal resonant circuit is proportional to its volume. These limitations are overcome by dielectric resonators (DR) due to the fact that their losses are dominated by dielectric losses (decribed by the loss tangent, see Eq. (3.1) below), and only to a small extent by metallic losses (in the walls of a metal housing surrounding the DR) or radiation losses (for unshielded or semi-shielded DRs). Dielectric losses have been improved constantly in course of refining material preparation methods such as single crystal growing or ceramic processing, whereas metal losses, with the exception of superconductors, have remained substantially the same. DRs can be made to perform similar to metal cavity resonators, but being smaller by a factor $\varepsilon^{1/2}$ (ε = permittivity of DR), light-weight, posses high-*Q*, are of low-cost and high reliability, posses high temperature stability and can be easily tuned in frequency.

3.1.1 Modes in cylindrical dielectric resonators

As in a conventional metal wall cavity, an infinite number of modes can exist in a dielectric resonator. As first approximation, a dielectric resonator can be explained as a hypothetical magnetic wall cavity, which represents the dual case of a metal (electric) wall cavity. Dielectric resonator can be divided into two categories with respect of modes which can accrue in it: resonators, utilizing fundamental and lower order electromagnetic oscillations, and resonators excited in a regime of azimuthally oscillations of a higher order (whispering-gallery modes).

The natural modes of a cylindrical sample of low-loss, dielectric material can be classified in the four categories

TE$_{nsm}$**, TM**$_{nsm}$**, HE**$_{nsm}$ and **EH**$_{nsm}$,

where *n* and *s* are integers which describe the wave patterns in the azimuthal (φ-coordinate in the cylindrical coordinate system) and radial directions (*r*-coordinate), respectively; *m* is an axial (along *z*-coordinate) wave number, which in general is a real number, reflecting the fact that the two circular boundary surfaces do not exactly contain an integer number of half

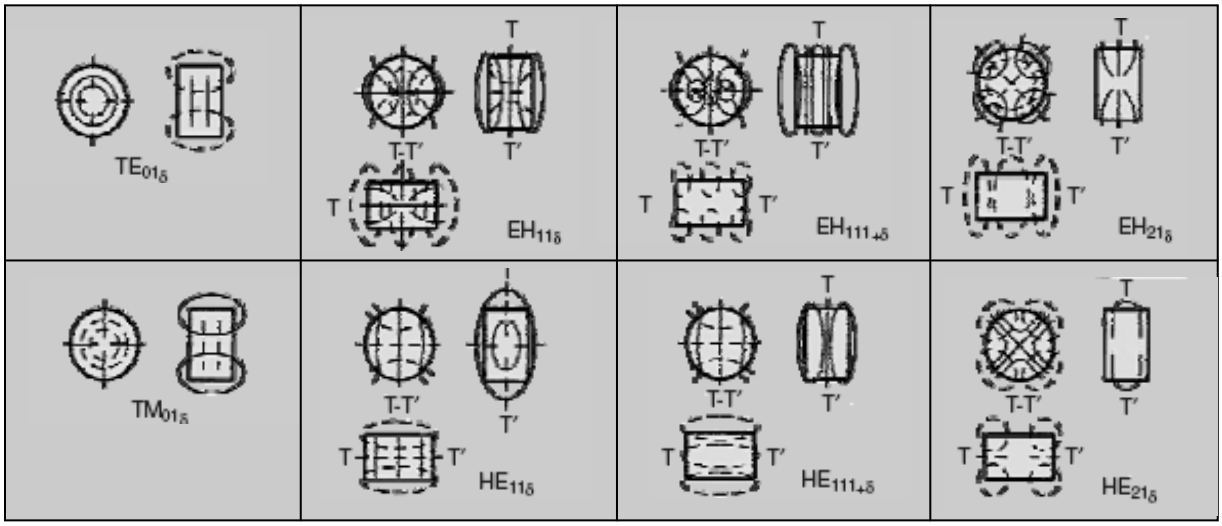

Figure 3.2 Modes in a dielectric resonator. The solid lines indicate electric field distribution and dashed lines – magnetic component field distribution [52].

wavelength as in metallic cavities. The mode number m is usually substituted by a Greek δ: $m = \delta, \delta+1, \delta+2,$ and assumes values in the range $\delta = 0.5–1.0$.

TE (transverse electric) and TM (transverse magnetic) modes do not contain electric and magnetic fields in the axial direction (z), respectively. HE and EH modes are called hybrid, because all six field components are present in both. HE (quasi TM) and EH (quasi TE) modes possess dominant magnetic and electric axial fields, respectively. Fig. 3.2 shows a sketch of the fields for the lowest order azimuthal modes.

The ratio between the DR diameter d and height h, d/h together with the external elements such as shielding cavity walls, tuning elements, holders and substrates determine which of the two fundamental modes $TE_{01\delta}$ or $HE_{11\delta}$ has the lowest resonant frequency. For most configurations the $TE_{01\delta}$ is the lowest mode when the aspect ratio is $d/h > 1.42$ [53]. For a majority of practical applications either the $TE_{01\delta}$ mode or $HE_{11\delta}$ mode is employed, including measurements of the dielectric properties of materials [54-56]. But it should be pointed out that the $TE_{01\delta}$–mode dielectric resonators have very large radiation losses therefore require metal shielding which leads to additional losses. Studies by J. Arnaud [57] show that applying higher order azimuthal modes or WG modes enable designers to employ larger-sized dielectric resonators at higher frequencies, say above 30 GHz, where fundamental mode resonators become very small to be effectively controlled. Such higher-order modes possess much smaller radiation losses and therefore allow for higher Q-factors.

Whispering-gallery modes (WGMs) in a dielectric resonator are high-order azimuthal modes, which exhibit special wave patterns with field variations in the direction of the curvilinear coordinate φ around the resonator axis. The wave undergoes multiple total internal reflections at the resonator boundary along the perimeter and becomes confined inside the resonator, giving rise to resonances. The important feature of total internal reflection is the presence of an evanescent wave outside the resonator very close to the boundary surface and

almost negligible radiation losses in high-order WGM resonators. An additional advantage of these modes in dielectric resonators with respect to lower order modes is an improved confinement of the electromagnetic field inside the DR and, consequently, higher *Q*-factors. Typically, for azimuthal mode numbers above 6 quality factors in the 10^4 to 10^5 range can be achieved in open unshielded resonator structures at room temperature, if low-loss single crystalline or ceramic dielectric materials are employed [58].

In general, the unloaded *Q* factor of a dielectric resonator can be written as,

$$\frac{1}{Q} = \sum k_i \tan \delta_i + \frac{R_S}{G} + \frac{1}{Q_{rad}} \tag{3.1}$$

where the $\tan\delta_i$ are the values of the loss tangent of the dielectric materials present in the resonator volume. The value of k_i describes the electric filling factors of the dielectric parts,

$$k_i = \frac{\varepsilon_i \int_{V_i} \vec{E}^2 dV}{\int_V \varepsilon(V) \cdot \vec{E}^2 dV}, \tag{3.2}$$

E the electric field distribution in the resonator where the total resonator volume *V* is composed of *N* sub-volumes V_i (dielectric parts of resonator or air) with permittivity ε_i. R_s is the surface resistance of the metal from which the shielding cavity is machined, *G* is a geometric factor accounting for the distribution of the magnetic field over the surface of the shielding cavity, and Q_{rad} the quality factor associated with radiation losses in case of an (semi) open DR.

Due to the high permittivity of many DR materials, the value of k_i *(i*=DR*)* is often close to unity such that the inverse loss tangent represents a limitation for the maximum achievable *Q*- factor.

Each WG-mode of azimuthal number *n* which accrues in the cylindrical specimen, for example Φ_c, can, depending on the way of wave excitation, have its orthogonal partner Φ_s. Both are characterised by the same (degenerated) resonant frequencies and quality factors, such that:

$$f_{rs}=f_{rc}, \quad Q_s=Q_c\,. \tag{3.3}$$

The dependencies of their electromagnetic fields on the angle φ are shifted along azimuthal direction by a quarter wavelength and are described by harmonic functions,

$$\Phi_S = \begin{Bmatrix} \sin(n\varphi+\psi) \\ \cos(n\varphi+\psi) \end{Bmatrix} \qquad \Phi_C = \begin{Bmatrix} \cos(n\varphi+\psi) \\ \sin(n\varphi+\psi) \end{Bmatrix} \tag{3.4}$$

where *n* is the azimuthal mode index; Ψ is an angle determined by the azimuthal position of the excitation source or any inhomogeneity, which disrupts the azimuthal symmetry. A typical behavior of $|\Phi(\varphi)|$ is shown in Fig. 3.3(a).

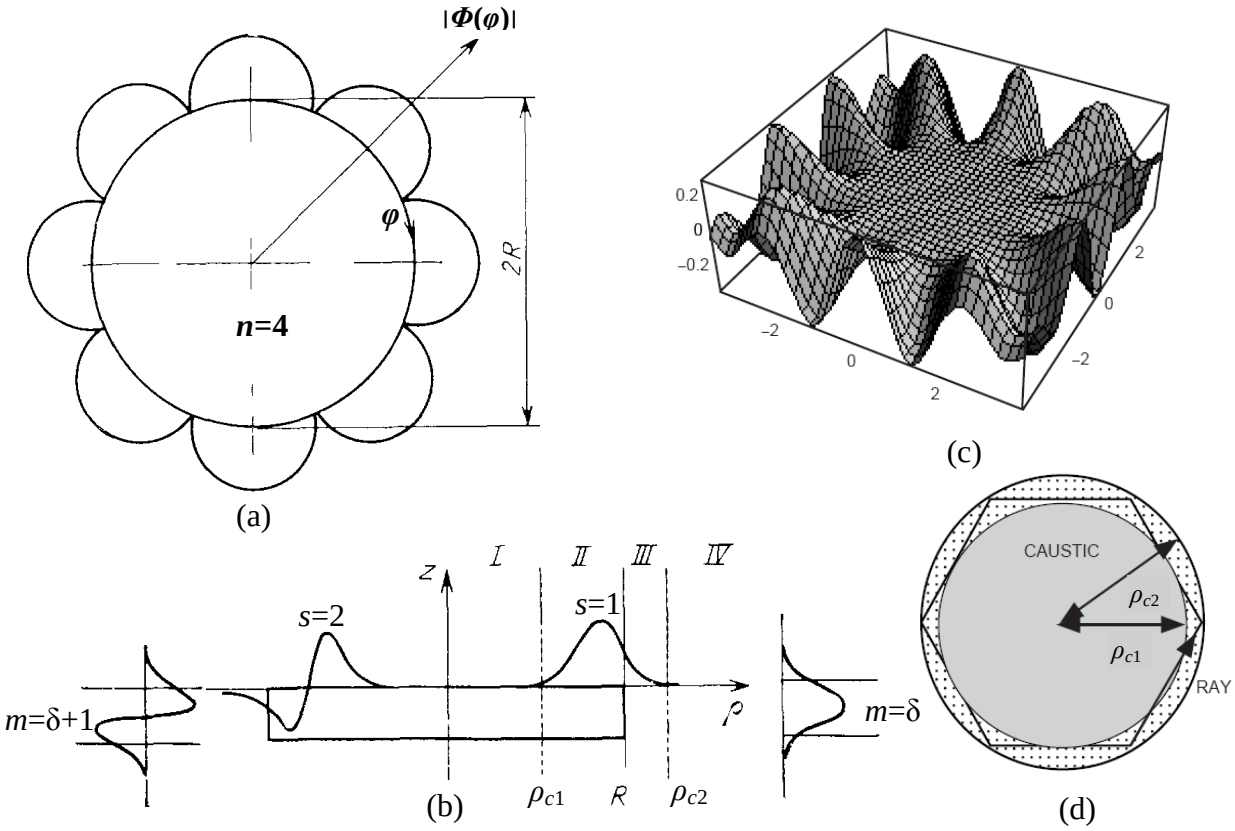

Figure 3.3 Distribution of the azimuthal waves along azimuth (a) and along radial and axial coordinates (b). (c) Three-dimensional EM-field presentation of $TE_{5,0,\delta}$. (d) Ray-tracing model of WGMs.

If the dielectric resonator structure is disrupted by the presence of some constructs, coupling elements or inhomogeneities in the resonator dielectric material, such that an azimuthal irregularity is introduced, the conditions (3.3) will be disrupted as well. Eigenmodes with the two kinds of azimuthal dependencies (3.4) will have different f and different Q, indicating that the two orthogonal modes are no more degenerated. This causes a frequency splitting of the eigenmodes, which becomes visible if it gets of the order or even larger than the resonant halfwidth determined by the quality factor.

The field distributions in z-direction and along the radius are shown in Fig. 3.3 (b). The radial distribution can be described by Bessel functions inside of the dielectric $\rho<R$ and by Hankel functions within the external area $\rho>R$. For the lowest order modes the radial dependences of the field are shown in Fig. 3.3 (b).

In order to explain the radial distribution of azimuthal waves we can use the concept of caustic surfaces (Fig. 3.3 (b,d)). A caustic is a boundary separating regions of wave and of "exciding, exponentially decaying" evanescent field character. Caustic surfaces are located in the areas which satisfy the condition $2\pi\rho_c\varepsilon_r^{0.5}=n\lambda$, partial radial waves propagate only at $\rho>\rho_c$. Therefore, caustic areas are the cylindrical areas with radii ρ_{c1} and ρ_{c2} including the physical boundary of the cylinder dielectric-air at $\rho=R$. They divide the space into 4 areas (I…IV) with different character of field distributions. The internal caustic has a radius:

$$\rho_{c1}=n\lambda/(2\pi\varepsilon_r^{0.5}) \quad (3.5)$$

In the region I, where $\rho<\rho_{c1}$, the field decays very quickly and the central part of the disk is almost free of field. At $\rho_{c1}<\rho<R$ (region II), the field has a character of a standing wave along the radius. At the boundary when $\rho=R$, the field distribution starts to alter due to the influence of the external caustic with a radius of:

$$\rho_{c2}=n\lambda/2\pi \quad (3.6)$$

Region III ($R< \rho<\rho_{c1}$) can be found inside of the external (outer) caustic, and the field decays almost exponentially. When $\rho_{c2}<\rho$, the field receives the character of an evanescent wave along the radius. An increase of the azimuthal index n, according to (3.6), moves the caustic of the resonator, decreasing the radiation losses from an open resonator structure.

Whispering gallery modes excited in a dielectric resonator form almost periodic sequences of the resonance response possessing amplitudes S_{21}^{ls} with increasing azimuthal mode index n, as shown in Fig. 3.4 (a) for s=1 and m=1. The amplitudes S_{21}^{hs} shown in Fig. 3.4 (b,c) represent corresponding sequences for higher values of the radial and the axial mode

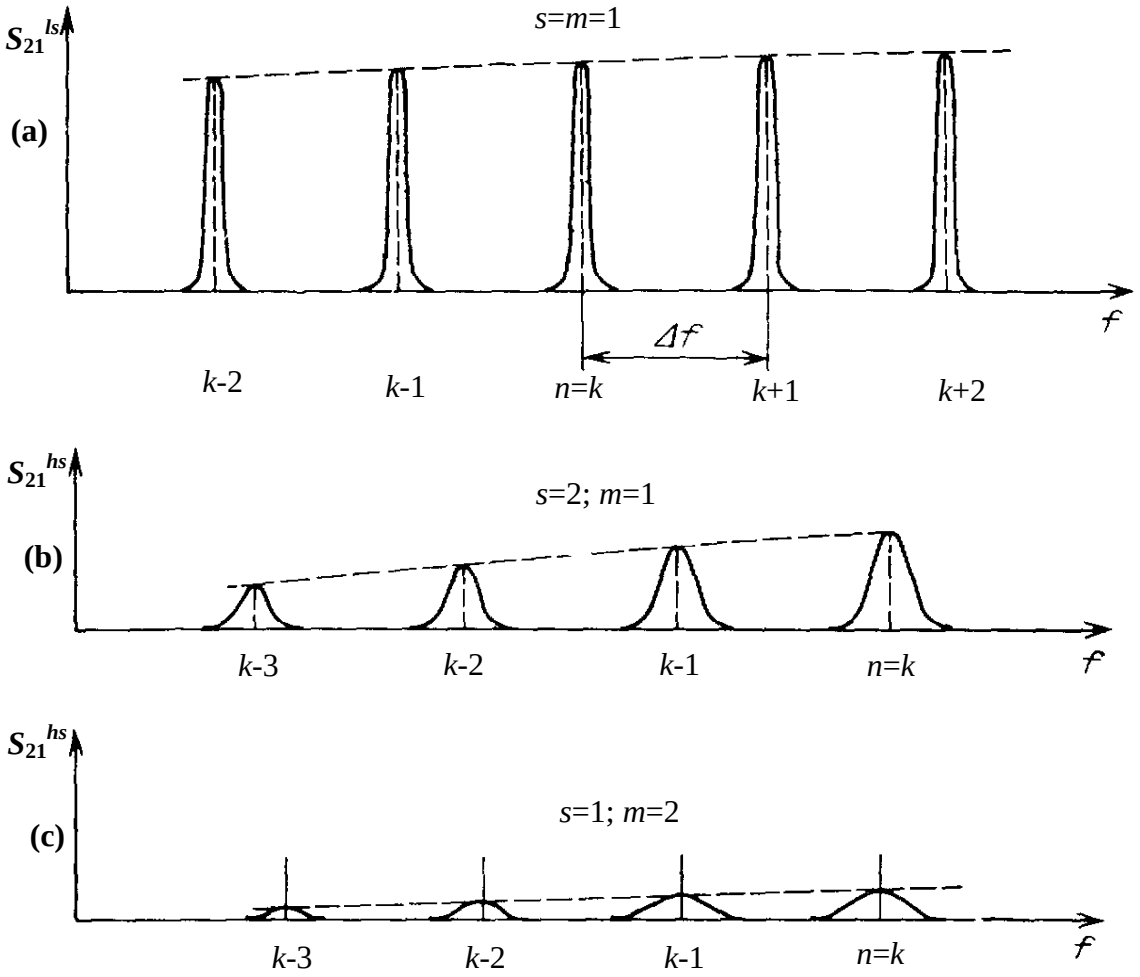

Figure 3.4 Mode spectra of a WGM dielectric resonator; s, m and n are mode indices along radius, height and azimuth, respectively.

number. All sequences of low and high mode numbers exist simultaneously, such that the reduction of the mode spectrum becomes a relevant issue. Due to some special instruments and procedures leading towards a reduction and discrimination of particular modes, in can be achieved that only one single high-*Q* mode remains isolated in a certain frequency range. This range is called the region of single-mode operation, which in the best case can reach values up to 15 to 35% of the resonant frequency.

3.1.2 Applications of dielectric resonators in microwave-to-millimeter wave technology

Dielectric resonators (DR) for micro-and-millimeter wave bands have been used to attain a reduction of device dimension, weight, and cost, simultaneously enhancing its performance, reliability, stability and functional potential. Microwave devices and systems utilizing dielectric resonators can be divided into 6 groups: dielectric resonator filters; devices utilizing DRs and ferrites; antenna devices; DR s in measurement setups; devices for microwave signal processing and solid-state oscillators with DR employed for frequency stabilization.

The most popular applications of DRs are high performance filters for satellite communication and base stations in cellular telephone networks, frequency stabilizing elements for low-phase noise oscillators as employed in satellite receivers (local oscillator unit) and point-to-multipoint high-performance wireless data links. The main advantages of DRs in such applications are low insertion losses (filters), low phase noise (oscillators), high frequency stability, particular with temperature, and small dimensions. For most commercial applications low-orders modes of DRs are employed [58].

Low-loss dielectric resonators operating on whispering-gallery modes in the microwave region have recently found more applications in devices as ultra-low-noise oscillators [59], power combiners and filters [60].

Measurement applications of DRs are resonators for measuring the surface impedance of unconventional metals such as superconductors [61,62] and real- and imaginary parts of dielectric permittivity of solids [55,56,63]. For such applications, the material parameters are usually extracted from the shift of resonance frequency and reduction of quality factor imposed by the sample under test. Whispering-gallery modes in cylindrically shaped DRs made from low-loss single crystals such as sapphire have been used to determine the anisotropic dielectric properties, in particular the extremely low losses at cryogenic temperatures [64,65].

So far, the results of a large number of investigations on dielectric resonators excited in WGM indicate a potential for their applications for investigation of liquids of arbitrary losses. Annino et al [66] constituted in their approach a relatively simple method of multifrequency EPR spectroscopy of high-sensitivity up to the THz regime. The utilized apparatus employs a novel combination of far infrared molecular lasers and of probe heads exploiting dielectric resonators working in whispering gallery modes. The same team [67] reports about the measurements of the electromagnetic parameters of WG dielectric resonators in the frequency range of 18-27 GHz and applications of these measurements to the determination of the

complex dielectric permittivity of the material forming the resonator itself and materials interacting with the WG dielectric resonator. In the second case dielectric properties of the interacting liquid materials (of low losses) were obtained by plunging the resonator in the liquid under test. Kirichenko et al. [68] developed a dielectrometer in form of a semidisk "image-DR" excited in WGMs by a diode module. A capillary tube of 0.08 ml volume was placed inside a hole in a semidisk at maximum of field intensity and filled with ethanol, kerosene, water, acetone and their mixtures. The measurement parameters such as frequency shift and change in the relative attenuation factor of the signal correlate with the dielectric properties of the liquids under test. Cherpak et al. [69] studied the electrodynamic properties of WGM resonators of two types with liquid-filled small cavities at K_a-band frequencies. One of the WGMR types is a two-hemidisc resonator with a diametrical slot in which a cuvette with a thin (0.01-0.1 mm) flat liquid layer is placed and the other is a disc resonator with a small diameter (0.3-2 mm) and liquid-filled cylindrical capillary.

The concept of WGMs with still acceptable dimensions for millimetre and submillimetre waves (much larger than that of fundamental mode in the same frequency range) can be employed from the low Gigahertz range up to optical frequencies and therefore provides a challenging approach for highly sensitive broadband investigation of liquids.

3.2 Sensitivity studies and optimization of WGM-resonators for liquid characterization

As already mentioned in the first chapter, water is one of the most common substances in the biosphere, it is the major component in any living system and therefore represents the main solvent for biochemical liquids and for biomolecules. Many biomaterials of scientific interest are often water-based fluids (blood, serum, physiological solutions, buffers, etc.). Water is characterized by its high dielectric losses and dielectric constant at micro- and millimeter wave frequencies (see, for example Table 1.2 in Chapter 1).

In most cases the investigated liquid solutions represent two-component (binary) water compounds, with complex permittivity depending on the solution concentration, which in turn can be utilized for concentration determination. The strong dependence of the dielectric permittivity of the solution ε^* on concentration is stipulated by high value of ε^* of the water-solvent in comparison to the permittivity of the dissolved substances in it. At the same time ε^* of the solution depends on its structure and intermolecular bonds. Approaches which allow to measure water-based, so-called lossy liquids of the smallest possible amounts down to pico-to-nanolitre volume are of great practical interest. The requirement for microlitre and submicrolitre measurements has become increasingly prevalent due to on-going technological advances in the life science. There is a need dictated by the potential applications range from the detection of particles of proteins or DNA (for label-free DNA analysis), analysis of organic solvents towards investigation of blood and tiny tissue samples, medical investigations of biochemical liquids. Chemical and biochemical methods for liquid characterization usually require volumes of at least several microlitres. Therefore, the physical methods described in this thesis have a potential for characterization of smaller volumes.

CHAPTER 3: ED PROPERTIES OF WGM RESONATORS WITH LIQUID INHOMOGENEITIES

Due to the high microwave losses of aqueous liquids even a macroscopic resonator allows for a high measurement sensitivity for nanolitres volumes, provided that its quality factor is sufficiently high. If a resonant structure is partially filled with a liquid, its resonant frequency and quality factor are altered depending on the values of real and imaginary part of permittivity $\varepsilon^* = \varepsilon' + i\,\varepsilon''$:

$$f_{res} = f_{res}\left(\varepsilon_{liq}', \varepsilon_{liq}''\right), \quad Q_{res} = Q_{res}\left(\varepsilon_{liq}', \varepsilon_{liq}''\right) \tag{3.7}$$

The problem of the electrodynamic analysis is that Eq. (3.7) cannot be simply inverted, i.e. the complex permittivity cannot be determined from the measured resonant frequency and quality factor in a straightforward way for any arbitrary geometry. The problem represents a serious challenge because fundamental difficulties arise in dielectric measurements of lossy liquids, which are inherent.

Any physical measurement can be carried in two different ways:

i) “absolute measurement”, i.e. the measurement with respect to basic physical quantities (mass, length and time),

ii) the measurement of physical properties using an apparatus which demands a procedure of suitable calibration with the help of reference samples of known properties.

The two main approaches which were developed in this work follow the two above mentioned measurement principles and allow a complementary study of solutions of nonorganic and organic molecules dissolved in water. These highly sensitive techniques are based on different modifications of whispering-gallery mode (WGM) dielectric resonators comprising local inhomogeneites filled with the liquid under test. Since this kind of resonator possesses extremely high values of the *Q*-factor, this approach becomes rather attractive because the available quantity of water-bio-substance solutions studied can be very small for high concentrations of bio-molecules.

In the first approach, we explore the use of open WGM cylindrical resonator with a local inhomogeneity in the form of a small droplet of the studied liquid of pico- to nanoliter volume. The introduction of a lossy liquid of such a small volume causes a small perturbation of the electromagnetic field distribution with a measurable change of resonator parameters at an operating resonance frequency of around 35 GHz. For such a case no rigorous solution of the eigen mode problem exist such that calibration measurements with reference liquids are required [7,8].

In particular for solutions, reference data are not always available in the literature. On the other hand, for the purpose to create “reference” data for liquids, reliable and a highly sensitive technique for absolute measurements are therefore required. The development of our second approach, we hope, can be considered as a response to one of the challenges of modern physics of liquids, which is an insistent necessity for the development of first principle measurement technique for lossy liquids. This is important, especially because “Reliable dielectric data is rather scarce and often one must glean where one can” [7].

For this purpose we employed a so-called radially two-layered (RTL) disk resonator shielded by two conductive metal end plates, which can be excited in whispering gallery modes with constant electric fields parallel to the cylinder axis (in TM WG-mode). The liquid is filled inside cylindrical volume embedded by concentric dielectric ring. Due to the rotational symmetry and *z*-independent cross section of this structure a rigorous solution of the electrodynamic problem exists, i.e. real and imaginary part of the liquid permittivity can be calculated by an analytical expression from the measured resonant frequency and quality factor. Therefore, we consider this technique as reference method for precise determination of the complex dielectric permittivity of aqueous solutions and other lossy liquids. However, this method needs a respectively large volume of liquid, for example $\pi(r_{innlayer})^2 \cdot h = \pi \cdot (3.5\text{mm})^2 \cdot 2.5\text{ mm} = 96 \cdot 10^{-9}\text{m}^3 = 96\mu\text{l}$ at 36 GHz for the resonator made of sapphire. Utilizing WG modes with the highest possible *Q*-factor (even despite a considerable decrease of *Q* due to the presence of metallic endplates) allows to prevent essential *Q*-factor degradation connected to high losses of millimeter wave radiation in polar lossy liquids under test.

3.2.1 Electrodynamic properties of WGM resonators with a liquid droplet on the resonator surface

As a first step in this approach, we studied the sensitivity which can be achieved by a WGM sapphire resonator for determination of the complex permittivity of a small liquid inhomogeneity in form of a small water droplet down to picoliter volumes, which can be spotted on the resonator surface.

Since the volume of the droplet is very small in comparison to the resonator volume, perturbation theory can be applied to describe the results and to optimize the resonator structures with respect to maximum sensitivity. Therefore Slater´s perturbation formula in its most general form for the case of nonmagnetic materials [70] is following:

$$\frac{\Delta f}{f} = -\frac{1}{4W}\int_{V_L}(\vec{D}_1^{\,*}\vec{E}_0 - \vec{D}_0\vec{E}_1^{\,*})dV = -\frac{\varepsilon_0}{4W}\left[\int_{V_L}(\varepsilon' \cdot E_1E_0 - E_1E_0)dV\right] \approx$$
$$\approx -\frac{\varepsilon_0 V_L E_0^{\,2}}{4W}\left[(\varepsilon' - 1)(E_1/E_0)\right] \qquad (3.8)$$

In Eq. (3.8), $\boldsymbol{D_1}$ and $\boldsymbol{E_1}$ represent displacement current and electric field with perturbation and $\boldsymbol{D_0}$ and $\boldsymbol{E_0}$ without, respectively, W is the stored resonator energy, $\varepsilon_0 = 8.85 \cdot 10^{-12}$ As/Vm, and V_L is the volume filled with liquid.

For the change of inverse quality factor, the incremental frequency rule applies [71], such that

$$\Delta\left(\frac{1}{Q}\right) = \left|\frac{\Delta f}{f}\right| \cdot \tan\delta \qquad (3.9)$$

with $\tan\delta = \varepsilon''/\varepsilon'$ being the loss tangent of the liquid.

In Eq. (3.8), the term in front of the brackets is called *filling factor*, resembling k in Eq. (3.2), which increases with increasing sample volume V_L, with increasing amplitude E_0 of the unperturbed electric field at the position of the sample, and with decreasing field energy W of the resonant mode. Within a series of modes, W is roughly proportional to the resonator volume, which depends on the permittivity of the dielectric resonator material ε_{res} according to $\varepsilon_{res}^{-3/2}$. However, the sensitivity for droplet detection is proportional to the ratio of liquid induced frequency shift divided by the resonant halfwidth, which decreases with increasing quality factor. For that reason, the selection of the resonator material and resonant mode is a trade-off between permittivity and achievable Q- factor.

In Eq. (3.8), the term in brackets accounts for a local field deformation by the sample. As simplification, the electric field strength at the position of the sample E_1 is assumed to be constant over the sample volume, but may deviate strongly from the unperturbed field. In case of a high permittivity liquid like water embedded in a low permittivity dielectric material, E_1 can be significantly lower than E_0. Therefore, the choice of dielectric material and the selection of mode have to be performed thoroughly and individually for each sensing arrangement. Perturbation theory in conjunction with numerical field simulations provides helpful support for the optimization procedure.

For most of the ceramic and single crystalline dielectric resonator materials, $\tan\delta$ scales linearly with increasing frequency. In particular, for frequencies above 35 GHz, sapphire represents a reasonable compromise, because of relatively high permittivity $\varepsilon'_{\perp}$=9.4, $\varepsilon'_{\parallel}$=11.59) and the lowest loss tangent of $9\cdot10^{-5}$ at 10 GHz [56]. Our investigation was performed at frequencies of 34-35 GHz, which lies slightly above the maximum of water absorption, and therefore provides suitable conditions for detection of small amounts of water with respect to a compromise of short wavelength and high water absorption.

In our preliminary investigation [72], we compared the electrodynamic properties of two sapphire resonators with slightly different diameters and essentially different heights in order to optimize the dimensions of the resonator-bioliquid sensor from the point of view of its sensitivity to the smallest droplet.

We selected modes from the $HE_{n1\delta}$ –family with nearly axially homogeneous electric field because of high field amplitude at the cylinder surface, relatively low density of the mode spectrum for azimuthal mode numbers $n \geq 7$ at which radiation losses are negligible. Fig. 3.5 shows the simulated distribution of the electric field for a $HE_{n1\delta}$ -modes with n = 7 in two sapphire resonators of slightly different diameters and essentially different heights operating the same resonant frequency of around 34.2 GHz. Simulations have been performed with CST Microwave Studio utilizing the Eigenmode-Solver. As seen from the details of the field distribution, the electric field inside the droplet is almost the same as without droplet, $E_1 = E_0$, such that the term in brackets in Eq. (3.8) is equal to unity.

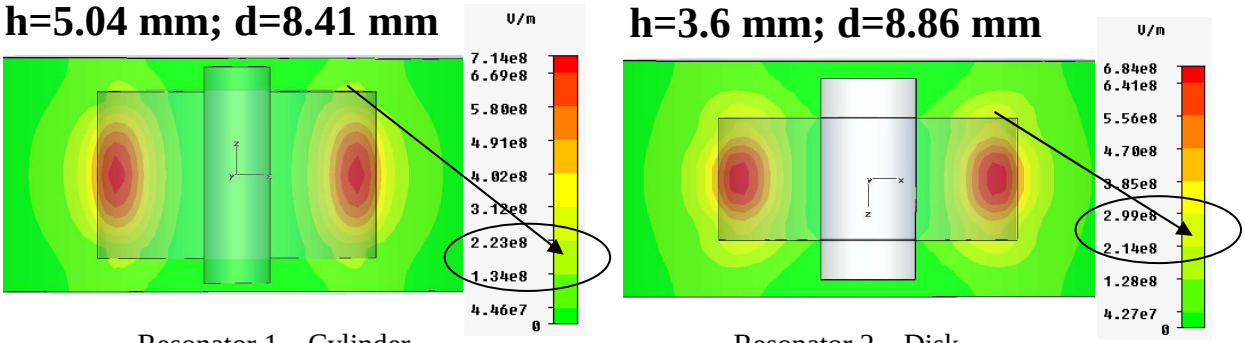

Resonator 1 – Cylinder Resonator 2 – Disk

Figure 3.5 Simulated electric field distributions (E_z-component) of the $HE_{71\delta}$ –mode in two sapphire resonators of different size.

Standing wave WGM excitation by lumped element coupling

For verification and experimental determination of sensitivity, we performed experiments with all-side polished sapphire resonators of abovementioned dimensions purchased from Crystec GmbH. Each of the resonator was placed inside a semi-open cylindrically shaped copper housing of dimensions D = 28 mm and H = 20 mm. In order to perform the droplet experiments, free access to the sensitive resonator surface from above is essential. We employed coupling of electromagnetic radiation from coaxial transmission lines into a dielectric resonator by means *coupling loops* (formed of a bent coaxial probe), which are mounted through holes in the semiopen metal cavity wall Fig. 3.6(a). This coupling allows to excite standing WGM-modes inside the dielectric cylinder by their magnetic fields. The measured quality factors were between 30 000 and 37 000, limited by the dielectric losses of sapphire.

For droplet positioning we utilized a 2D-scanning table and 1D-automated microprocessor controlled microinjection pipette delivering precise nanoliter volumes. The volume of the smallest droplet produced by the available pipette and detected by our system was about 90 picoliters.

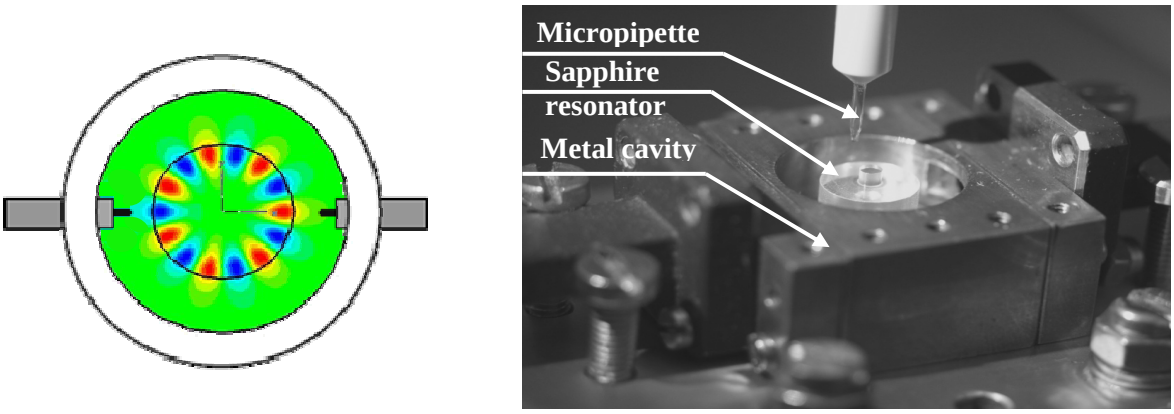

(a) (b)

Figure 3.6 Semiopen metal housing confined sapphire resonator of dimensions d=8.41 mm, h=5.04 mm and coupling. (a) Simulated standing wave field distribution of the E_z component. (b) Photograph of one of the developed resonator devise placed under the microinjection pipette during spotting.

The properties of the droplets can be determined from the induced change of resonant frequency and losses according to Eqs. (3.8) and (3.9). Experimentally, droplet induced losses were determined from the changes of the inverse quality factor $\Delta(1/Q_{liq\text{-}air})$ by using the equation

$$\Delta\frac{1}{Q_{liq-air}}=\frac{1}{Q_{liq}}-\frac{1}{Q_{air}}, \tag{3.10}$$

where $Q=f_r/\Delta f_{1/2}$ was determined from the resonance frequency f_r and the halfwidth $\Delta f_{1/2}$. Although the so-called "3 dB" method is used often to determine Q, more accurate results we obtained by fitting the resonance curve to a Lorentzian [73].

In order to find the most sensitive areas on the resonator surface, we spotted small water droplets of about 2 nl volume at different positions on the surface of the resonator. The measurement results are presented on Fig. 3.7 as droplet induced change of the inverse quality factor. In Fig. 3.7(a) the droplet position was varied along the semicircle of the resonator in azimuthal direction on the flat surface of the sapphire cylinder at a radial position of maximum electric field. The dependencies shown in Fig. 3.7(b) are the radial dependencies measured for a droplet position being fixed at the maximum of the azimuthal field distribution. The dependencies shown in Fig. 3.7 exhibit a very good agreement with the petals in Fig. 3.6 (a) representing the simulated field distribution of the $HE_{71\delta}$ WGM, which was excited in the resonator. The 7 maxima depict the most sensitive areas for droplet positioning which correspond to 7 antinode areas of the field distribution along the semicircle of the disk. According to Fig. 3.7 resonator 2 of smaller height (disk resonator) is more sensitive because the field at the droplet position is higher than for resonator 1. The ratio of measured frequency shift for a fixed droplet volume for the two resonators roughly corresponds to the ratio of their calculated square of the electric field (numbers at false colour scale in Fig. 3.5) at the field maximum, as expected by Eq. (3.8). Even the absolute values of the measured frequency shift agree well with values predicted by Eq. (3.8), providing the value for the total field energy of W = 1J, which is employed internally by the Microwave Studio software as the basis for the depicted false colour scale in Fig. 3.5.

A practical application of the spotting-positioning system is the identification of modes in dielectric resonators by probing the field distribution with a water droplet. This is sometimes a difficult task, which can be successfully solved by this method.

For the purpose of optimizing the amount of liquid under test we have measured the dependencies of frequency shift and loss variation on the water droplet volume. Fig. 3.8 shows the measured droplet induced changes of resonant frequency and inverse quality factor as a function of the number of droplets of about 90 pl volume each, i.e. as functions of the water volume, for both resonators. The droplets were spotted at the most sensitive positions on the surface corresponding to maxima on the position map defined by the simulation

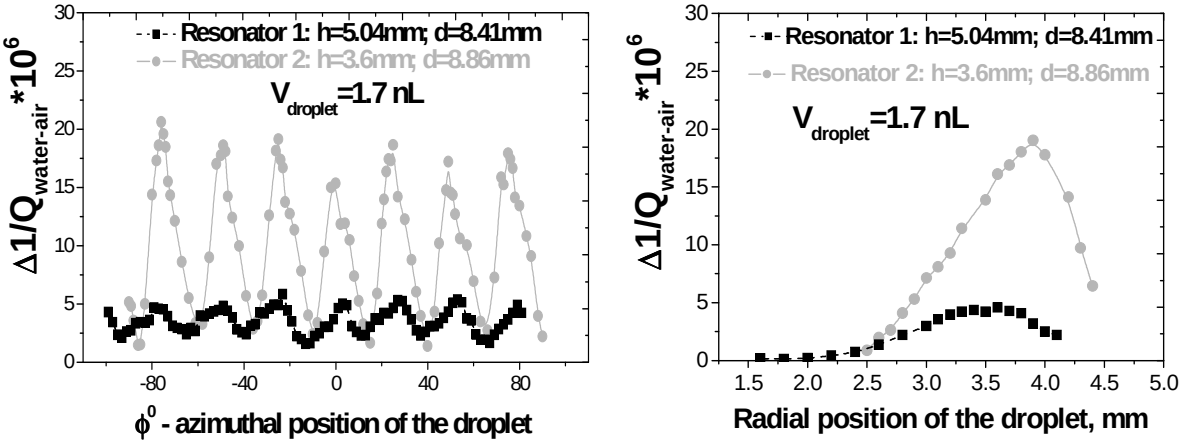

Figure 3.7 Measured droplet induced change of inverse quality factor when the droplet position is varied in (a) azimuthal and (b) radial directions.

(Fig. 3.6 (a)) and the experiment (Fig. 3.7). The results indicate almost linear dependencies for both resonator parameters (frequency shift and loss variation) on the number of droplets, within the range of small droplets up to 2.5 nl, which is expected by perturbation theory (see Eq. (3.8)). This can be convenient for calibration of our method with the help of reference liquids in order to obtain the complex dielectric permittivity of an unknown liquid.

For further verification of perturbation theory, we compared the measured values of frequency shift and shift of inverse quality factor. For a volume of 3 nl, $\Delta f/f = 1.76 \cdot 10^{-5}$ and $\Delta(1/Q) = 2.4 \cdot 10^{-5}$. According to Eq. (3.9), the ratio of $\Delta(1/Q)$ and $\Delta f/f$ should be equal to $\tan\delta$ of water, the resulting value of 1.36 agrees with the values of 1.46 (see Table 1.2 from Chapter 1) from broad band measurements. Due to the linear volume dependences this ratio enables - in some limits - a volume independent identification of unknown liquids by their loss tangent - independent of the liquid volume.

Although the resonator size is relatively large, the induced change of inverse quality factor by a single droplet of 90 pl volume could be clearly detected. We expect that the sensitivity can be increased by a further reduction of resonator height, which could be compromised by a reduction of resonator quality factor.

In Fig. 3.8(a) the experimental results on the induced change of resonant losses which were obtained by fitting the resonance curve to the Lorentzian are shown in the form of closed diamonds and circles on solid lines.

As an alternative method providing even higher accuracy for the smallest droplets changes of the quality factor were determined by measuring the decrease of the amplitude of the resonant curve at $f = f_r$,

$$\Delta\frac{1}{Q_{liq-air}} = \frac{1-10^{(\alpha_{air}-\alpha_{liq})/20}}{Q_{air}\cdot 10^{(\alpha_{air}-\alpha_{liq})/20}} \tag{3.11}$$

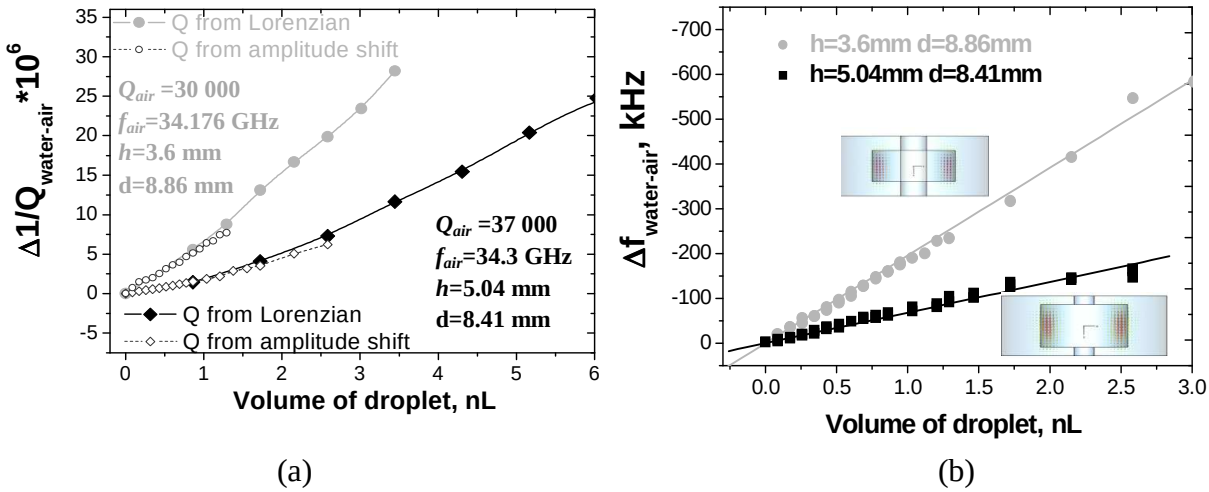

(a) (b)

Figure 3.8 Measured droplet induced changes of inverse quality factor (a) and resonant frequency (b) for the cylindrical and disk resonators superimposed in one plot as a function of water volume (each point corresponds to an integer multiple of 90 pl).

where $\alpha_{air} - \alpha_{liq}$ is the difference between the amplitudes in dB. In this case the measured data are presented as open diamonds and circles on the dotted lines.

So far, first results with WGM resonators at 34.2 GHz with quality factors *Q* of 30 000–37 000 revealed sufficient sensitivity for the detection of a single water droplet of 90 picolitres volume. Both resonators were shielded in semiopen metal housing and standing waves were excited by lumped element coupling, as it was clearly shown by azimuthal dependence in Fig. 3.7(a). This kind of coupling is efficient in the microwave region. However, at millimeter- to – submillimeter-wave frequencies lumped elements of the coupling are too small to be effectively adjusted and controlled.

Excitation of nearly running waves by a distributed quasioptical coupling

The utilization of higher frequencies leads to a reduction of resonator dimensions and correspondingly, to a smaller minimum droplet volume which can be sensed by the system. Apart from that, the use of higher frequencies may provide additional information on the properties of a liquid substance. The excitation of standing WG waves in dielectric resonators shielded by semi-open metal housing (Fig. 3.6 (a)) is limited to frequencies below about 100 GHz. In addition, integrated resonator arrays cannot be realized in this manner. Therefore, we have developed and optimized a scheme for distributed coupling of completely unshielded dielectric resonators by dielectric image waveguides, which can be scaled towards the terahertz frequency range and allows even multi-resonator excitation.

The dielectric image line has received renewed interest in recent years for millimeter-wave integrated circuits [74]. Many passive and active millimeter-wave devices have been developed in dielectric image line technologies [75]. The reason for this interest is that, in the regions from millimeter wave to optical waves, the metal wall structures cause attenuation due to skin effect loss. This conduction loss is proportional to the square root of the frequency. Since the dielectric image line is not enclosed by the metal wall, the conduction

losses are caused by only one metal image plane. This metal plane may also provide a heat sink and is convenient for dc biasing of integrated circuit devices. Another source of attenuation is absorption due to the dielectric material. This dielectric loss depends on the loss tangent and the dimension of the dielectric material. In practice, however, the cross-sectional dimensions of the dielectric become rather large in order to confine most of the energy within the dielectric.

From point of view of low losses, pure dielectric waveguides without image plane are even superior, and represent the method of choice for excitation of WG resonances in single resonators at submillimeter wave frequencies. On the other hand, for integrated circuits image guides are easier to integrate on a dielectric substrate and are more compact in size, which is advantageous for the microwave experiments performed in the frame of this thesis.

The rectangular dielectric image line, as depicted in Fig. 3.9 (a), consists of a rectangular dielectric core with relative dielectric constant ε_r, surrounded by a semi-infinite medium of dielectric constant ε_0 (usually air) and the metal image plane attached to the dielectric core. This image line can support a discrete spectrum of guided modes E^x_{mn}; and E^y_{mn}: (m=l,2,3,. ... n=l,3,5,. . .), and also a continuous spectrum of unguided modes. The subindices m and n indicate the number of half cycle variations each field component has within the dielectric core. The main transverse field components of the E^y_{mn} modes are E_y and H_x. The dominant mode is the E^y_{11}, mode, as shown in Fig. 3.9 (b), whose field variation is given by a cosine function, and outside the dielectric core (on top and on both sides) the fields decay exponentially.

A theoretical analysis of rectangular dielectric image line propagation characteristics was initially described by Toulios and Knox [76]. The wavelength of the guide depends on the normalized guide dimension

$$B = \frac{4b}{\lambda_0}\sqrt{\varepsilon_r - 1} \tag{3.12}$$

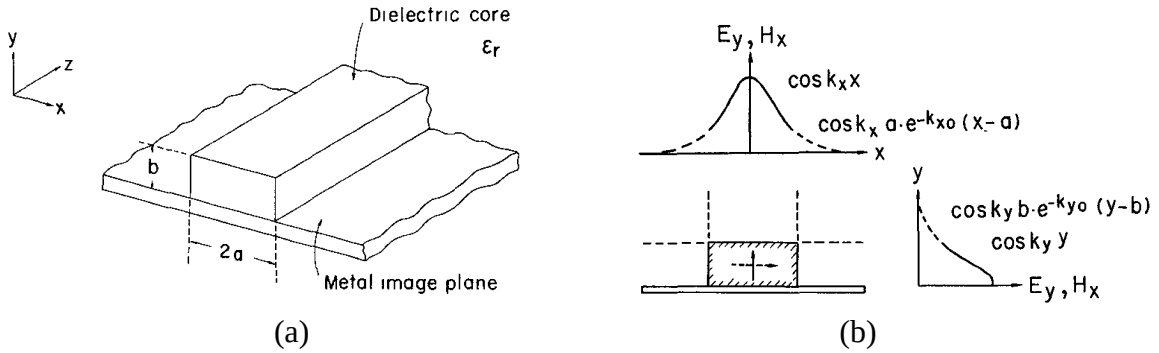

(a) (b)

Figure 3.9 (a) Rectangular dielectric image line. (b) Rectangular dielectric image line field distribution.

with λ_0 being the free space wavelength. The guide wavelength for B=1.108 has been determined from the graphs presented by [75] for a dielectric core having a cross section of $2a \cdot b$ with a/b = 1. Under this condition the one mode regime can be attained over a wide frequency range. This particular image guide is equivalent to a rectangular dielectric waveguide in free space with aspect ratio a/b=1.

The dielectric image waveguides applied for excitation of our resonators in the K_a frequency band were made of Teflon (ε_r=2.01) and had dimensions of b = 2.5 mm and $2a$=4.6 mm calculated on the base of the Eq. (3.12). The field distribution of the fundamental mode in the image guide shown in Fig. 3.9 (b) is similar to the distribution of the $HE_{n1\delta}$ mode in the dielectric resonator in axial (z) direction and along the radius as shown in Fig. 3.3 (b). Coupling between the image guide mode and the WGM in the sapphire resonator disk is achieved by the overlapping evanescent fields of both. For verification and optimization, we employed CST Microwave Studio to simulate an open resonator structure coupled by dielectric image waveguides in a transmission type configuration. One more advantage of utilizing the dielectric waveguide excitation in comparison to coupling loops in a metal housing is that dielectric waveguides allow additionally to select the modes to be excited in the resonant structure. In the coupling configuration shown on the Fig. 3.10, only $HE_{n1\delta}$ type modes can be excited. Similar to the loop coupling experiments, two different resonators were employed, each being placed between the input and the output waveguides. The first one was so-called resonator 2, or the sapphire disk with dimensions h=3.6 mm, d=8.9 mm which we used in our preliminary loop coupling experiment. The excitation of the $HE_{n1\delta}$ (n=7) mode in this resonator is demonstrated by the simulation shown in Fig. 3.10 (a).

The tilted ends of the waveguides shown on Fig. 3.10 represent a cut which allows fixing an absorbing material (usually carbon based) at the tilted plane of the waveguide. With such a configuration, the portion of field energy, which is not coupled from the upper waveguide to the resonator, is absorbed such that reflections and hence standing waves on the dielectric image guide are minimized. The angle of this tilted cut should be selected such that the tapered waveguide end is at least five times as long as the wavelength. Such matched loads allow to selectively excite running wave type whispering gallery modes.

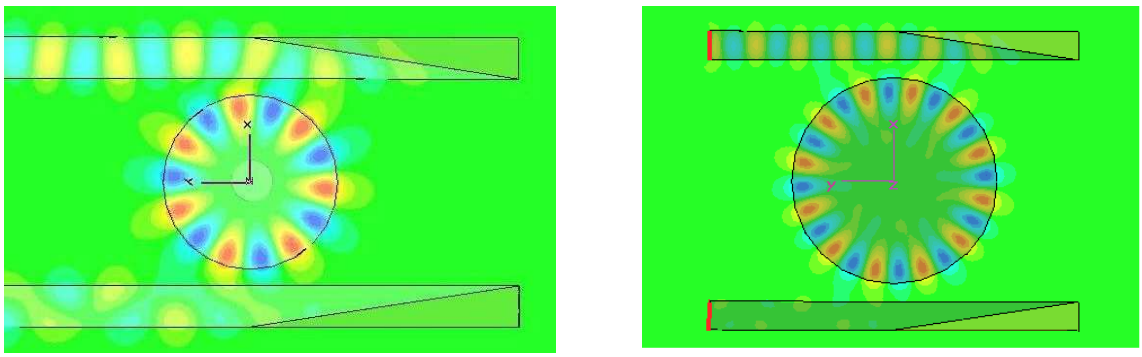

Resonator 2 (a) Resonator 3 (b)

Figure 3.10 Simulated distribution of the electric field amplitude at resonance. (a) Resonator 2 excited in $HE_{n1\delta}$ (n=7), dimensions h=3.6 mm, d=8.9 mm; (b) Resonator 3 excited in $HE_{n1\delta}$ (n=12), dimensions h=2.5 mm , d=14.5 mm.

Experimentally, the two waveguides were arranged slightly tilted with respect to each other rather than parallel like shown in Fig. 3.10, such that the coupling strength (defined by the minimum distance between the guide edge and the circumference of the dielectric resonator) could be adjusted by moving the dielectric resonator between the two waveguides (or by moving the waveguide assembly with respect to a fixed dielectric resonator).

Experiments performed in this way revealed a quality factor of only 25000 for the open resonator 2 without any shielding, which is smaller to the value 30000 measured in the semi-open housing with loop coupling. This reduction with respect to the ultimate value defined by the dielectric losses in sapphire is expected due to the influence of radiation losses.

In order to obtain higher quality factors for an open structure without any shielding, we tried to utilize modes with azimuthal index $n \geq 10$. As an example, a new resonator, so-called resonator 3, was excited in the $HE_{n1\delta}$ (n=12) mode with the field distribution shown on Fig. 3.10 (b). For the operating frequency of 35 GHz the manufactured sapphire cylinder has a

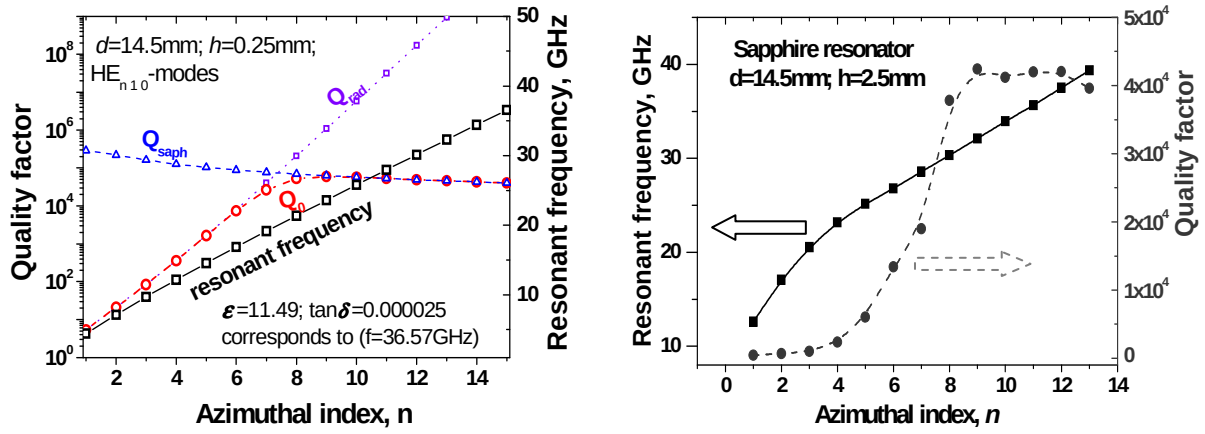

(a) (b)

Figure 3.11 Dependencies of quality factor and resonant frequency of the resonator 3 as a function of azimuthal mode number n calculated on the base of model described in Appendix A (a) and corresponding experimental results (b).

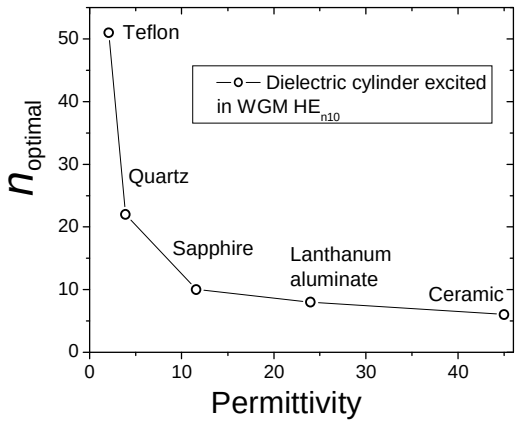

Figure 3.12 Dependence of the optimum azimuthal mode index on the permittivity of the dielectric resonator material for which radiation losses can be neglected (corresponding to the onset of the plateau in Fig. 3.11) at a fixed frequency of 35GHz.

much larger diameter of d = 14.5 mm. The height of h = 2.5 mm was chosen to be even smaller than in case of resonator 2, without significant affecting of Q-factor. This provides a quite high sensitivity for our liquid measurements. Fig. 3.11 shows the measured and calculated resonator parameters as functions of mode number n. The highest measured Q-factor for the open resonator was as much as 40 000.

The calculated dependence of Q_0 (open circles) was obtained as a sum of two constituents: Q_{sapph} (open triangles) – Q-factor which describes losses in the sapphire, dielectric material of the resonator, and Q_{rad} (open squares) corresponds to radiation losses in the resonant structure. At some optimum azimuthal number $n_{optimal}$ the radiation losses become negligible and the Q-factor of the resonator is equal to the Q_{sapph} and does not improve anymore with increase of n. The value of optimum azimuthal index varies with the dielectric properties of the dielectric resonator material. Fig. 3.12 shows that this index decreases with increasing permittivity of the resonator material.

In the case of the resonator excitation by distributed coupling elements based on dielectric waveguides possessing high directivity, both degenerated modes $\Phi_s(\varphi)$ and $\Phi_c(\varphi)$ appear to be shifted by 90°, such that the net wave will be a running wave propagating around the dielectric disk either clock or counterclockwise.

$$\Phi_r = \cos(n\varphi + \psi) \pm i\sin(n\varphi + \psi) = e^{\pm i(n\varphi+\psi)} \tag{3.13}$$

The angular propagation constant k is equal to integer number of waves n at the resonant frequency. The multiple superpositions of these waves produce interference effects, such that at the resonance the net amplitude increases abruptly. This resonance becomes noticeable by a significant change of the transfer ratio of the waveguide coupled via the dielectric disk. When the matched loads terminating the dielectric feedlines are properly implemented, reflections from the resonant structure are absent. Such resonance regime is called the running wave regime. If this regime can be realized practically, it can give us one more advantage to improve our liquid-detection measurements: the positioning of the small liquid droplet becomes independent on the azimuthal coordinate and we have to choose the position of the droplet only in radial direction, which is more convenient. Thus, if we extend our approach to higher frequencies, where the resonator dimensions are smaller, the search for the most sensitive point for spotting of the droplets becomes easier. In the ideal case of a running wave we will have the same response and correspondingly equal sensitivity along the azimuth direction at a fixed radial coordinate of the droplet.

In order to verify the advantages of running wave for droplet excitation, the azimuthal dependencies of the change of the inverse quality factor corresponding to losses induced by the droplet was measured for resonators 2 and 3 operating in the same frequency range (34-35 GHz) at T≈18°C [77]. Fig. 3.13 shows the measured values when the droplet position was varied along azimuth (along the semicircle of the disk) at a fixed radial coordinate corresponding to the maximum strength of the electric field.

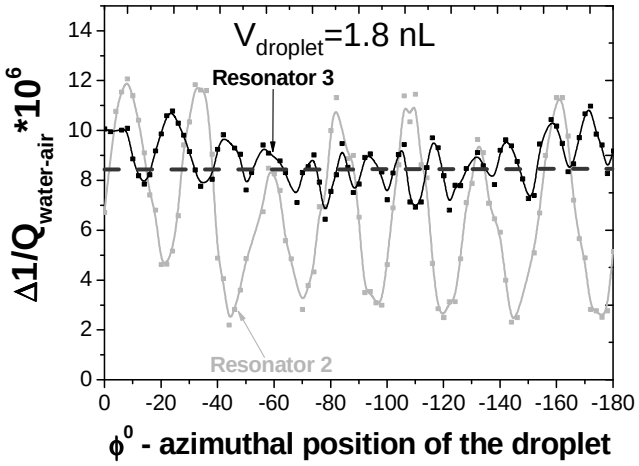

Figure 3.13. Measured water droplet induced change of inverse quality factor as a function of the droplet position varied in the azimuthal direction for two different resonators: Resonator 2 excited in $HE_{n1\delta}$ (n=7) with dimensions of h=3.6 mm, d=8.9 mm, Q=25 000; Resonator 3 excited in $HE_{n1\delta}$ (n=12) with dimensions of h=2.5 mm; d=14.5 mm, Q=40 000.

The experimental dependencies shown in Fig. 3.13 describe very well the calculated $HE_{n1\delta}$ field distribution (Fig. 3.10) excited in both resonators. Seven maxima and minima in the dependence for resonator 2 WG are strongly separated, which demonstrates the propagation of standing waves in the open resonant structure excited by the distributed coupling elements, in contrast to our expectation.

The azimuthal dependence for resonator 3 measured for a droplet of 2nl volume still resembles the features of an azimuthal mode number n=12, but the modulation depth is only about 20% of total inverse Q change. This indicates that the excited WGM is primarily of running wave character and that a high sensitivity for droplet detection can even be achieved in positions of the minima of the azimuthal electric field distribution.

As an explanation for the observed difference for both resonators, it is apparent from Fig. 3.10 (a) that the excitation of resonator 2 is similar to coupling loop excitation, since the field of the dielectric waveguide interacts efficiently with only one petal of the field in the resonator (the curvature of the resonator 2 is larger with respect to waveguides than in case of the resonator 3). In result, this leads to a dominant standing wave formation. In resonator 3 the directivity of the running wave is stronger pronounced due to the simultaneous interaction of the waveguide field with several petals of the resonator field.

As a summary, the field distribution determined experimentally by the droplet induced change of the inverse quality factor and shift of resonant frequency for resonator 3 are illustrated in Fig. 3.14. The results confirm that both the frequency shift and the losses show a similar behavior. The radial dependencies for both resonator characteristics at a fixed azimuthal position of maximum of electric field are inserted in Fig. 3.14 and reflect the radial distribution of the square of the electric field E^2. Further optimization of the dielectric waveguides and matched loads should further increase the running wave portion and may provide a more uniform dependence of the field amplitude on the azimuthal coordinate

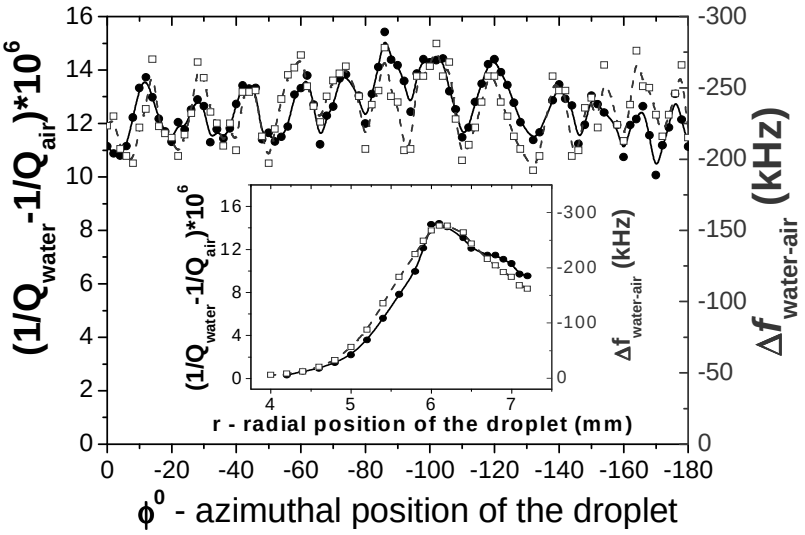

Figure 3.14 Water droplet induced changes of inverse quality factor $1/Q_{wat}$–$1/Q_{air}$ (solid circles) and resonant frequency $\Delta f_{wat\text{-}air}$ (open squares) as functions of the droplet position for resonator 3. The droplet position was varied in the azimuthal direction at a fixed radial position r=6.1 mm. Insert: the radial dependence for the same parameters at a fixed position of azimuth φ=86°. The volume of water droplet was 1.8 nl (T=18°C).

approaching the red dashed line symbolizing a 100% running wave propagation in the resonator structure.

In order to optimize the amount of liquid to be tested by resonator 3, we have measured the dependencies of frequency shift and loss variation on the volume of the water droplet. For that purpose, droplets of different volumes were spotted onto the resonator surface at a position of maximum electric field, according to our simulated (Fig. 3.10 (b)) and experimental (Fig. 3.14) maps.

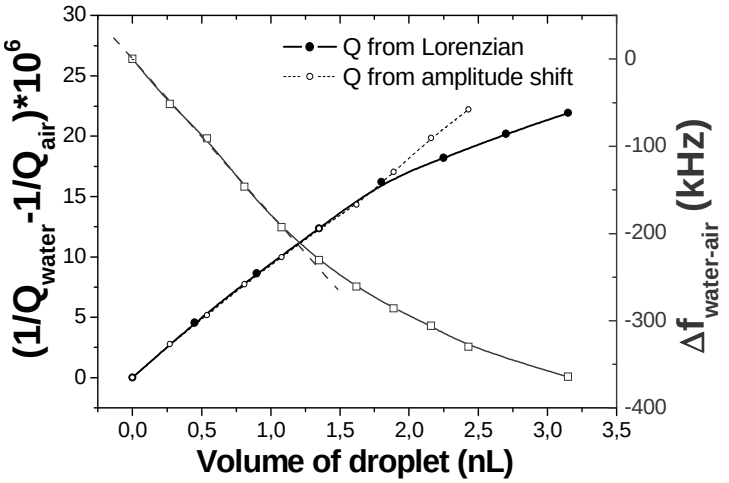

Figure 3.15 Measured water droplet induced changes of resonant frequency $\Delta f_{wat\text{-}air}$ (squares) and inverse quality factor $1/Q_{wat}$-$1/Q_{air}$ (circles) as functions of droplet volume (T=18°C) for resonator 3.

The results shown in Fig. 3.15 indicate almost linear dependencies of both frequency shift and loss variation on the droplets volume for droplets smaller than 2 nanoliters. For larger volumes, the observed sublinear behavior can be explained by the fact that the droplet extends over a large surface area such that the field inhomogeneity should be taken into account (see Fig. 3.10 and 3.14).

Finally, we compared the response from the two resonators 2 and 3 when spotting diluted aqueous solutions onto the sensitive points on the surfaces of each resonator. Fig. 3.16 shows the experimental volume dependencies of resonant frequency shift and loss variation for diluted aqueous solutions of ethanol in bidistilled water for 10% and 20% volume concentration compared with the volume dependence for water as reference liquid. The results indicate that both resonators allow us to distinguish concentrations below 10% of ethanol in such small volumes.

From point of view of sensitivity, both resonators are almost equal. For the investigation of biochemical liquids of interest resonator 3 was chosen, because it allows to obtain more reliable results due to higher *Q* and much less noisy resonance response.

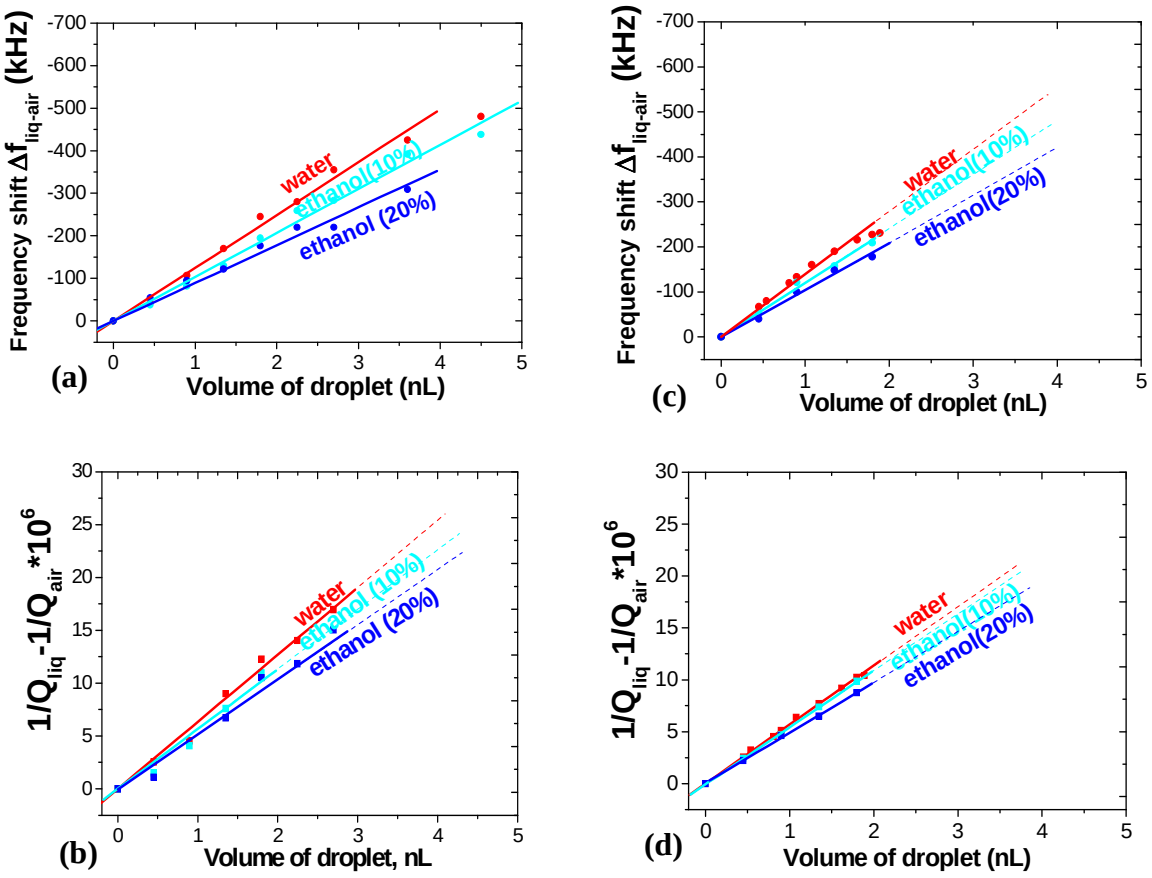

Figure 3.16 Droplet induced change of resonant frequency (a) and inverse quality factor (b) measured for resonator 2 and change of resonant frequency (c) and inverse quality factor (d) measured for resonator 3 as functions of volume of bidistilled water, and binary mixtures of 10% and 20% volume concentration of ethanol in bidistilled water.

3.2.2 Electrodynamics of the radially two-layered disk WGM resonator with liquid internal layer

Finally, the electrodynamic properties of the layered WGM resonator with conducting end plates (CEP) is discussed, which was employed for calibration measurements of reference liquids. The employed resonator configuration is depicted on the Fig. 3.17(a) representing a structure consisting of a dielectric disk sandwiched between two conducting metal end plates. The analysis of the field distribution in this geometry allows to calculate resonance frequencies and quality factors by analytical expressions depending on the complex permittivity of the dielectric disk material, the conductivity of the conducting endplates and the physical dimensions. For the first time such a structure was investigated in 1999 [78]. WGMR implemented in a form of the disk of uniaxial crystal with metallic end plates was theoretically investigated in [79]. In fact, such a structure represents a quasioptical analogue of the Hakki-Coleman resonator configuration [80], where the TE_{011} mode is excited in a dielectric cylinder clamped between two metal plates. Similar configurations have been used for measuring the surface impedance of normal or superconducting metals, provided that the loss tangent of the dielectric resonator material is known with sufficient accuracy [81], [62]. In reverse, the Haki-Coleman method can be used to determine the dielectric properties of the dielectric disk material, if the conducting properties of the metal endplates are known [82,83]. Alternatively, lossy liquids were used as dielectric disk such that WG modes were excited directly in liquids.

The rigorous solution for the resonator with conducting endplates also exists when the resonator has a laminated structure along the radius. In the present work, we consider a structure consisting of two concentric radial layers (Fig. 3.17(b)). The first internal layer of this resonator structure is the liquid under test, and the second external layer is a dielectric ring made of a solid dielectric material with known complex permittivity, such as Teflon, sapphire, quartz, or a common microwave ceramic. This ring shaped external layer also provides the confinement of the liquid inside the resonant structure. Measurements of dielectric permittivity of different liquids with a large variety of dielectric properties rely on the possibility to select the suitable *Q*-factor by optimizing the diameter of the internal liquid layer.

The real part of permittivity ε'_{liq} of the liquid arises by the comparison of experimental and simulated mode spectrum, if the permittivity of the external layer is known. At the same time, it is necessary to solve a number of problems under the condition of the known dispersion equation and field structure being implemented in a computer program, i) to calculate ε'_{liq} and ε''_{liq} (or $\tan\delta_{liq} = \varepsilon''_{liq}/\varepsilon'_{liq}$) of the liquid by a computer program from the measured resonant frequency and *Q*-factor; ii) to identify the oscillation modes employed for the measurements; and iii) to optimize the resonator dimensions from the point of view of highest measurement sensitivity. The latter is especially important to achieve a high precision for reference data of lossy liquids.

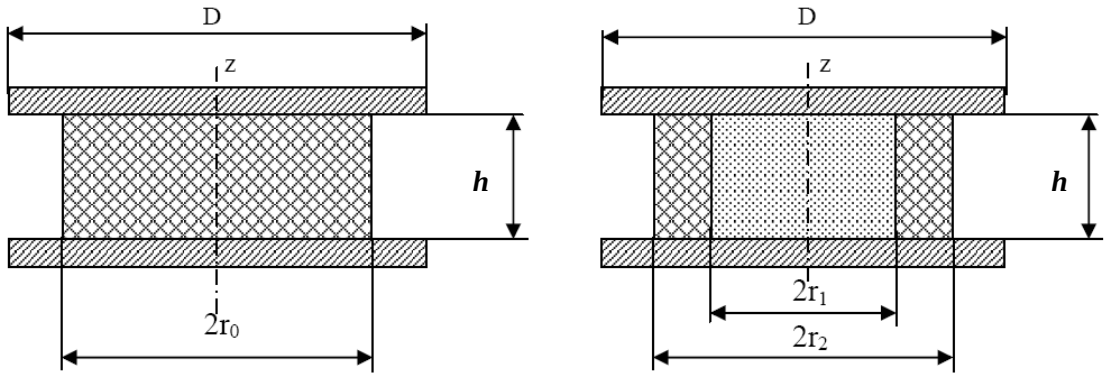

(a) (b)

Figure 3.17 (a) Cylindrical quasi-optical dielectric resonators with conducting endplates. (b) Radially two-layered quasi-optical dielectric resonator with conducting endplates.

Electrodynamic properties and optimization of the radial two-layered resonator

In order to optimize the dimensions of the resonator we carried out experimental studies with different liquids various values of the internal radius r_1, which is the radius of internal liquid layer. For this purpose the external layer or dielectric ring was made of Teflon. Teflon was chosen because it is machined easily and has acceptable electric properties for application in microwave and millimeter wave ranges. Within the K_a-band (f= 35 – 38GHz) at room temperature the complex permittivity is equal to $2.07+i\cdot 3.5\cdot 10^{-4}$.

The external dimensions of the resonator were chosen on the base of the analysis of its frequency spectrum and quality factors. As a first step we obtained the dielectric permittivity of a homogeneous Teflon disk (see Fig. 3.17(a)) of d=78mm diameter and height of h=7 mm, which was the base for the ring in Fig. 3.17(b). The spectrum of the disk was investigated experimentally in K_a band using axially homogeneous HE_{n10}-modes or (TM_{n10}) when the azimuthal index was varied from 35 to 38 (see Fig. 3.12). Then on the base of the dispersion equation (see Appendix, Eq. (A.24)) the theoretical spectrum of the homogeneous resonator was obtained, performing the calculation of the mode spectrum for a certain value of ε' (employing test values being close to the values to the real material under test). The experimentally determined spectrum was compared with the calculated one. In the case of a discrepancy an iterative process was started in order to achieve the highest level of coincidence between the simulated and the measured spectra. This fit of the measured spectrum by the calculated one revealed the desired value for the permittivity of Teflon.

The basic expressions for two-layered resonator structure are reviewed in the Appendix B. The modes in the radially two-layered resonator structure are described by solutions of a set of Maxwell's equations with appropriate boundary conditions. As for the disk resonator, a dispersion equations was derived which allow to obtain the spectral and energy characteristics (i.e. eigen frequencies and eigen-Q-factors) of the anisotropic radially two-layered resonator. These characteristics depend of dielectric properties of both resonator layers.

In the first part of the given work an external diameter $2r_2$=78mm was fixed and the internal $2r_1$ was changed by means of mechanical removal of the internal part of the dielectric disc (Fig. 3.17(b)). The internal radius was changed such that the liquid substance gradually came up to the area where the field of WGM is concentrated (this area of electromagnetic field confinement is called "caustic area" (see subsection 3.1.1), for the employed Teflon disk it was equal r_2-r_1≈ 8 mm distant from the dielectric cylinder edge or periphery). The resonance frequency f and the quality factor Q were measured for the resonator without liquid, i.e. with air filled internal layer (f_{air}, Q_{air}) and with liquid in the internal layer (f_{liq}, Q_{liq}). Sufficiently weak coupling of the resonator by image waveguides was established such that the measured f and Q are not affected by the coupling. The coupling strength was controlled by means of a distance variation between resonator and dielectric image waveguide. The optimum orientation of waveguides relatively a dielectric disc was chosen for excitation of axially-homogeneous modes TM_{n10} (or HE_{n10}), because just these modes could be excited most effectively in WGMR with conducting endplates with resonator height $h \approx \lambda$.

The experimental data on frequency shift $\Delta f_{liq\text{-}air}=f_{liq}-f_{air}$ (Fig. 3.18) and quality factor Q_{liq} (Fig. 3.19) as function of the resonator external layer radial thickness r_2 -r_1 (see Fig. 3.17(b)) were obtained for water, ethyl alcohol and benzene. In the same diagram, the calculation results obtained by solving the dispersion equation (Eq. (B.6) in Appendix B) are shown. The results indicate that the results of theoretical calculations coincide very well with the experimentally determined data for a resonator filled with these three liquids possessing completely different ranges of their complex dielectric permittivity values. For the calculation of losses, the metal losses of the endplates were taken into account.

Values of complex permittivity $\varepsilon^* = \varepsilon' + i\varepsilon''$ of liquids under test obtained with our measurements at the actual resonant frequency of 37.5 GHz of the empty resonator were as follows:

Bidistilled water $\varepsilon^* = 16.80 + i\ 27.38$; $\tan\delta = \varepsilon''/\varepsilon' > 1$;

Ethyl alcohol $\varepsilon^* = 3.6 + i\ 1.08$; $\tan\delta < 1$;

Benzine $\varepsilon^* = 1.88 + i\ 0.062$; $\tan\delta << 1$.

The frequency shift data were taken as a measured parameter with the purpose to eliminate inaccuracy of measurements. Because the endplates of the resonator have not ideal form and it possess some roughness on the surface and correspondingly some air gaps, there remains an influence of pressing strength between metal plates and resonator surface on the resonant frequency. The effect of such gaps and roughness is difficult to estimate, particularly if one reassembles the resonator. Therefore, the measurements were carried out without reassembling the resonator each time for frequency shift $\Delta f_{liq\text{-}air}= f_{liq}-f_{air}$ determination has been performed for each given radial thickness r_2-r_1 of the external layer. The values of the quality factor were found to be practically independent on reassembling; therefore values of Q_{liq} were used for the measurement results analysis.

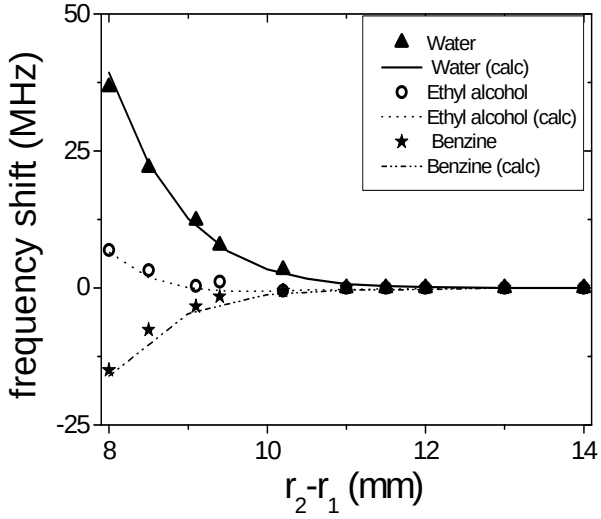

Figure 3.18 Frequency shift $\Delta f_{liq\text{-}air} = f_{liq} - f_{air}$ of WGMR as a function of radial thickness $r_2 - r_1$ of external dielectric ring at a constant external diameter $2r_2$. Experimental results are obtained when the internal ring was filled with one of different liquids: water - triangles, ethyl alcohol - circles, benzine - stars. The lines represent the results of calculations.

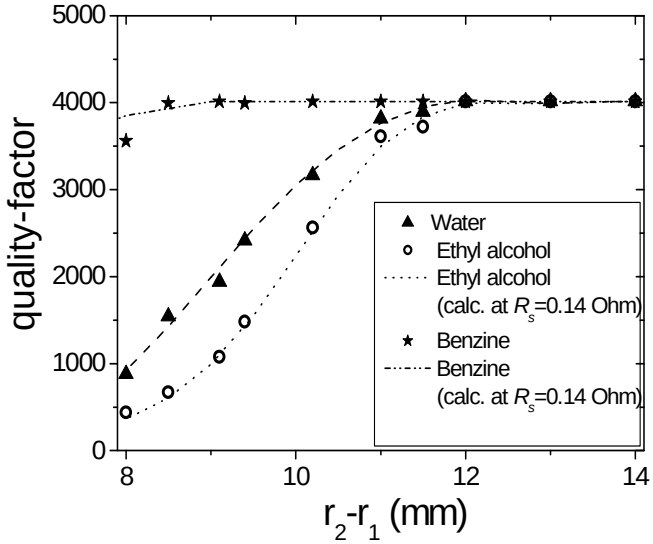

Figure 3.19 Quality factor of QDR as a function of radial thickness $r_2 - r_1$ at a constant external diameter $2r_2$. Experimental points are obtained for water - triangles, ethyl alcohol - circles, benzine – stars. The doted-dashed lines were calculated for these liquids taking into account microwave losses in the conducting endplates.

It is worth to underline a number of "anomalies" obtained found by the experimental investigation. These "anomalies" do not manifest themselves for resonators filled with dielectrics having values $\tan\delta << 1$. They are as follows:

i) A positive sign of a frequency shift $\Delta f_{liq\text{-}air}$ for both lossy liquids, namely, water and ethyl alcohol is observed (see Fig. 3.18); Water possesses higher losses than ethyl alcohol, such that the slope of $\Delta f_{liq\text{-}air}$ curves for water is bigger than for ethyl alcohol.

ii) Q_{liq} of the resonator filled with water is higher than the corresponding value for ethyl alcohol (see Fig. 3.19), in spite that $\tan\delta$ of ethyl alcohol is lower than that of water;

iii) Liquids characterized by small loss tangent values like benzene lead to a decrease of $\Delta f_{liq\text{-}air}$ with increasing inserted volume.

iv) A sign of a frequency shift $\Delta f_{liq\text{-}air}$ for ethyl alcohol changes from negative to positive at variation of r_2-r_1 from large to smaller values as it is shown in Fig. 3.18 (see more details for ethanol in Fig. 3.20 (b)).

These observations indicate that perturbation theory according to Eq. (3.8) does not apply. The reason is that in the case of the radial two layered resonator the field distribution is altered by the permittivity of the liquid.

Within this work there was studied the situation when the Teflon resonator body has a bottom of height l (see insert on Fig. 3.20 (a)). For such resonator geometry the characteristic equation cannot be obtained accurately. In this case the behavior of $\Delta f_{liq\text{-}air}$ becomes more complex because the internal layered structure is more complex. As it is displayed in Fig. 3.20 (a) the sign of the frequency shift changes from negative to positive even more significantly for alcohol than it was the case for the resonator without bottom (l=0). For water the decrease of the slope was also observed in comparison to the case of l=0.

However, all of the mentioned peculiarities can be theoretically described by using Maxwell equations with corresponding boundary conditions and can be explained by means of the evolution of the field distribution of R2L WGMR filled with lossy liquid. Fig. 3.21 shows the calculated field distribution along the radius for water, ethyl alcohol and air (the latter for comparison). One can see that because of lower loss in alcohol, the microwave field is damped more weakly in alcohol than in water. This means that a field penetration depth for alcohol is larger than for water, which causes higher values of Q_{liq} in the case of a water-filled resonator. High values of loss tangent $\tan\delta_{liq}$ and dielectric constant ε'_{liq} cause a screening – "metal" behavior of the frequency shift with a positive sign $\Delta f_{liq\text{-}air}$ for the resonator with ethyl alcohol and water.

Finally, the change of the sign of frequency shift sign (see Fig. 3.20) depending on r_2-r_1 in case of ethyl alcohol shows that a competition of two effects takes place in the resonator with lossy liquid. Namely, the influence of a dielectric liquid leads to the negative sign of the frequency shift (due to increase of electric field energy when the distribution of the electric field is not altered), and the influence of a lossy liquid on the field distribution itself leads to the positive sign of the shift. As the experiments show, the phenomenon of changing a frequency shift is very sensitive to the reference (i.e. without liquid) field distribution and hence to the particular type of resonator, its geometry, the volume of liquid, and also to the dielectric properties of the liquid.

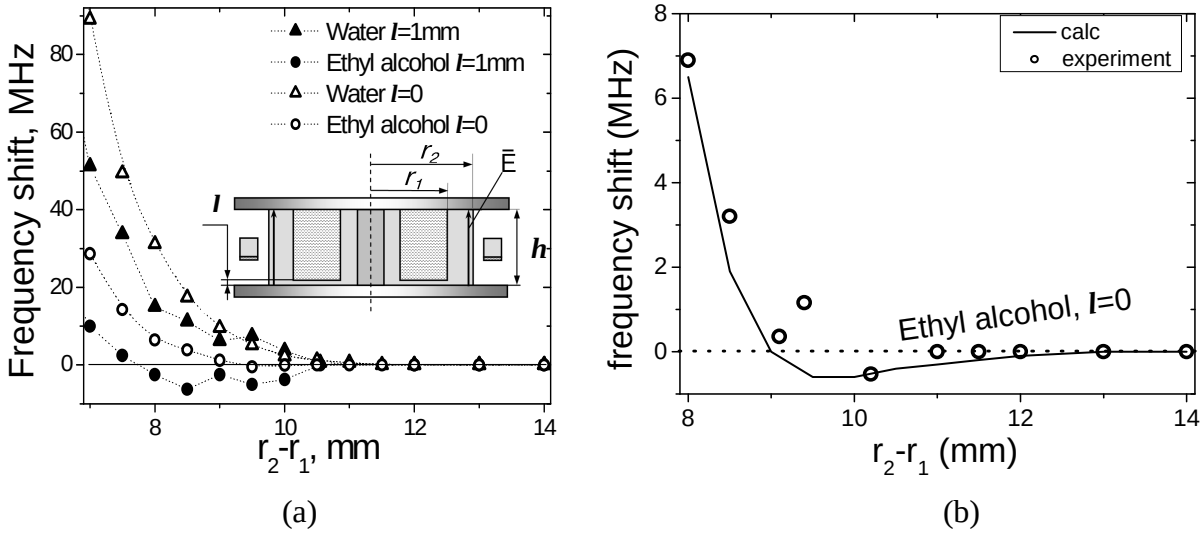

(a) (b)

Figure 3.20 (a) Frequency shift $\Delta f_{liq\text{-}air} = f_{liq} - f_{air}$ of the resonator as a function of radial thickness $r_2 - r_1$ of external dielectric ring of the resonator with internal ring filled with ethyl alcohol, *l* is a thickness of Teflon bottom in the internal layer. Inserted R2L resonator implemented in a form of double ring with bottom of thickness *l* and internal Teflon ring was made to keep metal plates rigidly parallel to each other. The electric field is shown for HE-mode; (b) frequency shift $\Delta f_{liq\text{-}air} = f_{liq} - f_{air}$ as a function of radial thickness of the resonator with ethyl alcohol when *l*=0 (zoomed view).

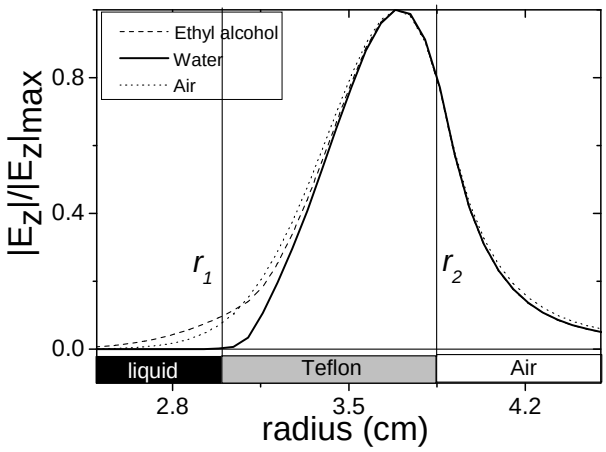

Figure 3.21 Distribution of the normalized *z*-component of the electric field in the resonator along the radius of the dielectric disk (ring), when the resonator is filled with ethyl alcohol, water or air.

It is necessary to note that an analogous change of the frequency shift sign for the same liquid was observed in another type of WGM resonator, namely, in a dielectric disc with a cylindrical capillary filled with water and placed in caustic area of the electromagnetic wave in the resonator [69]. The effect of increasing of *Q*-factor with increase of the loss tangent of liquid was found theoretically also for a hemi-spherical two-layered resonator excited in a lower order mode, however, only at large thickness of the Teflon layer of the resonator [67].

In summary, the electrodynamic properties of radially two-layered quasi-optical dielectric resonators with conducting endplates and lossy liquids (for example, ethyl alcohol and water) have been studied experimentally and theoretically. Whispering gallery modes are

excited in such resonators. The mode energy is concentrated near the inner side of the cylindric surface of the external layer. Liquids with arbitrary values of complex permittivity including liquids with $\tan\delta_{liq} > 1$ represent the internal layer. The obtained results allowed to determine an optimum value of the external ring thickness or thickness of the external layer (at fixed external radius) to be equal to about 8 mm. All further investigation with this type of resonator filled with different liquids was carried out with fixed resonator dimensions.

Chapter 4: Characterization of diluted aqueous solutions with an open WGM resonator technique

In this chapter the studies of the electrodynamic properties of WGM dielectric resonators of the two types described in Chapter 3 are discussed for the case of introduction of different aqueous biochemical liquids in the resonator structure in order to determine the dielectric properties of these liquids. The interaction of electromagnetic waves with water and aqueous materials forms the subject of this work. We can approach this subject with many different objects in view, when water serves as a solvent for small inorganic ions and low-weight organic molecules as well, and it plays a dominant part in determining the structure and functional properties of proteins and other macromolecules.

Aqueous systems have been in the focus of many investigations comprising a variety of experimental methods based on application of dielectric theories, helping to elucidate the "structure of liquid water" and of solutions, both electrolytic and bimolecular, including computer simulation studies of the microdynamics of water and aqueous systems. Much progress has been made recently in the understanding of the dielectric properties of biological systems [84-87]. The understanding of the principles of how biological macromolecules work is a challenging topic in biophysics. Conformational changes and molecular motions are essential to life processes. Dielectric spectroscopy is sensitive to intramolecular conformational variations of proteins in solution [88] as well as to hydration properties of macromolecules [89]. It is also an effective non-invasive method for investigations on a cellular level, for example for monitoring the effect of glucose on the human erythrocyte membrane [90].

Depending on the liquid composition we can describe several types of liquids with a specific behaviour of the dielectric function. In one case, the strength of the electrical polarizability and the molecular relaxation, the latter being determined by the molecular mass and the intermolecular interaction, provides a fingerprint for semipolar liquids such as alcohols. In the other case, long chain hydrocarbons with low real part of permittivity can be differentiated to some extend by their variation of dielectric losses. Finally, the contribution of conducting components such as ions leads to a $1/f$ dependence of the imaginary part of the permittivity. In particular, for biological liquids, which are water based, both the organic and inorganic constituents lead to specific modifications of the frequency dependence of the real and imaginary part of the complex permittivity at microwave frequencies.

Below we discuss the data on selected solutes in water, which were measured by our resonator techniques. Organic polar and non-polar molecules with slow relaxation time or electrolytes dissolved in water cause a reorientation of the intermolecular bonds and result in a change of the frequency dependence of real and imaginary part of permittivity. Therefore, we expect that the developed WGM resonators allow observing changes of frequency and inverse quality factor depending on the dissolved species and on concentration with a good accuracy for small volumes.

4.1 Example of aqueous solutions of non-electrolytes: ethanol-water mixtures

In this chapter we consider the dielectric properties of aqueous solutions of non-electrolytes, particularly of organic liquids and solids, such as alcohols and sugars. Such molecules will usually dissolve extensively in water if they are able to interact in some way with the network of OH…O hydrogen bonds. This implies that some parts of the solute molecule must itself be able to make a hydrogen bond to an H_2O molecule. Polar liquids such as alcohols possess their own static dielectric constants, correlation factors, and characteristic relaxation times. Aqueous solutions often show features which derive directly from the pure polar liquids.

Alcohols are compounds in which a hydroxyl (–OH) group is attached to a carbon atom, or replaces a hydrogen atom in a corresponding alkane molecule. The hydroxyl group is the functional group of alcohols. Their general formula is R–OH, and they are classified as monohydric, dihydric, trihydric, and polyhydric alcohols. The O–H bond is highly polar, because oxygen is highly electronegative. The oxygen carries a partial negative charge (δ–) and the hydrogen carries a partial positive charge (δ+). The polarity of the O–H bond gives rise to an attraction of partially positive hydrogen atoms of other molecules. Due to this, hydrogen bonding requires a lot of energy in the form of heat to overcome these attractive forces, and hence the boiling point of alcohols is higher than for pure organic substances of same molecular size such as the alkanes.

The first examples of water-based liquids being chosen in order to test our measurement systems were water-ethanol mixtures of different concentrations. Ethanol, with sum formula C_2H_5OH, is one of the most simple alcohol molecules and is a semipolar liquid with low real part of permittivity. Dissolving ethanol molecules in water leads to increase of the relaxation time and to a decrease of the dielectric permittivity with respect to water.

For the water dipole to be able to undergo considerable rotation about one of its hydrogen bonds, the breakage of its other bonds is necessary. Unbound molecules, or molecules making only one bond, can rotate without breakage, whilst molecules bonded to three or four neighbors require more than one bond. In “two bonded” molecules reorientation occurs after breaking of one bond. The strong bond which remains will play the dominant role in the principle relaxation process. The faster bond-breaking processes make slower (higher-energy) processes very rare, such that the three and four bonded species do not contribute to any appreciable relaxation, even though they are present in large proportions. The dipole properties of water molecules affect the interaction between water and other molecules that dissolve in water.

Water, methanol, ethanol, and others are hydrogen bonded liquids and completely miscible with each other and each of them exhibits a principal dispersion of Debye or nearly - Debye type in the microwave frequency range. The mechanism of the dispersion is suggested to be rotational diffusion of individual polar molecules or molecule clusters in the liquid under the action of the applied field.

The dielectric study has extensively been done on alcohol-water mixtures [91-95] because these systems exhibit an interesting behavior with emphasis on hydrogen bonding, hydrogen-bonded clusters and cooperative processes for the molecules. Dielectric spectra were obtained with different techniques. To the best of my knowledge, there is a paucity of such data covering a wide frequency range. Using complex nonlinear least squares (CNLS) fitting techniques, the dispersion parameters for water–methanol and water–ethanol mixtures could be determined based on both Debye and Cole–Davidson functions. The dependence of the relaxation time τ on the fraction of water reveals different relaxation mechanisms with various dominant relaxation processes in the different concentration regions.

Pure alcohol molecules are assumed to form chain like clusters in the liquid phase, and dispersion is due to the cooperative processes of entire clusters [96]. In the region of mole fraction of water below 80%, water molecules join the clusters like the alcohol molecules. The smaller size of the water molecules leads to a higher dispersion frequency compared to that of pure alcohol. Pure water molecules are believed to form loosely bonded circular clusters in the liquid phase compared to that of pure water, and each of them contains six molecules. In the region of mole fraction of water above 80%, alcohol molecules take part in the circular clusters like water molecules. The larger size of the alcohol molecules results in a lower dispersion frequency.

Water, methanol, and ethanol display distinct relaxation processes that differ from each other. For instance, two or three such processes in pure liquids could be observed. For their binary mixtures the existence of only a single primary relaxation strongly suggests that these molecules in the liquid phase react to the external field in a strongly cooperative way rather than individually. The Debye function actually results for a system of non-interacting dipoles. In general, two relaxation processes would be expected for binary mixture according to rotational diffusion theory, so it still presents a theoretical challenge [93] to understand how two well separated relaxations in the respective pure liquids fuse into one relaxation process in their binary mixture even when the sizes of the molecules differ substantially, such as in water–alcohol mixtures.

Therefore, the dependencies of ε_{liq}' and ε_{liq}'' on alcohol concentration in water mixture can be calculated by a single Debye function

$$\varepsilon_m = \varepsilon_m' + \mathrm{i}\varepsilon_m'' = \varepsilon_\infty^m + \frac{\varepsilon_s^m - \varepsilon_\infty^m}{1 - \mathrm{i}\omega\tau_m} \tag{4.1}$$

where ε_∞^m ε_s^m are high-frequency and static dielectric constants of mixtures respectively, τ_m is relaxation time of the mixture.

A linear relation between the static dielectric constant ε_s^m and the volume concentration of the solution (C_v) can be derived from the Onsager equation for miscible liquids within some approximation [97]. It means that the value ε_s^m of mixture can be calculated from its pure constituents.

Values ε_s^m and ε_∞^m are connected by means of relation which follows from an expanded theory by Frölich for static permittivity, where an effective dipole orientation factor g_{eff}^{m} is introduced [98],

$$\frac{\left(\varepsilon_s^m - \varepsilon_\infty^m\right)\left(2\varepsilon_s^m + 2\varepsilon_\infty^m\right)}{\varepsilon_s^m(\varepsilon_\infty^m + 2)^2} = \frac{\mathrm{N_a}}{9\varepsilon_0 k_B T} g_{eff}^m \rho_m \left(\frac{X_e\mu_e + X_w\mu_W}{X_e M_e + X_w M_W}\right) \tag{4.2}$$

where X_e and X_w are mole fractions of ethyl alcohol (ethanol) and water respectively, M_e and M_w are mole masses of mixture components, μ_e and μ_w are the dipole moments of ethanol and water (μ_e = 1.68, μ_w = 1.86 D), and ρ_m the density of the mixture.

Data on ρ_m of ethanol water mixtures are presented in a broad temperature interval in [94]. In the same work, the concentration dependence of g_{eff}^{m} have been obtained. The values of g_{eff}^{m} correspond to Kirkwood's orientation correlation factor g_w and g_e for each component of the mixture.

The temperature dependence of the relaxation time is presented by Eyring equation [6] (see also Eq. (1.48)).

$$\tau = \frac{h}{k_B T}\exp\left(\frac{\Delta G_m}{RT}\right) \tag{4.3}$$

where h is the Plank constant, T is the absolute temperature, R is the gas constant and ΔG given by (see 1st chapter)

$$\Delta \mathrm{G}_m = X_e \Delta G_e + (1 - X_e)\Delta G_w \tag{4.4}$$

where ΔG_e and ΔG_w are the free activation energies for ethanol and water, respectively. The relaxation time τ_m for the mixture is then given by

$$\tau_m = \frac{h}{k_B T}\exp\left(\frac{\Delta G_m}{RT}\right) = \tau_e^{X_e} \cdot \tau_w^{(1-X_e)} \tag{4.5}$$

where τ_e and τ_w are relaxation times of the mixture components.

The obtained values of ρ_m, $g_m = g_{eff}^m$; ε_0^m, ε_∞^m and τ_m depending on the volume concentration of ethanol in water are presented in Table 4.1. Values τ_e = 184 ps and τ_w = 9.38 ps have been taken from the literature [19, 94]. All data are presented for the case of room temperature (20°C).

On the base of the Eqs. (4.1)-(4.5) and the data summarized in Table 4.1 the calculations were carried out with Mathcad 2001 Professional.

Table 4.1 Values of ρ_m, $g = g_{\text{eff}}^{m}$, ε_0^m, ε_∞^m and τ_m depending on ethyl alcohol concentration in water at room temperature (20°C).

C_e	X_e	ρ_m [94], g/cm^3	g_m [94]	ε_s^m [94], [97]	ε_∞^m [94]	τ^m [93],[94]
0	0	0.998	1.180	80.124	3.823	9.38
0.1	0.033	0.990	1.177	75.353	3.833	10.36
0.2	0.072	0.978	1.175	70.301	3.842	11.61
0.3	0.117	0.964	1.171	64.982	3.857	13.29
0.4	0.171	0.948	1.163	59.428	3.883	15.6
0.5	0.236	0.928	1.142	53.683	3.942	18.95
0.6	0.317	0.906	1.085	47.813	4.103	24.1
0.7	0.419	0.881	1.069	41.905	4.167	32.67
0.8	0.553	0.853	1.139	36.067	4.021	48.65
0.9	0.736	0.823	1.288	30.432	3.754	83.8
1	1	0.790	1.611	25.153	3.322	184

4.1.1 Radially two-layered WGM Teflon resonator with ethanol-water solutions

After preliminary investigation of the radially two-layered resonator with Teflon outer layer described in Chapter 3, measurements of the concentration dependences of Δf_{liq} and Q_{liq} were performed for different concentrations C_e of ethanol in bidistilled water. The thickness of the external Teflon ring was fixed to $r_2 - r_1 = 8$ mm. Such thickness allows to achieve a reasonable sensitivity of frequency shift Δf_{liq} against the variation of alcohol concentration C_e. There is a stronger dependence of Q_{liq} on concentration with larger thickness $r_2 - r_1$ (see Fig. 3.19), however, at the same time the dependence of Δf_{liq} on C_e will be weakened. Evidently, the selected thickness $r_2 - r_1$ is the optimum from point of view of achieving maximum accuracy of measuring ε' and ε''. The measurement results are shown in Fig. 4.1.

The experiments are important for establishing the dispersion of substance properties in the microwave and millimeter wavelength ranges. In this connection it is relevant to find an opportunity to measure the concentration dependence of the complex permittivity of solutions excluding a calibration procedure.

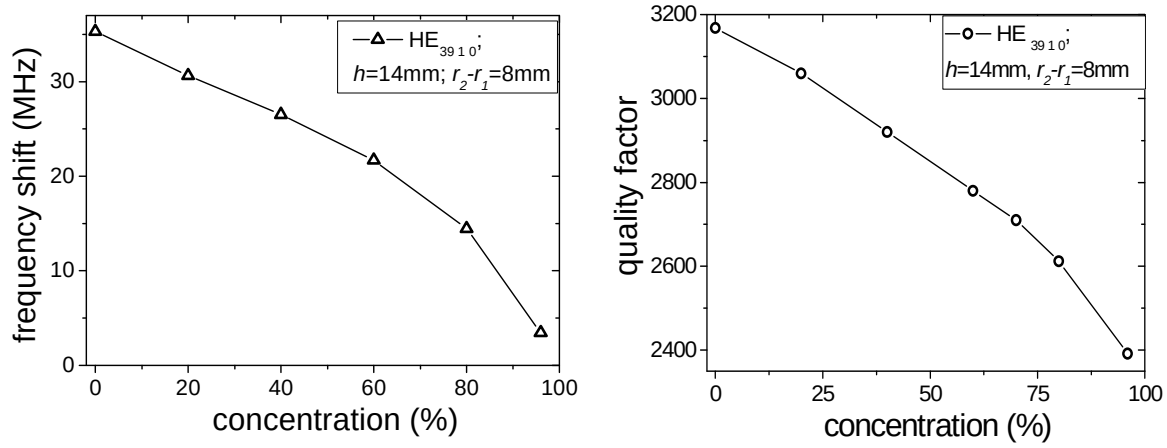

(a) (b)

Figure 4.1 (a) Frequency shift and (b) quality factor of a R2L WGM resonator with a binary water-ethanol mixture as functions of ethanol volume concentration, mode $HE_{39\,1\,0}$ (TM), h = 14mm, r_2 – r_1 = 8 mm, f_r=37.5 GHz – resonant frequency of empty resonator.

Using a special program composed for computer calculations of R2L type WGM resonators, real (ε'_{liq}) and imaginary (ε''_{liq}) parts of complex permittivity of the mixture were determined by means of fitting the calculated values of the experimentally determined values of Δf_{liq} and Q_{liq}. These results are presented in Fig. 4.2. In the same place, the solid lines show results of ε'_{liq} and ε''_{liq} calculation for the mixture, obtained independently on above stated results on the base of Debye's model for complex permittivity of binary mixtures ($\varepsilon'_{liq} = \varepsilon'_{mix}$ and $\varepsilon''_{liq} = \varepsilon''_{mix}$) and parameters of the Debye equation listed in the Table 4.1.

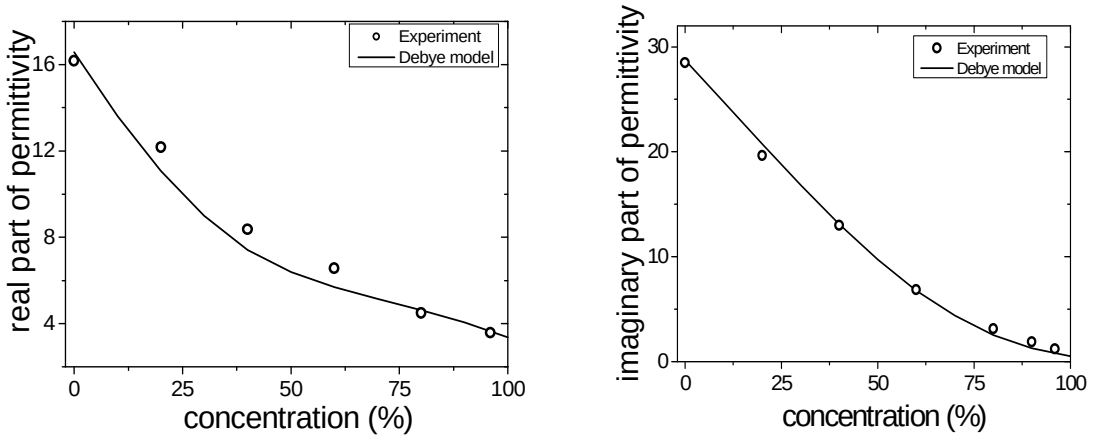

(a) (b)

Figure 4.2 (a) Real and (b) imaginary parts of permittivity of binary water-ethanol mixture as functions of ethanol volume concentration. The solid lines are a result of calculation using Debye's formula (Eq. 4.1)

The very good agreement between theoretical calculations and experimental results indicate the validity of the mentioned model for description of binary mixture properties and demonstrates the usefulness of a calibration free measurement approach. The obtained field components allow to calculate the coefficients $k_1=k_{liq}$, $k_2=k_{ring}$, which are coefficients of inclusion of liquid (air) and dielectric material of the ring, as well as $A_s = 1/G$, which is called CEP inclusion coefficient which determines the loss contribution of CEP metal to the quality factor of the resonator (see Chapter 3, Eq. (3.1)). Thus one can determine $\tan\delta_{liq}$ from the measured values of Q_{liq}. In the given work the coefficient A_S was calculated only for a homogeneous disk or large thickness of $r_2 - r_1$ (see for example [62]). This time it was determined in the whole interval of $r_2 - r_1$ variation using the known properties of water and by comparison to the experimental dependence of Q_{liq} on $r_2 - r_1$ and calculated dependence of Q_{liq} for the resonator with perfect CEP. In future, the coefficient A_S will be calculated through field components of the corresponding mode of the resonator intended to be used as measuring cell.

4.1.2 Sapphire resonator with a small droplet of a water-ethanol mixture.

In the previous chapter the approach, which was developed in order to investigate various substances dissolved in water in the shape of a droplet of volume down to 90 picoliters, was described. Fig. 4.3 demonstrates the functioning of the device. The water droplet of a very small amount ($V \approx 2$ nl) leads to a significant reduction of quality factor and shift of resonance frequency. This can be utilized as a highly sensitive detector for the identification and monitoring of different aqueous solutions in small volumes. Droplets were prepared by a microprocessor controlled microinjection pipette and spotted onto the most sensitive position on the WGM resonator surface according to the calculated field distribution in the resonator (see Chapter 3). Our dielectric liquid-sensor operates by monitoring Q-factor and resonant frequency changes induced by the droplet at frequency around 35 GHz. The signal transmitted S_{21} from the input to the output waveguide through the resonator depicted in Fig. 4.3 (absolute value of S_{21}) around the resonance frequency was measured with a

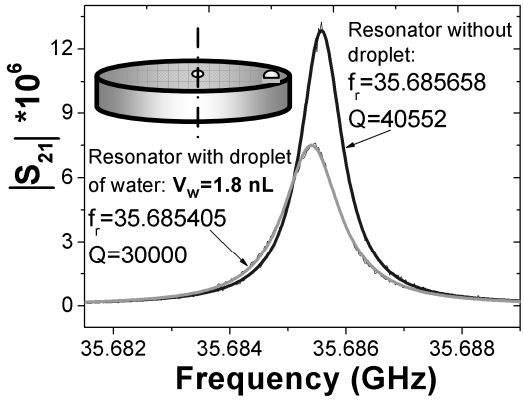

Figure 4.3 Measured resonance curve before and after the droplet spotting. The experimental data are fitted by Lorentzian curves.

Hewlett-Packard 8722C Vector Network Analyser. The HP 8722C was interfaced with a computer using HTBasic 9.5 and a GPIB controller to measure and store the data. Measurements were always performed approximately five times for the same droplet volume of each liquid under test.

The resonator assembly was composed of the sapphire resonator, resonator holder, coupling elements and a Peltier cooler based system for temperature stabilizing as shown in the photograph (Fig. 4.4). The resonator assembly was attached to a *xy* scanning table through a metal holding plate as it is shown in Fig. 4.4(a). A computer controlled spotting positioning system employs the scanning *xy* table for precise positioning of the resonator system in front of the nozzle tip of a fine glass capillary connected to an autodrop pipette system. The AD-K-501 pipette is based on a piezo-driven inkjet printing technology, the smallest droplet which is emitted from the nozzle tip and detected by our resonator system has a volume of about 90 picoliters. The spotting system is also equipped with a miniature camera setting for controlling the droplet shape. For the purpose of stabilizing the droplet on the resonator surface and avoiding rapid evaporation of the liquid from the surface as well as for stabilization of the dielectric resonator characteristics, a temperature controlling system was utilized to keep the temperature of the resonator at 18±0.1°C, which was slightly lower than the temperature of 23°C in the laboratory.

As a first step, volume dependencies of resonant parameters of our droplet-detector were measured by spotting solutions of several diluted concentrations of ethanol in water (Fig. 4.5). The limiting concentration was around 50% of ethanol, where the speed of the evaporation process is still comparable with the speed of almost "instantaneous" measurements of the

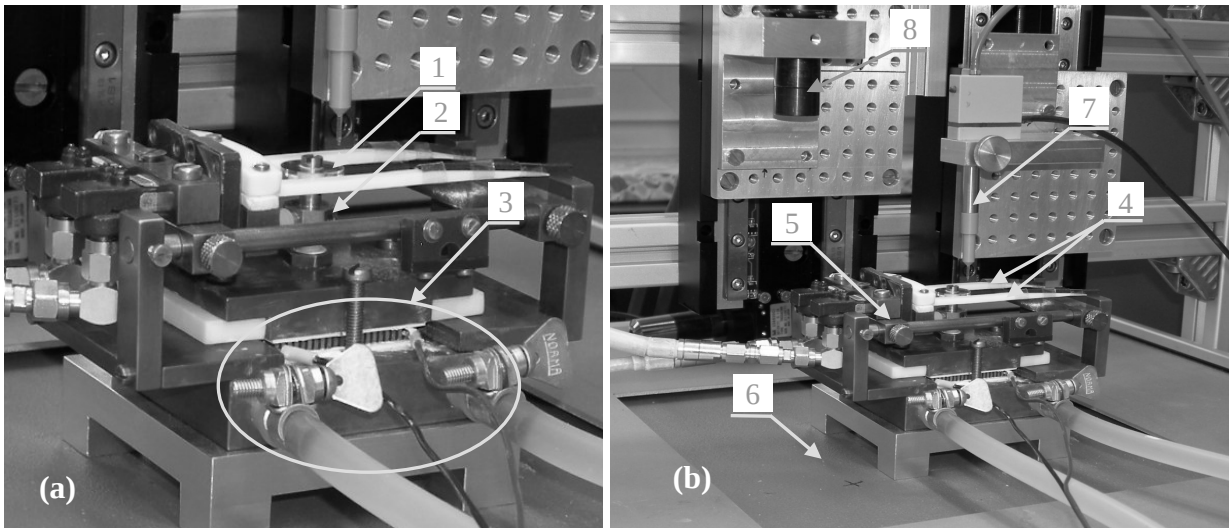

Figure 4.4 (a) Photograph of the experimental setup in a close view. (b) A view of the resonator including spotting-positioning system. The main elements of the experimental setup indicated by arrows are: 1- resonator; 2 – holder for resonator and temperature platinum sensor; 3 – elements of temperature stabilizing system including a Peltier element and plate with circulating cooling liquid providing an effective extraction of heat; 4 – dielectric waveguides; 5 – mobile carriage utilized for positioning of the coupling elements, serving as their holder simultaneously; 6 – xy scanning table; 7 – *z*-axis moving automated microinjection pipette; 8 – miniature CCD camera.

changes in the resonant curve. The results indicate that the resonator allows us to distinguish between different concentrations of ethanol in such small volumes. The obtained dependencies tend to be linear on droplet volume for this range, which is advantageous for the calibration of our system [99].

Now, one can compare the measured changes of resonant frequency and inverse quality factor with the real and imaginary parts of the complex dielectric permittivity $\varepsilon^*(\omega)$ of diluted aqueous solutions of ethanol, which can be well described by a Debye-type relaxation spectral function Eq. (4.1). Fig. 4.6 shows the data calculated for the real and imaginary parts of the complex permittivity as a function of concentration using the parameters of the Debye function displayed for water-ethanol mixtures in tabular format (Table 4.1). The corresponding values for 35 GHz are represented in the form of relative change (in %) of dielectric permittivity with respect to the permittivity of bidistilled water. The negative sign of the percentage means that adding ethanol to water decreases both real and imaginary parts of $\varepsilon^*(\omega)$. These results can be compared directly with the droplet data depicted in Fig. 4.5. The open symbols connected by the dashed lines in Fig. 4.6 show the percentage of change of resonant frequency with increase of alcohol concentration (change of slopes of the frequency shift-vs-volume curves in Fig. 4.5 (a)) and the percentage of change of the inverse quality factor (slopes from Fig. 4.5 (b)). According to perturbation theory (Eqs. (3.8) and (3.9), chapter 3), these curves directly predict the relative changes of ε' and ε'', respectively. There is a qualitative agreement between the droplets results and theoretical predictions, the difference may be due to a smaller than nominal concentration of alcohol in the droplets due to evaporation (in fact, "squeezing" of the concentration axis for the droplet data in Fig. 4.6 would cause a better agreement with the calculated values).

It is interesting to compare the ratio of slopes for frequency shift and change of inverse quality factor, which is proportional to the loss tangent (see Eq. (3.9)). According to the Debye model (Eq. (4.1)), the loss tangent can be written as:

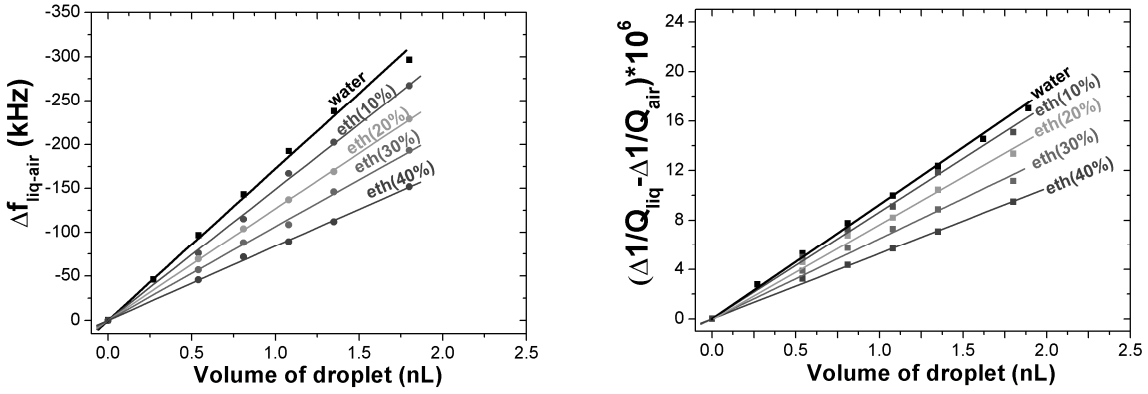

(a) (b)

Figure 4.5 Measured droplet induced changes of (a) resonant frequency $\Delta f_{liq-air}$ and (b) inverse quality factor $1/Q_{liq}$-$1/Q_{air}$ as functions of volume of dilute aqueous solutions of ethanol (T=18°C).

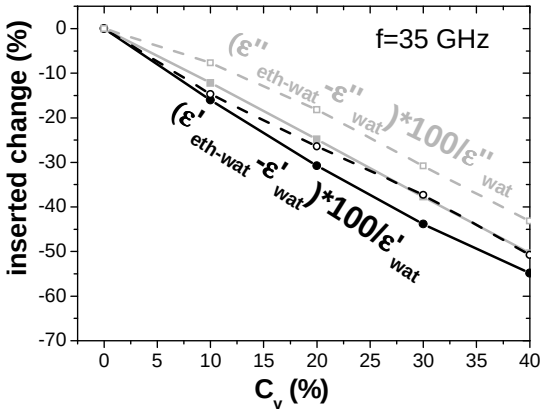

Figure 4.6 Calculated dielectric permittivity (real ε' and imaginary ε'' parts) as a function of concentration (C_v) of ethanol in bidistilled water (T=20°C) (full symbols connected by solid lines) and experimental data taken from droplet measurements (open symbols connected by dashed lines).

$$\tan\delta_m = \frac{\varepsilon_m''}{\varepsilon_m'} = \left[\frac{\varepsilon_\infty^m}{\varepsilon_m''} + \frac{1}{\omega\tau_m}\right]^{-1} \approx \omega\tau_m \quad (\varepsilon_\infty^m << \varepsilon_m'') \tag{4.6}$$

Taking the ε_∞ data shown in Table 4.1 and the permittivity reference data shown in Fig. 4.2, the approximation $\tan\delta = \omega\tau$ in Eq. (4.6) holds true ($1/\omega\tau \approx 0.46$ for water at 35 GHz) for the measured concentration values below about 40 %. Due to the linear dependences on volume shown in Fig. 4.5 our method allows the determination of the relaxation time as a function of concentration without exact knowledge of the droplet volume. In turn, out method allows a high precision determination of the alcohol concentration of nanolitre droplets without exact knowledge of their volume. This is an extremely important finding, indicating the analytical power of our method.

Fig. 4.7 shows the re1axation time determined by

$$\tau = \frac{1}{2\pi}\frac{\Delta(1/Q)}{\Delta f} \tag{4.7}$$

employing the linear slope of the $\Delta(1/Q)$ and Δf data on the droplets for the different concentration values shown in Fig. 4.5. The data for albumin and glucose will be discussed later. The full line is the theoretical curve for alcohol water mixture according to Eq. (4.5), roughly corresponding to the reference data from Table 4.1.

One should note that this methods gives the correct order of magnitude for pure water (concentration = 0), which is an indication for the validity of the perturbation approach. At low concentration values (below 10%), the curve gives the correct slope. For higher values, the experimental slope is significantly lower. This may be partially due to neglecting of the $\varepsilon_\infty / \varepsilon''$ term in Eq. (4.6), but also due to a lower-than-nominal alcohol concentration in the droplets, as discussed in conjunction with Fig. 4.6. However, a non-monotonous dependence of the relaxation time on concentration in alcohol-water mixtures was also reported in the

literature [100]. As it will be discussed in Chapter 5, loss tangent measurements represent a powerful tool for concentration measurements of extremely diluted aqueous solutions.

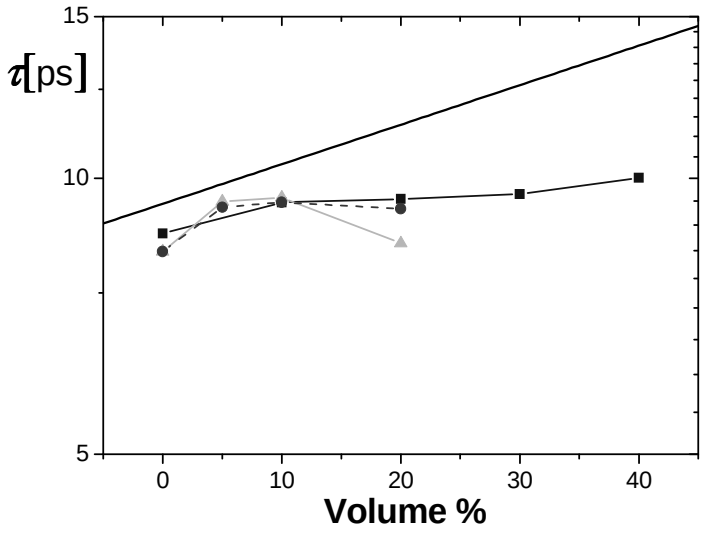

Figure 4.7 Relaxation time as a function of volume percent concentration for ethanol (squares), glucose (triangles) and albumin (circles) dissolved in bidistilled water, determined from the measurements on nanolitre droplets.

4.2 Example of aqueous electrolyte solutions: sodium chloride dissolved in water

The results on the dielectric properties of aqueous electrolytic solutions are of considerable importance because of the particular significance of electrolytes in diverse chemical and biological processes, and their influence on the dielectric properties of cells and biological tissue. Besides this, interest in electromagnetic wave interaction with saline solutions also springs from a variety of applications. The most important electrolytes are NaCl and KCl water solutions, which particular control the function of biological membranes at the cellular level. Contrary to the major role that aqueous solutions of salts do play in nature, science, and chemical engineering, their dielectric properties are insufficiently known. Presently, a generally valid theory describing the dielectric properties of solutions of charged solutes is not available. In recent years computer simulations have been used to study principally the structure and the dynamics of ionic solutions [101-104]. There exist a great interest in the dynamics of hydrogen bond fluctuations and collective dipole moment-current correlation functions. However, more detailed dynamical aspects such as effects of ion concentration on ion-water pair dynamics, frequency dependent conductivity, orientational relaxation of water molecules, and coupling of translational motion of ions in concentrated electrolyte solutions have not been investigated before. One reason for this are the long simulation runs for aqueous solutions based on real water models.

In many cases, the complex dielectric constant of NaCl-water solution as a function of frequency can be adequately represented by the Debye equation of the following form [105]

$$\varepsilon_S^*(\omega) = \varepsilon_\infty^w + \frac{\varepsilon_0^S - \varepsilon_\infty^w}{1 - i \cdot \omega\tau_S} + i\frac{\sigma}{\varepsilon_0 \omega} \quad , \tag{4.8}$$

where ε_0=8.854·10^{-12} F/m is the permittivity of vacuum; ε_∞^w is the high frequency limit of ε_w^* known to be independent on salinity [105] and equal to one of pure (distilled) water; ε_0^S, τ_S, σ are static dielectric constant, relaxation time and ionic conductivity of the solution, respectively.

This equation is similar to the Debye model for distilled water with the addition of the effect of conductivity on the dielectric constant. By many authors solutions with salinities up to 3.5% weight percent were measured and analyzed in order to obtain the complex permittivity of aqueous NaCl solutions as a function of frequency (20 MHz $\leq f <$ 40 GHz) and temperature [95,105-108].

The experimental results can be expressed in terms of salinity of water and temperature by the following equations

$$\varepsilon_0^S = \varepsilon_0^w(T) \cdot A(T,S); \tag{4.9}$$

$$\tau_S = \tau_w(T) \cdot B(T,S); \tag{4.10}$$

$$\sigma = \sigma_{T=25°C}(S) \cdot e^{-\varphi(\Delta T,S)}, \tag{4.11}$$

where the salinity S is expressed in parts per thousand (ppt) on a weight basis; $A(T,S)$, $B(T,S)$ and $\varphi(T,S)$ are empirical functions. All the models described in the literature evaluate the functional dependence of the terms in Eq. (4.8) on the salinity and temperature by fitting polynomial, rational or exponential functions to the experimental data. The parameters were determined from experimental data to predict the variation of all the terms in Eq. (4.8) with temperature and salinity. The highest concentration considered in these studies corresponds to the salinity of sea water. Dielectric reference data of strongly conducting solutions (higher concentrations of salt) are just scarcely available. A high conductivity impedes dielectric measurements by imposing a small resistance on any suitable specimen cell and also by potential space charge polarization effects at the liquid-electrode interface.

By analyzing all listed above models, convenient equations being valid for a wide range of salinities and temperatures on the base of polynomials were constructed by [105] and [106].

The temperature dependence of the static dielectric permittivity and relaxation time of pure water are given by,

$$\varepsilon_0^w(T) = 87.74 - 4.0008 \cdot 10^{-1} \cdot T + 9.398 \cdot 10^{-4} \cdot T^2 + 1.41 \cdot 10^{-6} \cdot T^3$$

$$\tau_w(T) = \frac{1}{2\pi} \cdot (1.1109 \cdot 10^{-10} - 3.824 \cdot 10^{-12} \cdot T + 6.938 \cdot 10^{-14} \cdot T^2 - 5.096 \cdot 10^{-16} \cdot T^3) .$$

The parameters $A(T,S)$ and $B(T,S)$ in Eqs. (4.9) and (4.10) by:

$$A(S)=1-0.2551\cdot N(S)+5.151\cdot 10^{-2}\cdot N(S)^2-6.889\cdot 10^{-3}\cdot N(S)^3;$$

$$B(T,S)=0.1463\cdot 10^{-2}\cdot T\cdot N(S)+1-0.04896\cdot N(S)-0.02967\cdot N(S)^2+5.644\cdot 10^{-3}\cdot N(S)^3$$

where N is the normality of the solution. The relationship between the normality and salinity is

$$N= S\cdot[1.707\cdot 10^{-2}+1.205\cdot 10^{-5}\cdot S+4.058\cdot 10^{-9}\cdot S^2].$$

The other parameters are

$$\Delta T=25-T;$$

$$\varphi=2.033\cdot 10^{-2}+1.266\cdot 10^{-4}\cdot\Delta T+2.464\cdot 10^{-6}\cdot\Delta T^2 - S\cdot[1.849\cdot 10^{-5}-2.551\cdot 10^{-7}\cdot\Delta T+2.551\cdot 10^{-8}* *\Delta T^2].$$

The ionic conductivity of salty water may be fitted in a different way for dilute aqueous NaCl solutions and for concentrated NaCl solutions:

- For the case of $0 \le S \le 40$:

$$\sigma_{T=25^\circ C}(S)=S\cdot[0.182521-1.46192\cdot 10^{-3}\cdot S+2.09324\cdot 10^{-5}\cdot S^2-1.28205\cdot 10^{-7}\cdot S^3]$$

- For the case of $40 < S \le 260$ it was necessary to derive new expressions for the ionic conductivity of concentrated NaCl solutions:

$$\sigma=\sigma_{T=25^\circ C}(N)\cdot[1.000-1.962\cdot 10^{-2}\cdot\Delta T+8.08\cdot 10^{-5}\cdot\Delta T^2-\Delta T\cdot N(S)\{3.02\cdot 10^{-5}+3.922\cdot 10^{-5}\cdot\Delta T +$$

$$+N\cdot(1.721\cdot 10^{-5}-6.584\cdot 10^{-6}\cdot\Delta T)\}],$$

where $\sigma_{T=25^\circ C}(N)=N\cdot[10.394-2.3776\cdot N+0.68258\cdot N^2-0.13538\cdot N^3+1.0086\cdot 10^{-2}\cdot N^4]$.

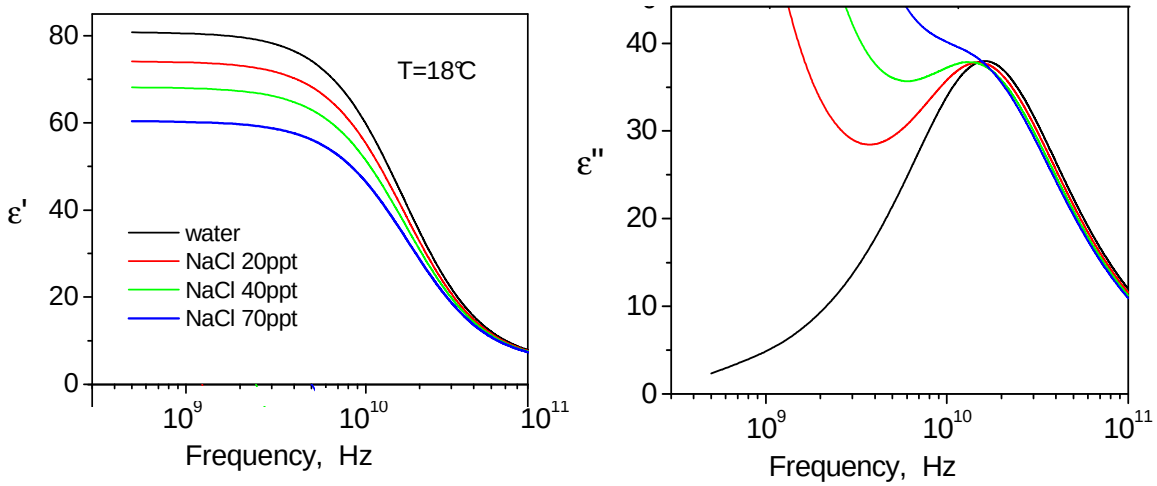

(a) (b)

Figure 4.8 (a) Real and (b) imaginary parts of permittivity of sodium chloride- water solution as functions of frequency calculated by the empirical formulas.

ε_∞^w was taken equal to 4.9 because it leads to a slightly better fit to published data at high frequencies. This frequency limit is independent on salinity and equal to that of pure (bidistilled water).

The frequency dependence of the complex permittivity calculated by the empirical equations was programmed with Mathcad 2001 Professional. The results for a temperature of 18°C are shown in Fig. 4.8, being in very good agreement with experimental data.

Measurements on droplets of NaCl-water solutions

The droplet-detection technique operating at 35 GHz was applied. At this frequency the influence of ionic conduction on the imaginary part of permittivity is not anymore strong in comparison to lower frequencies (see Fig. 4.8). In order to investigate the sensitivity for sodium chloride-water solution, we employed a certain salinity of 70 ppt. The measured linear volume dependencies shown in Fig. 4.9 allow to clearly distinguish this solution from the reference liquid (water). Like for ethanol solutions, in Fig. 4.10 the changes (with respect to water) of complex permittivity for diluted aqueous solutions of sodium chloride of different concentrations C_v, calculated using Eq. (4.8) for electrolytic solutions are shown. The corresponding data from the droplet measurements for the 70 ppt solution are 17% change for the change of frequency shift (corresponding to change of ε') and 7% for the change of inverse Q shift (corresponding to change of ε''), in quite good agreement with the data shown in Fig. 4.8.

The results demonstrate that the change in ε' corresponding to the frequency shift is more sensitive to increasing salinity than the alteration of ε'' with a corresponding smaller change of the inverse Q-factor. The selected NaCl concentration, which is about seven times higher than in a physiological solution, reveals a small effect on measured parameters. This result gives an advantage for the observation of biological liquids, since the effect of diluted biomolecules may otherwise be masked by the ions.

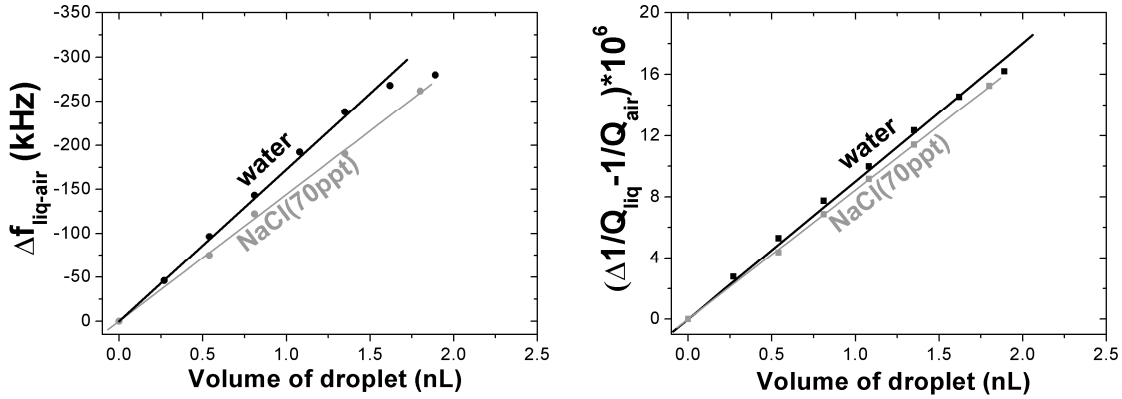

(a) (b)

Figure 4.9 Measured droplet induced changes of (a) resonant frequency $\Delta f_{liq-air}$ and (b) inverse quality factor $1/Q_{liq}$-$1/Q_{air}$ as functions of volume of bidistilled water and aqueous solution of NaCl for a salinity of 70 ppt (T=18°C).

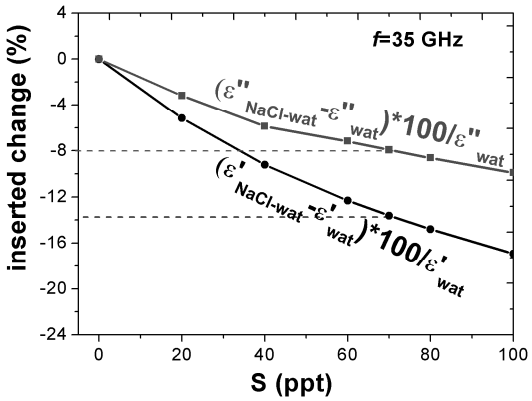

Figure 4.10 Calculated dielectric permittivity (real ε' and imaginary ε'' parts) as a function of salinity (S) of NaCl in bidistilled water (T=18°C).

4.3 Aqueous solutions of albumin and glucose

The dielectric study of biological complex molecules like proteins and carbohydrates dissolved in water is important, since these are essential parts of the living organism and participate in every process within the cells. The results can provide new and unique knowledge and understanding of molecular processes contributing both to the polarization and the conduction of biomolecular solutions; they can be interpreted in terms of the protein molecular structure in its water environment and also in terms of the hydration of a protein solution. In general, dielectric relaxation spectroscopy of proteins allows studying the structural properties of proteins in various environmental conditions [109]. The static dielectric constant of the solution yields the solute protein molecule dipole moment, which can be related to its structure. The dielectric constant in the microwave band, to which there is little contribution from orientation polarization of the protein molecule, can be related to the extent of “binding” of water by the protein. Some information may be extracted about the relaxation of the bound water, which can be discerned at frequencies between that of the protein molecule and that of the free water. But this process can be attributed to relaxation of individual parts of the protein molecule.

From practical point of view, dielectric methods are complementary to more traditional approaches and might provide new insights into the structural and electrical differences between normal and transformed cells (biological objects). The analysis of these substances has been of ever growing importance because of the possibility of simple diagnosis of diseases by measuring dielectric properties.

As an example approaching biological liquids, we have started with the investigation of diluted albumin and glucose. In magnitude relation albumin is mostly represented among other proteins and was one of the first proteins to be studied in dielectric spectroscopy experiments [110]. On the other hand, the glucose concentration in blood is of diagnostic relevance in medicine. Glucose serves as a main energy source, used to maintain the structural and functional properties of the cells. The ability of carbohydrate to substitute water in the

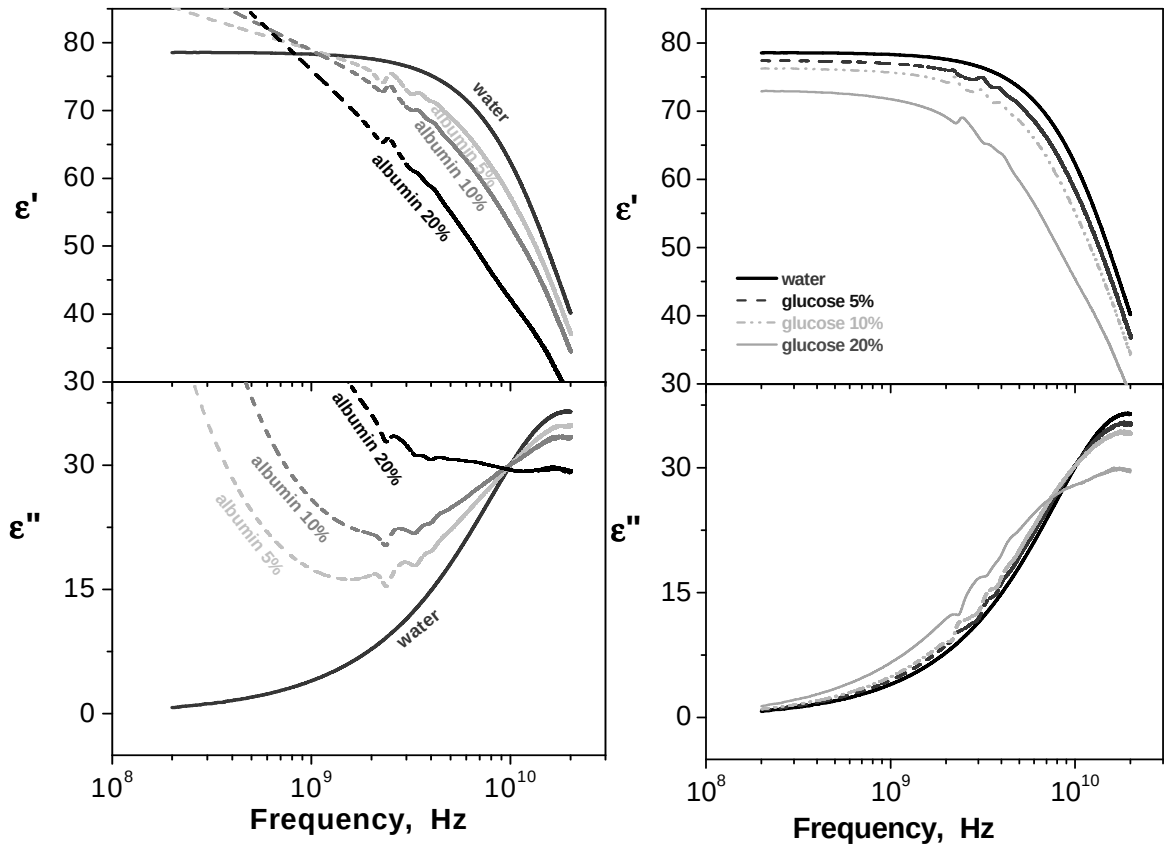

Figure 4.11 Measured complex dielectric spectra for (a) lactalbumin-water and (b) glucose-water at 25°C at different mass fractions.

hydrogen network is essential for their role in biomolecular stabilization and protection. Microwave results on various saccharides were reported in the literature [111,112].

In order to define the character of the dielectric function aqueous solutions of glucose and lactalbumin we measured their complex dielectric permittivity in a wide frequency range from 45 MHz to 20 GHz for 3 particular weight concentrations 5%, 10% and 20% of each solute using the standard open-ended coaxial probe technique, which is very convenient for liquids. As described in chapter 2, with this technique dielectric spectra can be obtained as a continuous function of frequency.

The spectra obtained for albumin (Fig. 4.11 (a)) displays that apart from an increase of relaxation time and decrease of static dielectric permittivity with increase of concentration of macromolecules in the solutions, the dielectric properties of liquids are also influenced by the presence of dissolved ionic residuals, which contribute to a the $1/f$ behavior of the imaginary part of ε* resulting from the conductivity.

In contrast, glucose (Fig. 4.11 (b)) is a complex organic molecular which increases and slightly broadens the relaxation time distribution in a similar manner as alcohols. In addition, the static dielectric constant decreases with increasing concentration.

Despite the coaxial probe technique shows us a tendency of the dielectric behavior in a wide range of frequencies; it does not exhibit a very good accuracy. In particular, the increase of the real part of permittivity at low frequency for the albumin solutions of high conductivity is an artifact due to imperfections of the calibration procedure. Furthermore, it requires respectively larger volumes of a few ml which are not always available for any liquid substance of interest. Therefore, our investigations based on dielectric resonator methods were continued.

4.3.1 Radially two-layered WGM sapphire resonator with aqueous glucose and albumin solutions

For the determination of electrophysical parameters of the "expensive" biochemical liquids there was applied a new modification of the radially two layered resonator. Earlier it was shown that the Teflon ring sandwiched between conducting endplates (CEP) can be used for complex permittivity measurement of lossy liquids [113]. It is worth to note that the accuracy of lossy liquids (such as water) measurement by means of a Teflon resonator is insufficient. Evidently, the accuracy will increase if instead of Teflon another microwave material with the permittivity being of the same order as the permittivity of water at the given operating frequency of 37 GHz can be utilized for the dielectric ring. Therefore, a new resonator composed of a sapphire ring with complex permittivity being noticeably higher than the permittivity of Teflon. The complex permittivity of sapphire is a tensor, the components of this tensor in parallel and perpendicular directions of the crystal optical axis are equal to

$$\varepsilon_{\perp 1} = \varepsilon'_{\perp 1}\,(1+i\cdot\tan\delta_{\perp 1})=9.4\,(1+\,i\cdot 2.5\cdot 10^{-5}) \text{ and } \varepsilon_{\|1} = \varepsilon'_{\|1}\,(1+i\cdot\tan\delta_{\|1})=11.59\cdot(1+\,i\cdot 2.5\cdot 10^{-5}).$$

Another advantage of sapphire is the decrease of the dimensions of the resonator with a corresponding decrease of the internal liquid cavity volume. The resonator was operated in the $HE_{12\ 2\ 0}$ mode excited in the traveling wave regime by means of two dielectrics waveguides using distributed coupling at 38.2 GHz, which supposes two field antinodes along the radius (see Fig. 3.3 (b) case when s=2), in order to decrease additionally the radius of the internal caustic and correspondingly the radius of the internal liquid layer. The external radius of the resonator was r_2 =7.25 mm, and the axial dimension was equal h =2.51 mm (Fig. 4.12(a)). The photograph of this measurement setup and a schematic drawing are shown on Fig. 4.12 (b,c).

The experimental and numerical study of the mode spectrum was performed in analogy with the case of Teflon ring. In order to optimize the volume of the internal liquid layer, the dependencies of frequency shift and quality factor on radial thickness $r_2 - r_1$ were obtained in a way described in Chapter 3 and are presented in Fig. 4.13. The results of the numerical study are presented as solid and dashed lines for measurements with water and ethyl alcohol filling, accordingly. Experimental results are shown by symbols (○) and (Δ) for measurements with water and ethyl alcohol filling. The surface resistance of copper CEP was equal to R_S =0.065 Ohm.

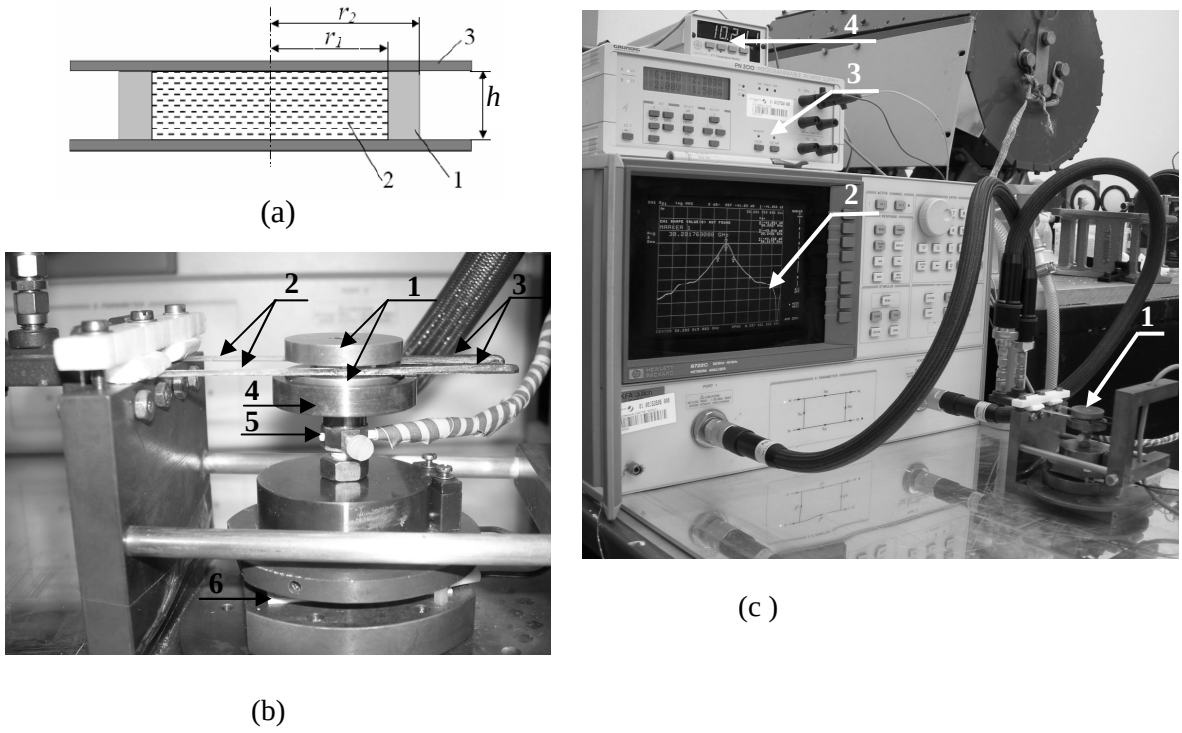

Figure 4.12 (a) Scheme of the resonator structure: 1 – sapphire ring, 2 – liquid, and 3 – conducting endplates; (b) Resonator section in a close view: 1 – metal conducting endplates (sapphire resonator is hidden behind these plates, because it is significantly smaller), 2 – dielectric waveguides, 3 – matched loads, 4 – resonator holder, 5 – temperature sensor; 6 – Peltier element; (c) Photograph of the experimental setup: 1 – resonator section, 2 – Network analyzer, 3 – EPU, 4 – Temperature monitor.

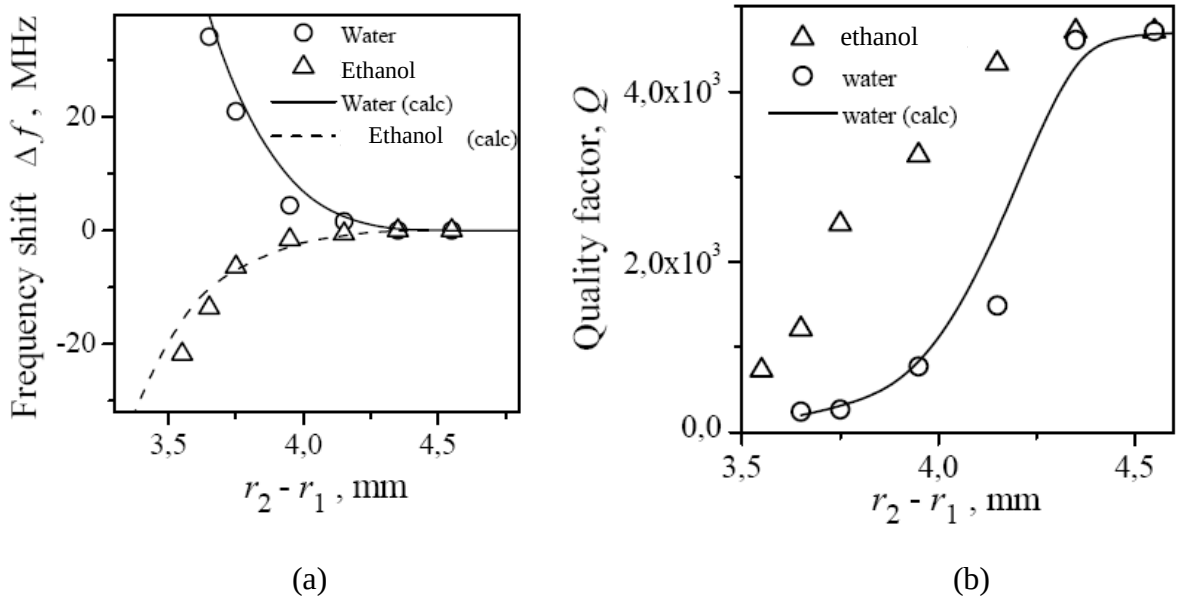

Figure 4.13 Dependencies of (a) frequency shift and (b) quality factor of the resonator filled with ethanol and water on radial thickness $r_2 - r_1$. The solid line is calculated for water taking into account microwave loss in the conducting endplates.

The dependencies of measured values Δf_{liq} and Q_{liq} on both parts, ε_{liq}' and ε_{liq}'', of complex permittivity complicate the analysis of errors of ε_{liq}', ε_{liq}'' measurements by means of the proposed technique. However, the most probable error (MPE) for the permittivity measurement can be evaluated on the base of the following expressions

$$\delta\varepsilon_{liq}' = \left\{ \left[\frac{\partial \varepsilon_{liq}'}{\partial \Delta f_{liq}} \delta(\Delta f_{liq}) \right]^2 + \left[\frac{\partial \varepsilon_{liq}'}{\partial Q_{liq}} \delta Q_{liq} \right]^2 \right\}^{1/2} \tag{4.12}$$

$$\delta\varepsilon_{liq}'' = \left\{ \left[\frac{\partial \varepsilon_{liq}''}{\partial \Delta f_{liq}} \delta(\Delta f_{liq}) \right]^2 + \left[\frac{\partial \varepsilon_{liq}''}{\partial Q_{liq}} \delta Q_{liq} \right]^2 \right\}^{1/2} \tag{4.13}$$

Values of $\delta(\Delta f_{liq})$ and ΔQ_{liq} in Eqs. (4.12), (4.13) are the measurement errors of frequency shift Δf_{liq} and quality factor Q_{liq}. The derivatives in Eqs. (4.12), (4.13) depend strongly on thickness $r_2 - r_1$ and the correlation of the dielectric constants of the liquids with that of the material of the external layer of two-layered WGM-resonator. The complex permittivity of lossy liquids $\varepsilon'_{liq} + i\ \varepsilon_{liq}''$ can be determined with sufficiently high accuracy using a resonator with a sapphire outer layer. Based on Eqs. (4.12), (4.13) the accuracy of complex permittivity measurement for distilled water is $\delta\varepsilon'/\varepsilon' \approx 0.24\%$, $\delta\varepsilon''/\varepsilon'' \approx 1\%$.

In Fig. 4.14 the resonator parameters are presented as concentration dependencies obtained at 38 GHz when the resonator was filled with aqueous solutions of glucose and albumin. The quality factors and resonant frequency shifts are recalculated into real and imaginary parts of dielectric permittivity of both kinds of liquids and plotted as functions of concentration (Fig. 4.15). The data indicate that for a given frequency the complex permittivity of glucose deviates stronger from water than albumin.

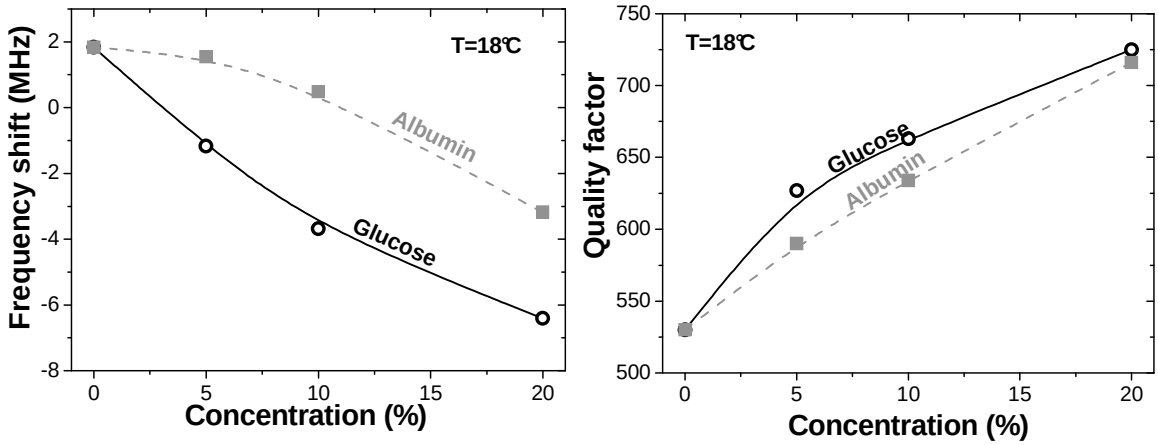

(a) (b)

Figure 4.14 (a) Frequency shift and (b) quality factor of a R2L WGM resonator with a binary glucose and lactalbumin aqueous solutions as functions of solute's weight concentration, mode $HE_{13\,2\,0}$ (TM), $r_2 - r_1 = 3.75$ mm.

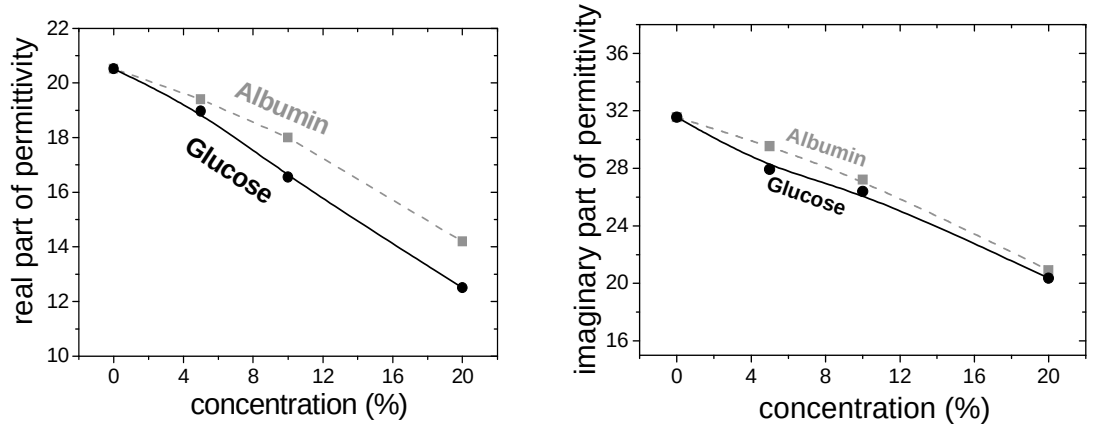

(a) (b)

Figure 4.15 (a) Real and (b) imaginary parts of permittivity of binary water-glucose and water-albumin solutions as functions of weight concentration.

4.3.2 Investigation of glucose and albumin-water droplets by an open WGM resonator

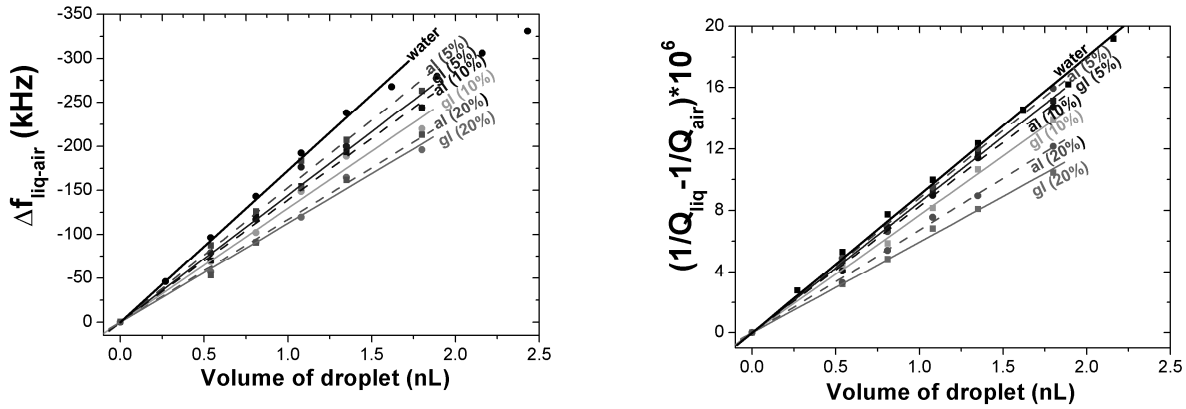

(a) (b)

Figure 4.16 Measured droplet induced changes of (a) resonant frequency $\Delta f_{liq\text{-}air}$ and (b) inverse quality factor $1/Q_{liq}$-$1/Q_{air}$ as functions of volume of bidistilled water and aqueous solutions of glucose (gl) and lactalbumin (al), all measurements at T=18°C.

The results on droplets depicted in Fig. 4.16 indicate that for concentrations down to 5% both solutions can be clearly separate from water. Qualitatively, there is a challenging similarity to ethanol and NaCl. Glucose, which is a complex organic molecule, simply reduces the concentration of "active" water molecules, which absorb electromagnetic energy by the dipole relaxation process. Therefore, both the inverse quality factor and resonant frequency are reduced by a similar percentage upon increasing the concentration of the solvent.

Similar to the analysis performed on ethanol solutions, in Fig. 4.17 the relative changes of frequency shift and change of inverse quality factor, as determined from the slopes in Fig. 4.15 (open symbols), are compared with the permittivity data obtained with the radially two layered resonator determined from Fig. 4.15 (full symbols). Both quantities show the same

tendencies, the differences in the details, in particular the non-monotonous concentration dependences, are not clear yet.

The relaxation time data depicted in Fig. 4.7, which were determined from the ratio of $\Delta(1/Q)$ and Δf slope according to Eq. (4.7), indicates a stronger slope with increasing concentration. In contrast, albumin is a charged protein. Broad band experiments on proteins indicate a $1/f$ part in the imaginary part of the permittivity at low frequencies [114]. According to Fig. 4.16, at respectively high frequency of 35 GHz the resulting change of inverse quality factor with increasing concentration of albumin is significantly smaller than for the observed frequency shift. Since the conductivity does not affect the imaginary part of permittivity at 35 GHz, the relaxation time can be determined the same way as for glucose (Fig. 4.7). The interpretation of the relaxation time data is not clear yet. In contrast to NaCl solutions, albumin shows a significant concentration dependence of ε'', which is due to an increase of the relaxation time with concentration, similar strong than for glucose at low concentration values. This is clear, because - in spite of ionic character – albumin influences the hydrogen bond network resulting in an increase of the relaxation time. In order to distinguish between ionic and non-ionic character of a solute, a lower measurement frequency would be advantageous, such that the conductivity could have a stronger effect on ε''.

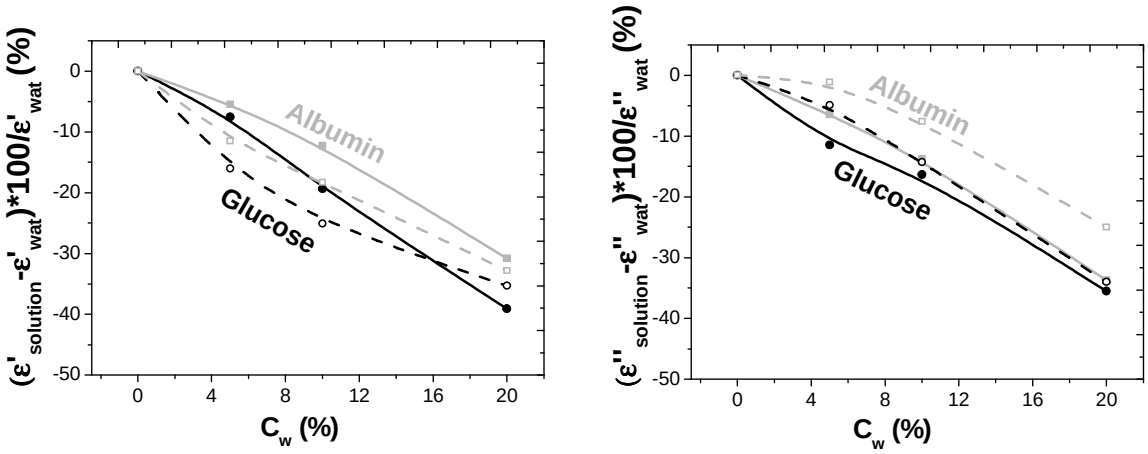

Figure 4.17 Experimental data on (a) real ε' and (b) imaginary ε'' parts of dielectric permittivity as function of concentration (C_w, %) of glucose and albumin in bidistilled water. Full symbols connected by full lines correspond to data obtained from measurements with the radially-two layered sapphire resonator (see Fig. 4.15) at 38 GHz. Open symbols connected by dashed lines are data taken from droplet measurements (Fig. 4.16) at 35 GHz.

Chapter 5: Towards biosensing applications: first microfluidic implementation and submillimetre wave WGM resonators

In the previous chapters it was demonstrated that evanescent field sensing by WGM resonators is very efficient for characterization of biochemical liquids of the smallest possible volumes. Therefore, the resonator approach shows interesting perspectives for the development of measurement and sensor arrangements utilizing several possible schemes:

- The first obvious extension of the work described so far is the dielectric resonator investigation on droplet-like objects at different frequency ranges within the microwave band. However, droplets of different liquids under test of ultra-small volumes are not sufficiently stable and apart from that, an expensive spotting-positioning system is required. Therefore, an integration of dielectric resonator with a microfluidic system becomes a compatible approach for some applications. This can be realized in two different ways:

i) either as a flip-chip configuration, i.e. a microfluidic system on a separated wafer will be attached to the WGM resonator;

ii) or as microfluidic system integrated directly within a resonator made of high resistive silicon, ceramic, or quartz, because micromachining on this materials is possible.

- The open WGM resonator in conjunction with dielectric waveguide excitation has shown a perspective to develop WGM resonators for evanescent field sensing applications at much higher frequencies. According to Eq.(3.8), the sensitivity for measuring of a small sample (such that perturbation theory can be applied) scales with $Q/V = Q \cdot f^3$ (V= resonator volume) for a cylindrical DR of given height-to-diameter ratio and for a given mode. This means, that increasing the frequency from 35 to, say 170 GHz, already allows an increase in sensitivity by a factor of 115, provided that the same quality factor can be achieved (which appears to be possible by using of highly resistive silicon). Such an increase will allow to measure dried or even frozen "solids", as being prepared by spotting nanolitre droplets of aqueous solutions of non-volatile substances on the resonator surface. This should allow the study of the dielectric properties of extremely small amount of solids, for example DNA. As an inspiring example, it was shown in the literature [115–117] that the hybridization of single DNA molecules leads to a measurable change of their electric permittivity at sub-Terahertz frequencies. This may pave a new way towards label-free DNA detection, if measurements on single pico- to nanolitre droplets of DNA-NaCl-water solutions can be performed. Therefore, arrays of several WGM dielectric resonators prepared by micromachining from highly resistive silicon may represent a promising approach towards label-free DNA analysis.

Alternatively, at terahertz frequencies biochemically activated resonator surfaces may allow the detection of the vibrational modes even on single molecular layers.

5.1 WGM sapphire resonator combined with a quartz wafer containing a nanoliter liquid filled cavity

The integration of microfluidic structures with coplanar waveguide transmission lines was reported recently [118, 119]. This technique enables to measure the dielectric properties of sub-μL volumes of fluids and biological samples at frequencies up to 40 GHz.

Kim et al [120] showed that the concentration of glucose in water can be determined by a ceramic dielectric resonator with a sensitivity of 3 % weight concentration from frequency shifts for the test liquid being confined in a small 4 μl volume cylindrical air gap, but with strong temperature control requirements. Within the work reported here (see also [121]), an attempt was made to construct a first approach towards an integrated microfluidic system based on our previous experience with WGM resonators described in the chapters before.

The approach discussed here is a flip-chip sensor composed of a simple quartz disk with a liquid cavity (representing a simple microfluidic system) being combined with a high-*Q* whispering-gallery sapphire resonator at a frequency of about ten gigahertz (within X_a frequency band).

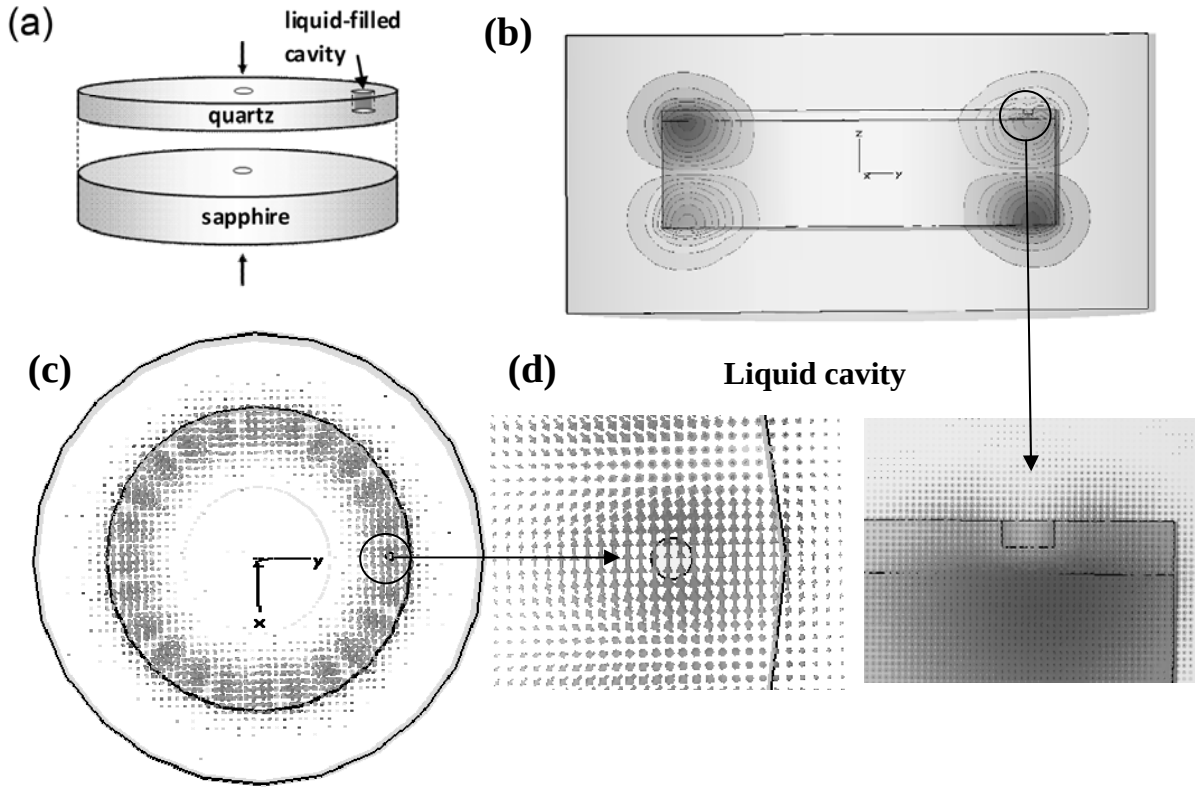

Figure 5.1 (a) Flip-chip high-*Q* resonator: bottom part – whispering-gallery sapphire disk, upper part – *c*-axis oriented quartz wafer with nanolitre cavity; simulated distribution of the electric field amplitude (b) front view and (c) top view at resonance showing the optimum position of the cavity filled with a test liquid; (d) the magnified field distribution inside and in the vicinity of the liquid cavity.

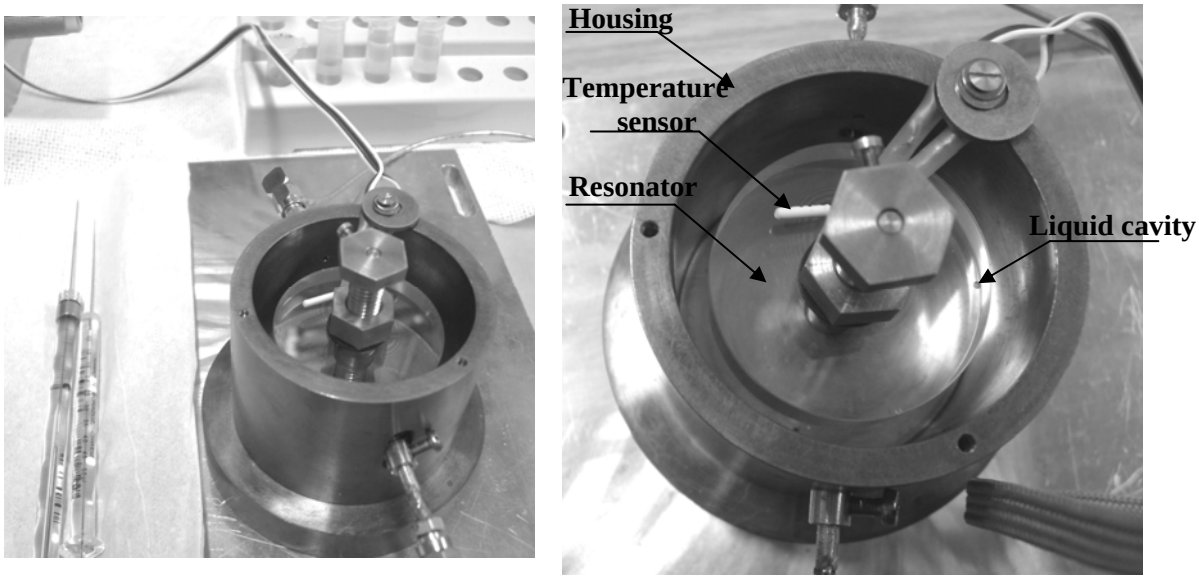

(a) (b)

Figure 5.2 (a) Photograph of the resonator section, (b) close view on the liquid cavity.

In comparison to the 35 GHz setup, the 11 GHz resonator and shielding cavity are relatively large, which makes it easier to demonstrate the general advantages of this approach with respect to the droplet experiments. On the other hand, the sensitivity is expected to be lower; such that larger liquid volumes are required. For the liquid cavity wafer, we choose quartz because of low microwave losses and demonstrated micromachining capability [122], which represents an essential requirement for a reasonable material combination comprising sufficiently high-Q. For simplicity, we employed a c-axis oriented quartz wafer of 1 mm thickness (Fig. 5.1(a)) with a single cavity of 1 mm diameter and 0.5 mm height prepared by ultrasound machining. The quartz wafer and a c-axis oriented sapphire disk of the same diameter (d=40.5 mm; h=10.8 mm, the dimensions were scaled from the resonator 3 described in Chapter 3 and 4) were attached to each other and fixed by a screw inside the central hole in both parts. This flip-chip assembly was mounted inside a semi-open copper housing (Fig. 5.2). The dielectric resonator was excited in a whispering gallery resonance of type $HE_{12\,1\,\delta}$ at a resonant frequency of 11.62 GHz by coupling loops. The position of the cavity was optimized with respect to the calculated field distribution (Microwave Studio software by CST) shown in Fig. 5.1. According to the simulation results the axially electric field strongly bends near the cylindrical top and bottom surface of the sapphire cylinder, such that the electric field at the location of the liquid cavity is almost parallel to the surface. Therefore, the electric field is perpendicular to the circular surface of the liquids cavity, which leads to a less strong field deformation by a high permittivity liquid than an electric field parallel to the field direction. However, in contrast to the droplet experiments the local field deformation (term in bracket in Eq.(3.8), Chapter 3) cannot be neglected.

With this assembly we achieved a Q-factor of $1.1 \cdot 10^5$, which is close to the maximum achievable value determined by the intrinsic dielectric losses of sapphire [56].

Broadband (45MHz – 20 GHz) complex permittivity measurements by the Agilent coaxial probe technique (see Fig. 2.5, Chapter 2) on aqueous solutions with different concentrations of methanol, ethanol and glucose as well as oil, benzene and glycerine were employed to calibrate the sensor over a wide range of values for real (ε') and imaginary parts (ε'') of permittivity, the results are shown in Fig. 5.3.

The resonator measurements were performed as follows. The cavity was filled with the test liquid of 400 nl volume by a Hamilton syringe-micropipette. Similar to the droplet experiments, the liquid induced changes of resonant frequency, Δf, change of inverse quality factor $\Delta(1/Q)$, and change of the transmission coefficient S_{21} at the resonance frequency were measured with an Agilent N5230A vector network analyzer. Fig. 5.4(a) shows the measured liquid induced frequency shift value of the resonator with respect to air ($\Delta f_{liq\text{-}air}=f_{liq}-f_{air}$) as a function of real part of permittivity ε' for aqueous solutions of ethanol and methanol, pure glycerine, oil and benzene. Fig. 5.4(b) shows the corresponding resonator loss values (liquid induced change of inverse quality factor) as a function of the loss tangent $\tan\delta = \varepsilon'' / \varepsilon'$. The results indicate that real and imaginary part can be clearly separated. The losses are proportional to the loss tangent, but the frequency shift shows a stronger dependence on ε' for small values of permittivity. This demonstrates that for diluted aqueous solutions the losses are much more sensitive to concentration changes than the frequency shift.

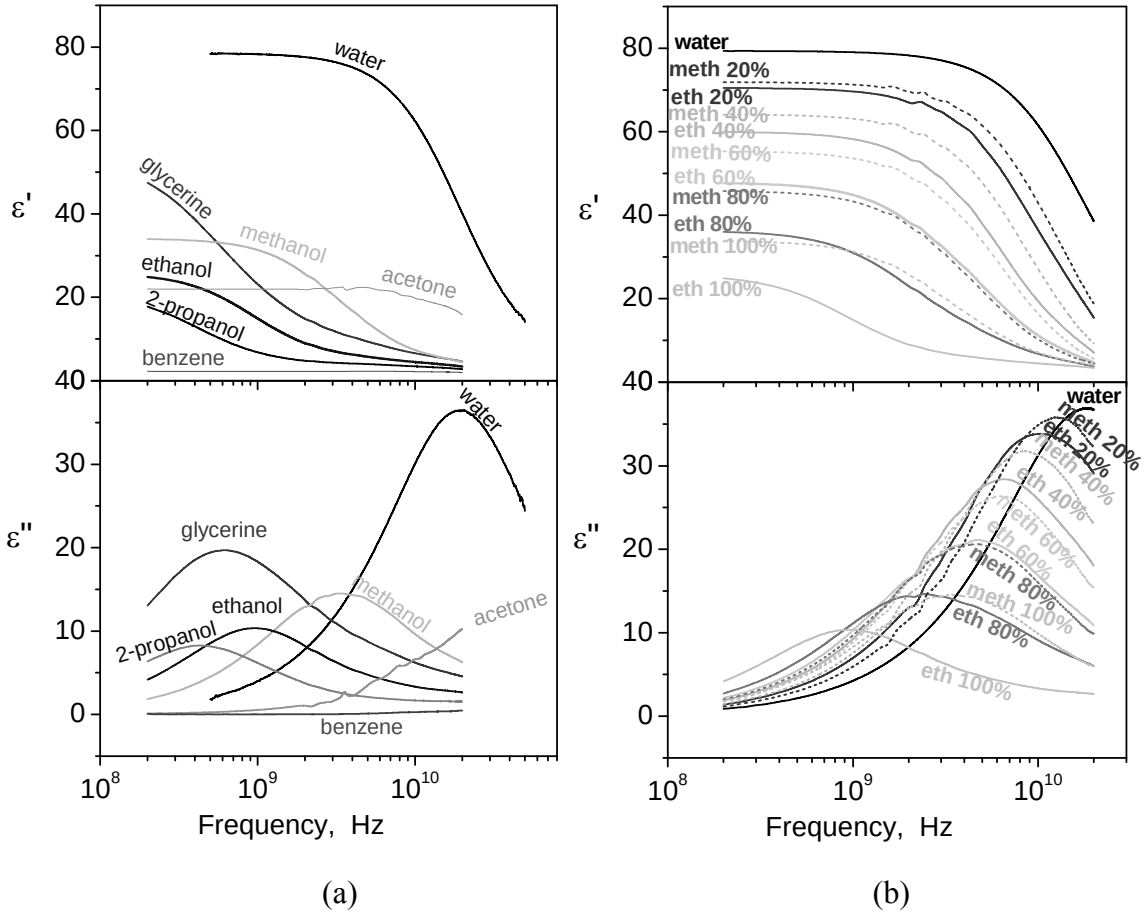

Figure 5.3 Dielectric spectra of several selected "reference liquids" measured by the broadband coaxial probe technique.

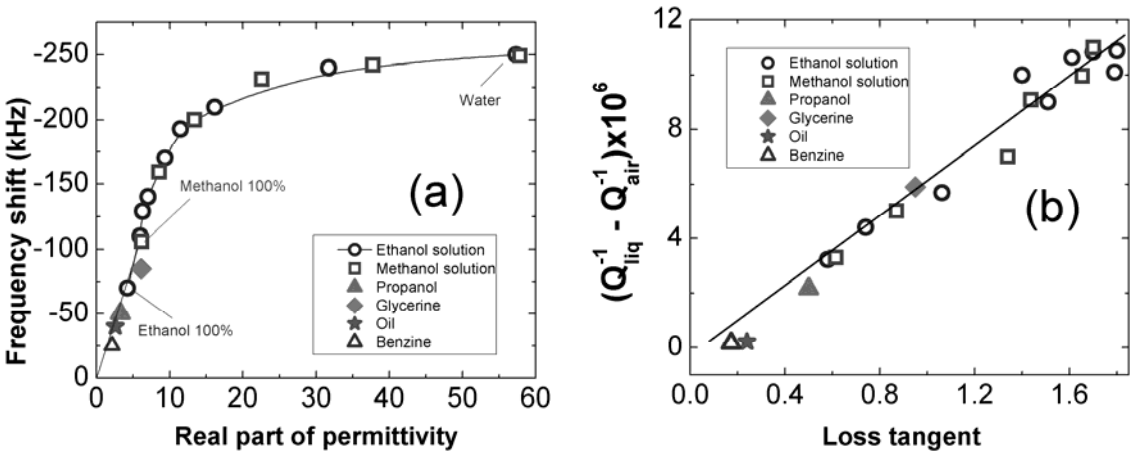

Figure 5.4 Measured liquid induced changes of (a) frequency shift $\Delta f_{liq\text{-}air}=f_{liq}-f_{air}$ as a function of real part of permittivity of liquids under test selected to cover a wide epsilon range; (b) inverse quality factor $1/Q_{liq}$-$1/Q_{air}$ as a function of loss tangent (T = 24 °C).

The separation of real and imaginary parts is expected by perturbation theory (Eqs.(3.8) and (3.9), Chapter 3). For low permittivity liquids (typically lower than the permittivity of sapphire), dielectric screening is negligible ($E_1 = E_0$), corresponding to the observed linear dependence according to Fig. 5.4(a). For higher values of permittivity, screening becomes more significant ($E_1 < E_0$), leading to a weaker dependence of frequency shift on permittivity. In case of an electric field perpendicular to the quartz-liquid interface $E_1 = E_0 / \varepsilon'$ holds, such that the frequency shift becomes nearly independent on ε' according to Eq. (3.8), in qualitative agreement with the experimental results shown in Fig. 5.4(a).

Eq. (3.9) from Chapter 3 explains qualitatively the observed linear dependence for liquids with permittivity above 10 and the sub-linear dependence observed for oil, glycerine, benzene and highly concentrated methanol, according to Fig. 5.4(b).

In Fig. 5.5 the behaviour of the ε' and tanδ with measured resonator frequency shift is compared with the change of inverse quality factor as functions of concentration for aqueous solutions of methanol and ethanol. As expected from our previous considerations, changes of the inverse Q represent a highly sensitive measure of the concentration in case of low concentration values. In order to demonstrate the high sensitivity of our technique for an aqueous solution with high relevance for biosensor applications, we have measured diluted solutions of glucose.

The measured solid linear curve depicted in Fig. 5.6 (a) shows the transmission coefficient at resonance S_{21}, which apparently exhibits much less data scattering then the linear frequency shift curve (dashed line in Fig. 5.6(a)). From measurements of the temperature dependence of resonant frequency and quality factor between 18 and 28 °C (not shown in the figure) we found that a change of concentration of 1% corresponds to a frequency shift caused by a temperature change of only 1 mK. This strong effect is caused by the temperature dependence of the permittivity of sapphire, which is about 100 ppm /K [123], frequency changes due to the temperature dependence of water are very small. In strong contrast, for the temperature variation of the liquid induced change of the inverse quality

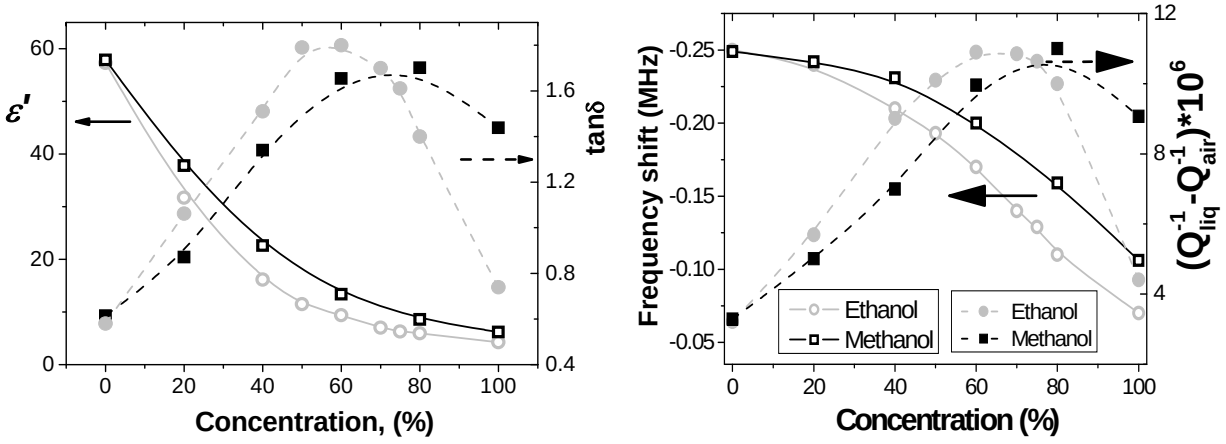

(a) (b)

Figure 5.5 Measured concentration dependence of ε' and $\tan\delta$ (data extracted from Fig. 5.3) and solution induced changes of resonant frequency shift $\Delta f_{liq\text{-}air}$ and inverse quality factor $1/Q_{liq}$-$1/Q_{air}$ as functions of ethanol and methanol solution concentration (T = 24 °C): circles – ethanol solutions, squares – methanol solutions.

factor the temperature dependence of the losses of the empty resonator can be neglected, because of the extremely low losses of sapphire and high losses of water in the range of 10 GHz. To proof this assumption, we analysed the theoretically expected temperature dependences. The complex permittivity of aqueous solutions of non-ionic solutes such as alcohol or glucose can be well described by the Debye formula (see for example Eq.(4.1) in Chapter 4). According to Eq. (4.6), the loss tangent is proportional to the relaxation time. For highly diluted aqueous solution at 10 GHz this approximation holds well ($\varepsilon_\infty/\varepsilon''$=4/33 = 0.12<< 2 = 1/($\omega\tau$)). According to Eq.(1.48) from Chapter 1 the temperature dependence of the loss tangent can be written as:

$$\tan\delta(\omega,T) \approx \omega\tau(T) = \omega\tau(300K)\frac{300\mathrm{K}}{T}\exp\left(\frac{\Delta H}{k}\frac{300\mathrm{K}}{T}\right) \qquad (5.1)$$

For pure *water,* the relaxation enthalpy ΔH is 0.196 eV [6].

In contrast to the droplet experiments, the frequency shift exhibits only a weak dependence on real part of permittivity (see Fig. 5.4 (a)), such that the changes of inverse quality factor are proportional to $\tan\delta$ (assuming $\Delta f/f$ in Eq. (3.9) to be concentration independent). Therefore, we expect that $\Delta(1/Q)$ should exhibit temperature dependence according to Eq. (5.1). Fig. 5.6 (b) shows the corresponding temperature measurements for water and a 10% glucose solution. The slope for water is in very good agreement with the literature value. Notice that the data scattering apparent in Fig. 5.6(b) is caused by the applied -3dB halfwidth method.

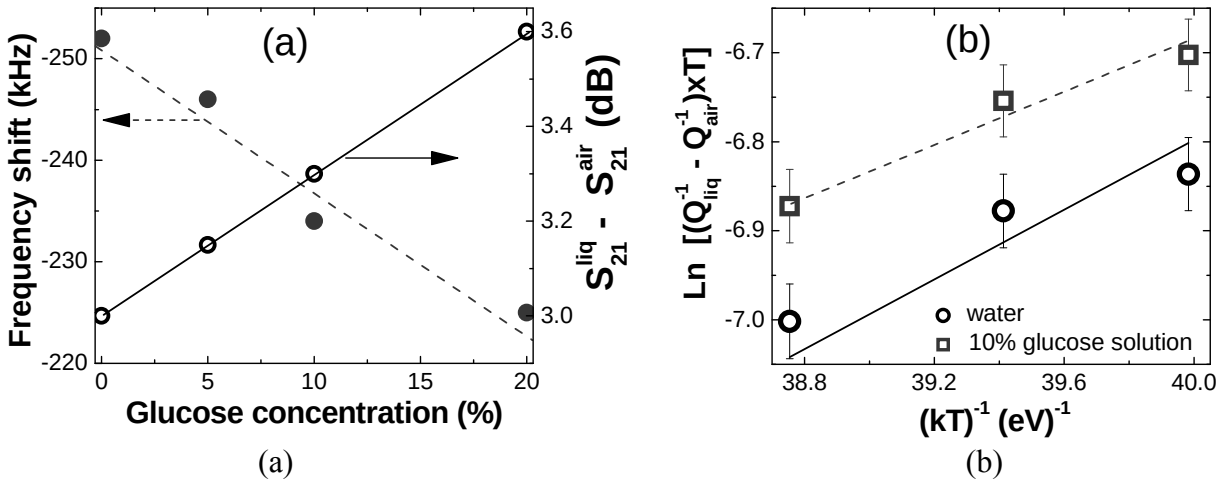

(a) (b)

Figure 5.6 (a) Measured solution induced changes of resonant frequency $\Delta f_{liq\text{-}air}$ and change of transmission coefficient $S_{21}{}^{liq} - S_{21}{}^{air}$ as a function of glucose concentration (T=24°C); (b) Logarithm of inverse quality factor change $1/Q_{liq}$-$1/Q_{air}$ multiplied by T as a function of inverse thermal energy kT. The solid line represents calculation results using Eq. (5.1) for ΔH = 0.196 eV corresponding to water.

Therefore, the maximum achievable sensitivity for concentration determination according to Fig. 5.6 (b) is determined by the temperature dependence of the relaxation time of the liquid. From the horizontal displacement between the linear temperature curves for pure water and for the 10 % glucose solution in Fig. 5.6 (b) one can estimate that a temperature change by 6.5 K causes the same effect as a concentration change by 10 %. Considering the linear characteristics indicated by Fig. 5.4 (a), we can conclude that for a practical microfluidic glucose sensor with temperature being stabilized to 10 mK, the expected sensitivity corresponds to a glucose concentration of 0.15 ppt. For the current setup the limitation of sensitivity is determined by the resolution of amplitude measurements, which is about 0.01 dB corresponding to a weight concentration sensitivity of 0.1 %.

In summary, we have studied the molecular relaxation time from microwave loss measurements of diluted aqueous solutions of organic molecules of nanolitre-volume liquid using our developed flip-chip resonator technique. The slope of $\Delta(1/Q)$ as a function of temperature for water is in very good agreement with the literature data. Our analysis of concentration and temperature dependence of the resonator losses in the framework of the Debye model revealed a sensitivity of 0.1% for concentration measurements on aqueous solutions of glucose of 400 nanolitre volume. Due to compact size, relatively low cost and short measurement time our developed high-sensitive flip-chip resonator can be used in medicine, chemistry and biology.

5.2 WGM resonator approach at 170 GHz

For possible terahertz biosensing applications we performed first simulations with Microwave Studio about excitation of more than one resonator by one common pair of feed lines. As it is shown in Fig. 5.7 three sapphire resonators being slightly separated in resonance frequency (by a slight diameter variation invisible in Fig. 5.7) can be excited with one pair of dielectric image guides. The prototype consisting of three sapphire resonators excited by

dielectric image waveguides can distinguish between different liquids simultaneously, sweeping in the frequency range around 170 GHz. As indicated by the grey resonance curves in Fig. 5.7, the effect of a small water droplet on resonator 2 and a small ethanol droplet on resonator 3, but no droplet on resonator 1, can be clearly resolved.

In practice the first measurements on single reaction and transmission type WGM resonators machined form sapphire and quartz at 170 GHz were performed. Photographs of these setups are shown in Fig. 5.8. Measurements were carried out with a Scalar Network Analyzer including mm-wave fullband waveguide signal generator based on a single broadband backward wave oscillator tube (BWO) which is capable to cover the entire 118-178 GHz waveguide band.

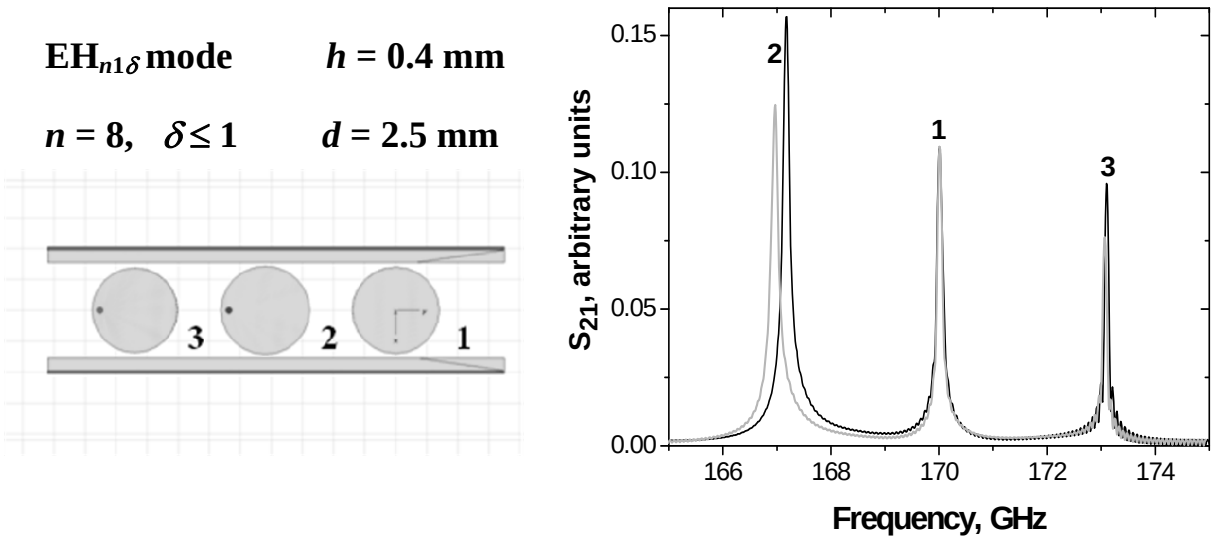

Fig. 5.7 Simulated resonant response of 3 sub-millimeter wave WGM sapphire resonators excited by a pair of common feedlines. Resonator 1 without droplet is a reference one; resonator 2 with a droplet of water; resonator 3 with a droplet of ethanol of the same volume.

Fig 5.9 represents a spectrum obtained for a single SiO_2 resonator depicted on Fig. 5.8 (b). At frequency f=172 GHz the quartz resonator demonstrates very high Q of around 28000, which is much higher than Q obtained with sapphire resonator in the same frequency range. Therefore the multiple resonator arrays will be convenient to combine with the microdroplet-spotting equipment in order to continue the investigation at higher frequencies in the future.

The experimental spectra obtained for these two resonators indicate that quartz is a much more perspective material for resonators in this frequency range than sapphire, because its resonances are characterized by a much higher Q-factor.

It is planned to develop integrated terahertz resonator arrays from quartz and high resistive silicon, which has a similar dielectric permittivity than sapphire, but much lower losses at terahertz frequencies.

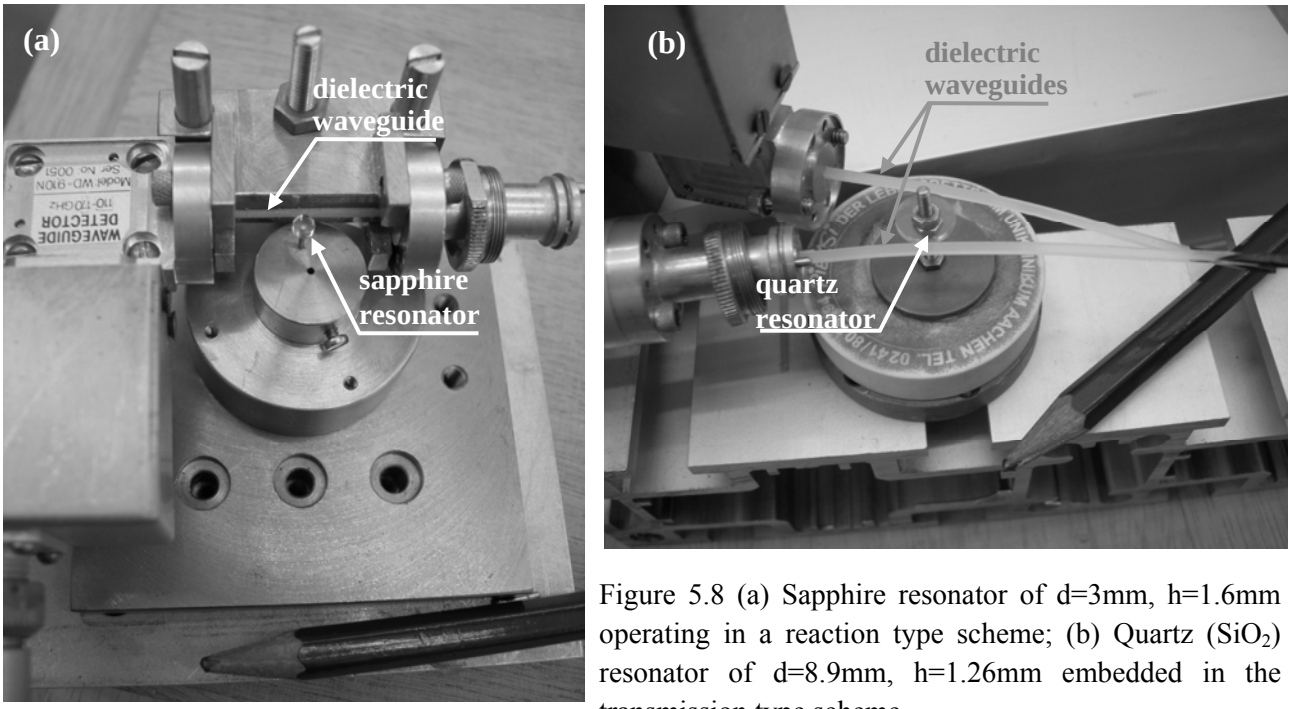

Figure 5.8 (a) Sapphire resonator of d=3mm, h=1.6mm operating in a reaction type scheme; (b) Quartz (SiO_2) resonator of d=8.9mm, h=1.26mm embedded in the transmission type scheme.

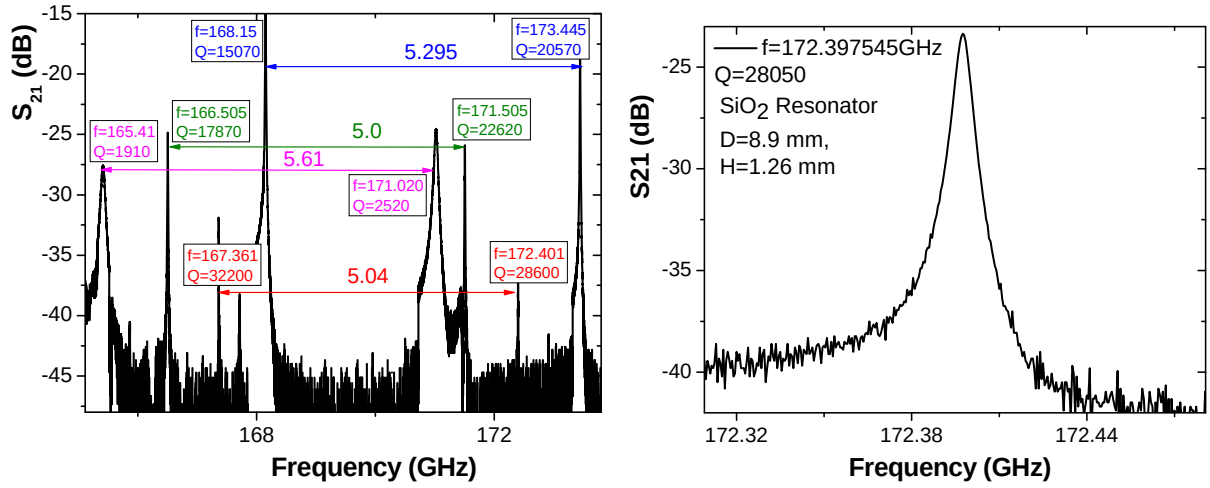

(a) (b)

Figure 5.9 (a) Spectrum measured for a single quartz resonator. (b) Zoomed view of a high-Q WGM resonance.

Chapter 6: Conclusion and Outlook

In the frame of this thesis it was shown, that whispering gallery mode resonators can be utilized as very sensitive systems for the microwave characterization of liquids comprising volumes of nanolitres only. Droplets spotted on the resonator surface with volumes as small as 100 pl and liquids inside a microfluidic cavity of 400 nl volume were investigated. For both cases, perturbation theory in conjunction with numerical simulations of the electromagnetic field distribution of the unperturbed (without test liquid) resonator revealed real and imaginary part of the dielectric permittivity of the liquid under test. The application of this method to diluted aqueous solutions allows for a highly precise determination of their concentration. Although the measurements on liquids were performed at 10 and 35 GHz within this thesis, the developed methods can be applied up the terahertz frequency range, as demonstrated by first successful operation of a whispering gallery resonator at 170 GHz. As a calibration standard, a special whispering gallery resonator comprising a radially symmetric (with respect to the resonator) liquid cell was investigated and employed.

Interesting perspectives result from the findings of this thesis: At first, a prototype for a simple dielectrometer for those liquids, which are only available in very small volumes, such as certain proteins or DNA solutions, was successfully demonstrated. Similar volume restrictions are expected for liquid explosives and other harmful chemical and biological liquids. Although the complex permittivity is only measured at one frequency, the two-parameter space of real- and imaginary parts of permittivity provides a high selectivity; multimode or multiresonator methods could even enhance significantly the selectivity in the future.

The high quality factor of whispering gallery mode sapphire resonators makes the liquid sensor method extremely sensitive for monitoring small changes of the loss tangent, which is closely related to the relaxation time of orientational dipole relaxation. This allows to determine the concentration of highly diluted solutions, such as glucose in water or water in benzene or oil. The first is interesting for medical applications and food industry, the later for monitoring the quality of petrochemical products such as benzene.

Aiming towards practical sensor systems, closed microfluidic systems will be the next step with emphasis on a constant liquid volume, reproducible and versatile filling procedures and a stabilized resonator temperature. For such systems practical applications can be expected. In the frequency range of about 10 GHz, the network analyzer can be replaced by a compact and highly integrated (typically a one platine solution) measurement circuit, such that compact and moderate-cost sensor systems appear to be realistic. Beyond measurements on nanolitre volumes, a resonator attached to the skin of a human body may provide an indirect measure of the glucose content in blood. The penetration depth of the evanescent field into the skin can be controlled and optimized for a given task by selecting resonator geometry (resonator length to height ratio) and azimuthal mode number.

Another great challenge is expected upon scaling the resonator dimensions down such that the resonance frequencies are in the terahertz range. In particular, for highly resistive silicon as resonator material the dielectric losses are very low, extremely high Q values in the

10^6 range can be expected for room temperature operation. Although such a small system would be already too sensitive for liquid identification, it could be employed for permittivity measurements on spotted biomolecular samples after drying or freezing (the latter would provide DNA in a low-loss ice matrix, eliminating the effect of salt crystal formation appearing after drying). For the terahertz frequency range, the dielectric resonator and the dielectric (image) coupling waveguides need to be integrated on one chip. Advanced micromachining techniques such as high aspect ratio chemical or reactive ion etching have to be employed and optimized for structure manufacturing. Form point of view of measurement, multiplied solid state sources and bolometric detectors, in the future also quantum cascade lasers, could be employed. As demonstrated by simulations within this thesis, excitation of several whispering gallery resonators by a common feed-line would pave the way towards the realization of a terahertz biochip. For such an ambitious project, biochemical functionalization of the resonator surface needs to be realized. Even a single virus on such a highly sensitive surface may lead to virus specific change of the resonator quality factor.

In summary, this thesis has opened the gate to a further extension of microwave, millimetre wave and terahertz technology towards highly accurate and selective sensor applications with a strong potential for life science. It can be expected, that the full potential will be exploited within the next few years and first practical sensor products will appear on the market.

Appendix A: The dielectric disk WGM resonator with CEP

In appendix A and B the CGS unity system is used, in contrast to the main chapters of the thesis.

The open cylindrical WGM resonator shown in Fig. 3.17(a) manufactured from an uniaxial crystal is characterized by the tensor of dielectric permittivity

$$[\varepsilon_{ij}] = \begin{cases} \delta_{ij}, & r > r_0 \\ \begin{bmatrix} \varepsilon_\perp & 0 & 0 \\ 0 & \varepsilon_\perp & 0 \\ 0 & 0 & \varepsilon_z \end{bmatrix}, & r \le r_0 \end{cases}$$

where ε_z and $\varepsilon_\perp$ are the [ε_{ij}] components in the parallel and perpendicular directions of the crystal optical axis; which is parallel to the cylinder axis; r_0 is resonator radius; δ_{ij} is the Kroneker symbol.

For the aim to find the field distribution in any volume, including cylinder, Maxwell's equations (1.1) have to be solved. For the case of a cylinder this is more convenient to express them in the cylindrical coordinate system in the following form:

$$\begin{cases} \dfrac{1}{r}\dfrac{\partial H_z}{\partial \varphi} - \dfrac{\partial H_\varphi}{\partial z} = -ik_0 \varepsilon_\perp E_r \\ \dfrac{\partial H_r}{\partial z} - \dfrac{\partial H_z}{\partial r} = -ik_0 \varepsilon_\perp E_\varphi \\ \dfrac{1}{r}\left[\dfrac{\partial}{\partial r}(rH_\varphi) - \dfrac{\partial H_r}{\partial \varphi}\right] = -ik_0 \varepsilon_\parallel E_z \end{cases} \qquad \text{(A.1)}$$

And taking into account μ_r =1:

$$\begin{cases} \dfrac{1}{r}\dfrac{\partial E_z}{\partial \varphi} - \dfrac{\partial E_\varphi}{\partial z} = ik_0 H_r \\ \dfrac{\partial E_r}{\partial z} - \dfrac{\partial E_z}{\partial r} = ik_0 H_\varphi \\ \dfrac{1}{r}\left[\dfrac{\partial}{\partial r}(rE_\varphi) - \dfrac{\partial E_r}{\partial \varphi}\right] = ik_0 H_z \end{cases} \qquad \text{(A.2)}$$

where (r, z and φ) are cylindrical coordinates; $k_0 = (\omega' - i\omega'')/c$; ω' and ω'' are real and imaginary parts of the resonance frequency ($\omega'' \ge 0$); c is the light velocity.

Consider harmonic oscillations ($\vec{E}$, $\vec{H} \sim e^{-i\omega t}$) The transverse components of the electromagnetic field can be expressed by means of the axial components E_z and H_z in the following way

$$\begin{cases} E_\varphi = \dfrac{i}{q^2}\left(\dfrac{k_z}{r}\dfrac{\partial}{\partial\varphi}E_z - k_0\dfrac{\partial}{\partial r}H_z\right) \\ E_r = \dfrac{i}{q^2}\left(k_z\dfrac{\partial}{\partial r}E_z + \dfrac{k_0}{r}\dfrac{\partial}{\partial\varphi}H_z\right) \\ H_\varphi = \dfrac{i}{q^2}\left(k_0\varepsilon_\perp\dfrac{\partial}{\partial r}E_z + \dfrac{k_z}{r}\dfrac{\partial}{\partial\varphi}H_z\right) \\ H_r = \dfrac{i}{q^2}\left(k_z\dfrac{\partial}{\partial r}H_z - \dfrac{k_0\varepsilon_\perp}{r}\dfrac{\partial}{\partial\varphi}E_z\right) \end{cases} \quad \text{(A.3)}$$

where $q^2 = \begin{cases} q_H^2, & r \le r_0 \\ q_0^2, & r \ge r_0 \end{cases}$, k_z is the axial component of the wave vector

We can define the axial component of the HE mode inside of the resonator ($r \le r_0$) substituting the third and the fourth equations of the system (A.3) in the third Eq. (A.1):

$$\Delta_\perp E_z = -\frac{\varepsilon_\parallel(k_0^2\varepsilon_\perp - k_z^2)}{\varepsilon_\perp}E_z \quad \text{(A.4)}$$

where $\Delta_\perp = \dfrac{1}{r}\dfrac{\partial}{\partial r}\left(r\dfrac{\partial}{\partial r}\right) + \dfrac{1}{r^2}\dfrac{\partial^2}{\partial\varphi^2}$.

We can define axial component of the EH mode inside of the resonator substituting the first and the second equations of the system (A.3) in the third Eq. (A.2):

$$\Delta_\perp H_z = -(k_0^2\varepsilon_\perp - k_z^2)H_z \quad \text{(A.5)}$$

Similar transformations can be performed for the case $r > r_0$ (outside the resonator):

$$\Delta_\perp E_z = -(k_0^2 - k_z^2)E_z \quad \text{(A.6)}$$

$$\Delta_\perp H_z = -(k_0^2 - k_z^2)H_z \quad \text{(A.7)}$$

The solution for the Eq. A.4 and A.5 for the case ($r \le r_0$) (the field inside the resonator) can have the following form:

$$E_z = B_n J_n(q_E r)e^{i(n\varphi + k_z z - \omega t)};\ H_z = A_n J_n(q_H r)e^{i(n\varphi + k_z z - \omega t)}, \quad \text{(A.8)}$$

And the solution of the Eq. A.6 and A.7 for the field outside the resonator ($r > r_0$) can be written in the form:

$$E_z = R_n H_n^{(1)}(q_0 r)e^{i(n\varphi + k_z z - \omega t)};\ H_z = G_n H_n^{(1)}(q_0 r)e^{i(n\varphi + k_z z - \omega t)}, \quad \text{(A.9)}$$

where A_n, B_n, R_n and G_n are constants, $J_n(z)$ and $H_n^{(1)}(z)$ are n-th order Bessel and Hankel cylindrical functions of the first kind, respectively; $n = 0,1,2,\ldots$, q_H, q_E and q_0 - are the axial components of wave vector inside and outside the resonator, correspondingly. Substitute Eq. (A.8) in Eq. (A.5) and (A.6) one obtains:

$$q_E^2 r^2 J_n^{"}(q_E r) + q_E r J_n^{'}(q_E r) - r^2\left[\frac{n^2}{r^2} - \frac{\varepsilon_{\|}}{\varepsilon_{\perp}}(k_0^2\varepsilon_{\perp} - k_z^2)\right] J_n(q_E r) = 0 \tag{A.10}$$

$$q_H^2 r^2 J_n^{"}(q_H r) + q_H r J_n^{'}(q_H r) - r^2\left[\frac{n^2}{r^2} - (k_0^2\varepsilon_{\perp} - k_z^2)\right] J_n(q_H r) = 0 \tag{A.11}$$

where prime means the derivative of the functions $J_n(q_E r)$ and $J_n(q_H r)$.

Eq. (A.10) is Bessel equation at the condition $-r^2\left[\frac{n^2}{r^2} - \frac{\varepsilon_{\|}}{\varepsilon_{\perp}}(k_0^2\varepsilon_{\perp} - k_z^2)\right] = q_E^2 r^2 - n^2$, resulting in $q_E^2 = \frac{\varepsilon_{\|}}{\varepsilon_{\perp}}(k_0^2\varepsilon_{\perp} - k_z^2)$. For Eq. (A.11) an analogue condition has to be implemented: $-r^2\left[\frac{n^2}{r^2} - (k_0^2\varepsilon_{\perp} - k_z^2)\right] = q_H^2 r^2 - n^2$, which gives $q_H^2 = k_0^2\varepsilon_{\perp} - k_z^2$. Therefore, $q_E^2 = \frac{\varepsilon_{\|}}{\varepsilon_{\perp}} q_H^2$.

Substitute expression (A.9) correspondingly in (A.6) and (A.7), one can obtain an expression for the case $r > r_0$. Under similar conditions one can obtain the expressions for the axial components of the wave number for the HE and EH modes: $q_{0H}^2 = q_{0E}^2 = q_0^2$, where $q_0^2 = k_0^2 - k_z^2$.

Boundary conditions

At the surface *S* where the parameters ε and μ change, the electromagnetic field equations should be completed by boundary conditions:

$$E_\tau^{(1)} = E_\tau^{(2)}; H_\tau^{(1)} = H_\tau^{(2)} \tag{A.12}$$

The index τ defines the tangential components. Utilizing the cylindrical coordinate system, one can write the boundary conditions in the form:

$$E_z^{(1)}(r_o) = E_z^{(2)}(r_o); \tag{A.13}$$

$$E_\varphi^{(1)}(r_o) = E_\varphi^{(2)}(r_o); \tag{A.14}$$

$$H_z^{(1)}(r_0) = H_z^{(2)}(r_0); \tag{A.15}$$

$$H_\varphi^{(1)}(r_0) = H_\varphi^{(2)}(r_0) \tag{A.16}$$

Taking into account the presence of the return (reflected) wave in the resonator, one can rewrite (A.8) in a form $H_z = A_n J_n(q_H r)e^{i(n\varphi+k_z z-\omega t)} + \tilde{A}_n J_n(q_H r)e^{i(n\varphi+k_z z-\omega t)}$, $E_z = B_n J_n(q_E r)e^{i(n\varphi+k_z z-\omega t)} + \tilde{B}_n J_n(q_E r)e^{i(n\varphi+k_z z-\omega t)}$, where $\tilde{A}_n = -A_n$ and $\tilde{B}_n = B_n$. Therefore, Eq. (A.8) for the case of $r \le r_0$ becomes

$$H_z = C_n J_n(q_H r)\sin(k_z z)e^{i(n\varphi-\omega t)} \tag{A.17}$$

$$E_z = D_n J_n(q_E r)\cos(k_z z)e^{i(n\varphi-\omega t)} \tag{A.18}$$

where $C_n = 2iA_n$, $D_n = 2B_n$.

Analogically for the case $r > r_0$ we have

$$E_z = D_n \frac{J_n(q_E r_0)}{H_n^{(1)}(q_0 r_0)} H_n^{(1)}(q_0 r)\cos(k_z z)e^{i(n\varphi-\omega t)} \tag{A.19}$$

$$H_z = C_n \frac{J_n(q_H r_0)}{H_n^{(1)}(q_0 r_0)} H_n^{(1)}(q_0 r)\sin(k_z z)e^{i(n\varphi-\omega t)} \tag{A.20}$$

Boundary conditions for the conducting endplates made of an ideal conductor at $z = 0$ and $z = h$. The axial component of the wave vector are $k_z = m\pi/l$, m=0,1,2,...

In the case m = 0 ($\frac{\partial}{\partial z} = 0$) the fields are axially homogeneous.

Dispersion equation

Substituting field components E_z and H_z from Eq. (A.8) and (A.9) correspondingly in the left and right sides of the Eq. (A.13) and (A.15) one obtains

$$R_n = B_n \frac{J_n(q_E r_0)}{H_n^{(1)}(q_0 r_0)}; \qquad G_n = A_n \frac{J_n(q_H r_0)}{H_n^{(1)}(q_0 r_0)}. \tag{A.21}$$

Substitute E_φ and H_φ field components from the first and the third equations of the system (A.3) correspondingly into Eq. (A.14) and (A.16), and taking into account (A.21), one obtains the following expressions

$$\frac{ik_z n}{r_0} B_n \frac{J_n(q_E r_0)}{J_n(q_H r_0)}\left(\frac{1}{q_H^2} - \frac{1}{q_0^2}\right) = k_0\left(\frac{1}{q_H} A_n \frac{J_n'(q_H r_0)}{J_n(q_H r_0)} - \frac{1}{q_0} A_n \frac{H_n^{(1)'}(q_0 r_0)}{H_n^{(1)}(q_0 r_0)}\right); \tag{A.22}$$

$$\frac{ik_z n}{r_0} A_n \frac{J_n(q_H r_0)}{J_n(q_E r_0)}\left(\frac{1}{q_H^2} - \frac{1}{q_0^2}\right) = k_0\left(\frac{1}{q_0} B_n \frac{H_n^{(1)'}(q_0 r_0)}{H_n^{(1)}(q_0 r_0)} - \frac{q_E}{q_H^2}\varepsilon_\perp B_n \frac{J_n'(q_E r_0)}{J_n(q_E r_0)}\right) \tag{A.23}$$

Multiplying expressions (A.22) and (A.23), we obtain the **dispersion equation**:

$$(X_H - X_0)(\frac{\varepsilon_\perp q_E}{q_H} X_E - X_0) = C\,,$$

where: $X_H = \frac{1}{q_H}\frac{J_n^{'}(q_H r_0)}{J_n(q_H r_0)}$; $X_E = \frac{1}{q_H}\frac{J_n^{'}(q_E a)}{J_n(q_E a)}$; $C = \frac{k_z^2 n^2}{k_0^2 r_0^{\,2}}(\frac{1}{q_H^2} - \frac{1}{q_0^2})^2$; $X_0 = \frac{1}{q_0}\frac{H_n^{(1)'}(q_0 r_0)}{H_n^{(1)}(q_0 r_0)}$.

We can rewrite the dispersion equation in the more simple form

$$a_H a_E = a \tag{A.24}$$

where $a_H = X_H - X_0$; $a_E = \varepsilon_z X_E - X_0$; $a = \left[\frac{k_0 k_z n}{q_0^2 q_H^2 r_0^2}(1-\varepsilon_\perp)\right]^2$

Therefore, in the cylindric WGMR there exist two types of independent modes: HE, for which $|E_z\|_{\cos(k_z z)=1} >> |H_z\|_{\sin(k_z z)=1}$, and the constants B_n and R_n defined from the conditions of excitation, and EH, for which $|E_z\|_{\cos(k_z z)=1} << |H_z\|_{\sin(k_z z)=1}$, and the constants A_n and G_n obtained from excitation conditions. The following condition $\left|(X_H - X_0)^{1/2}(\frac{\varepsilon_\perp q_E}{q_H} X_E - X_0)^{-1/2}\right| = \left|\sqrt{a_H / a_E}\right| >> 1$ is valid for the HE mode and for the EH mode it is just opposite.

The energy of the electromagnetic field in the resonator one can describe in the following form:

$$W_{em} = \frac{1}{8\pi}\int_{\mathrm{v}} (\mathbf{ED} + \mathbf{HB}) d\mathrm{v} \tag{A.25}$$

where $\mathbf{D} = \left[\varepsilon_{ij}\right]\mathbf{E}$ and $\mathbf{B} = \mathbf{H}$, Eq. (A.25) confines the sum of energies inside W_{em}^{I} and outside W_{em}^{II} the resonator. Energies of the HE - mode field inside and outside the resonator are equal:

$$W_{em}^{I\,HE} = \frac{1}{8\pi}\int_0^{r_0}\int_0^{2\pi}\int_0^{h} I_I^{HE}(r,\varphi,z) r dr d\varphi dz\,; \tag{A.26}$$

$$W_{em}^{II\,HE} = \frac{1}{8\pi}\int_{r_0}^{\infty}\int_0^{2\pi}\int_0^{h} I_{II}^{HE}(r,\varphi,z) r dr d\varphi dz \tag{A.27}$$

where $I_I^{HE} = \left|D_n\right|^2 \times \left\{ \begin{array}{l} \dfrac{\varepsilon_\perp q_E^2}{q_H^4}\left[\left|J_n^{'}(q_E r)\right|^2 + \dfrac{n^2}{q_E^2 r^2}\left|J_n(q_E r)\right|^2\right]\times \\ \times\left[k_z^2 + q_H^2\cos^2(k_z z)\right] + \varepsilon_z\left|J_n(q_E r)\right|^2\cos^2(k_z z) \end{array}\right\}$

$$I_{II}^{HE} = \left|D_n\right|^2 \frac{\left|J_n(q_E r_0)\right|^2}{\left|H_n^{(1)}(q_0 r_0)\right|^2}\times\left\{\begin{array}{l} \dfrac{1}{q_0^2}\left[\begin{array}{l}\left|H_n^{(1)^*}(q_0 r)\right|^2 + \\ + \dfrac{n^2}{q_o^2 r^2}\left|H_n^{(1)}(q_0 r)\right|^2\end{array}\right]\left[k_z^2 + q_0^2\cos^2(k_z z)\right] + \\ + \left|H_n^{(1)}(q_0 r)\right|^2\cos^2(k_z z)\end{array}\right\}$$

For the EH-mode

$$W_{em}^{I\,EH} = \frac{1}{8\pi}\int_0^{r_0}\int_0^{2\pi}\int_0^{h} I_I^{EH}(r,\varphi,z)\,r\,dr\,d\varphi\,dz; \tag{A.28}$$

$$W_{em}^{II\,EH} = \frac{1}{8\pi}\int_{r_0}^{\infty}\int_0^{2\pi}\int_0^{h} I_{II}^{EH}(r,\varphi,z)\,r\,dr\,d\varphi\,dz \tag{A.29}$$

where

$$I_I^{EH} = \left|C_n\right|^2 \times \left\{ \begin{array}{l} \dfrac{1}{q_H^2}\left[\left|J_n^{'}(q_H r)\right|^2 + \dfrac{n^2}{q_H^2 r^2}\left|J_n(q_H r)\right|^2\right]\times \\ \times\left[k_z^2 + q_H^2\sin^2(k_z z)\right] + \left|J_n(q_H r)\right|^2\sin^2(k_z z) \end{array}\right\}$$

$$I_{II}^{EH} = \left|C_n\right|^2 \frac{\left|J_n(q_H r_0)\right|^2}{\left|H_n^{(1)}(q_0 r_0)\right|^2}\times\left\{\begin{array}{l} \dfrac{1}{q_0^2}\left[\left|H_n^{(1)^*}(q_0 r)\right|^2 + \dfrac{n^2}{q_o^2 r^2}\left|H_n^{(1)}(q_0 r)\right|^2\right]\times \\ \times\left[k_z^2 + q_0^2\sin^2(k_z z)\right] + \left|H_n^{(1)}(q_0 r)\right|^2\sin^2(k_z z)\end{array}\right\}.$$

The relationship between electromagnetic fields, created by HE- and EH- modes outside the resonator, can be expressed in a following form:

$$\frac{W_{em}^{II\,HE}}{W_{em}^{II\,EH}} = \frac{\left|D_n\right|^2}{\left|C_n\right|^2}\frac{\left|J_n(q_E r_0)\right|^2}{\left|J_n(q_H r_0)\right|^2}; \tag{A.30}$$

For the dielectric disk made of an anisotropic crystal, such that, as for most crystals, $\varepsilon_\perp < \varepsilon_z$, when $D_n \approx C_n$, it follows that $W_{em}^{II\,HE}/W_{em}^{II\,EH} < 1$. Therefore, the field energy outside

the dielectric cylinder is lesse for the HE-mode than for EH-mode, which indicates a different efficiency for their excitation. An increase of the relation $\varepsilon_z/\varepsilon_\perp$ enhances this distinction.

After integration along over the space coordinates, the expressions for the stored energy of EH and HE modes one can be brought to the following form:

$$W_{em}^{EH}=\frac{1}{8}\left|C_n\right|^2 r_0^2 l\times\left\{\begin{array}{l}\left(\frac{k_z^2}{q_H^2}+1\right)F_1^H+\frac{1}{2}\left(\frac{2k_z^2}{q_H^2}+1\right)F_2^H-\\ -\frac{\left|J_n(q_H r_0)\right|^2}{\left|H_n^{(1)}(q_0 r_0)\right|^2}\left[\left(\frac{k_z^2}{q_0^2}+1\right)\Phi_1+\frac{1}{2}\left(\frac{2k_z^2}{q_0^2}+1\right)\Phi_2\right]\end{array}\right\},$$

$$W_{em}^{HE}=\frac{1}{8}\left|D_n\right|^2 r_0^2 l\times\left\{\begin{array}{l}\varepsilon_z\left[\left(\frac{k_z^2}{q_H^2}+1\right)F_1^E+\frac{1}{2}\left(\frac{2k_z^2}{q_H^2}+1\right)F_2^E\right]-\\ -\frac{\left|J_n(q_E r_0)\right|^2}{\left|H_n^{(1)}(q_0 r_0)\right|^2}\left[\left(\frac{k_z^2}{q_0^2}+1\right)\Phi_1+\frac{1}{2}\left(\frac{2k_z^2}{q_0^2}+1\right)\Phi_2\right]\end{array}\right\},$$

where $F_1^{E(H)}=\left(1-\frac{n^2}{q_{E(H)}^2 r_0^2}\right)\left|J_n(q_{E(H)}r_0)\right|^2+\left|J_n^*(q_{E(H)}r_0)\right|^2;$

$$F_2^{E(H)}=\frac{1}{q_{E(H)}r_0}\left(\begin{array}{l}J_n(q_{E(H)}r_0)J_n^{'*}(q_{E(H)}r_0)+\\ +J_n^{*}(q_{E(H)}r_0)J_n^{'}(q_{E(H)}r_0)\end{array}\right);$$

$$\Phi_1=\left(1-\frac{n^2}{q_0^2 r_0^2}\right)\left|H_n^{(1)}(q_0 r_0)\right|^2+\left|H_n^{(1)*}(q_0 r_0)\right|^2;$$

$$\Phi_2=\frac{1}{q_0 r_0}\left(\begin{array}{l}H_n^{(1)}(q_0 r_0)H_n^{(1)'*}(q_0 r_0)+\\ +H_n^{(1)*}(q_0 r_0)H_n^{(1)'}(q_0 r_0)\end{array}\right);$$

The sign "*" indicates the complex conjugate quantity.

As it is known, there exist three sources of losses in the resonator: Joule heat, induced from the conducting plates, losses in the dielectric cylinder and radiation losses (Eq. (3.1) – Chapter 3). When the conductor has a certain (non-zero) value of the microwave conductivity, and therefore a certain value of the surface resistance R_S, than the Joule heat in the two end surfaces (z=0; z=h) averaged in time are defined as following:

$$P_c = \frac{c^2}{16\pi^2} R_s \left(\int\limits_{S_1} \left|H_{\tau 1}\right|^2 ds + \int\limits_{S_2} \left|H_{\tau 2}\right|^2 ds \right) \tag{A.31}$$

where $H_{\tau 1(\tau 2)}$ are the tangential components of magnetic field to conducting surfaces S_1 at $r \le r_0$, and S_2 at $r > r_0$. Correspondingly, for the HE and EH modes Eq. (A.31) can be converted into:

$$P_c^{HE} = \frac{1}{8\pi}\left|D_n\right|^2 c^2 R_s k_0^2 \times \left(\begin{array}{l} \dfrac{\varepsilon_z \varepsilon_\perp}{q_H^2} \int\limits_0^{r_0} I_E(q_E r) r dr + \dfrac{1}{q_0^2} \dfrac{\left|J_n(q_E r_0)\right|^2}{\left|H_n^{(1)}(q_0 r_0)\right|^2} \times \\ \times \int\limits_{r_0}^{\infty} I(q_0 r) r dr \end{array} \right); \tag{A.32}$$

$$P_c^{EH} = \frac{1}{8\pi}\left|C_n\right|^2 c^2 R_s k_z^2 \times \left(\begin{array}{l} \dfrac{1}{q_H^2} \int\limits_0^{r_0} I_H(q_H r) r dr + \dfrac{1}{q_0^2} \dfrac{\left|J_n(q_H r_0)\right|^2}{\left|H_n^{(1)}(q_0 r_0)\right|^2} \times \\ \times \int\limits_{r_0}^{\infty} I(q_0 r) r dr \end{array} \right), \tag{A.33}$$

where $I_E(q_E r) = \dfrac{n^2}{q_E^2 r^2}\left|J_n(q_E r)\right|^2 + \left|J_n^*(q_E r)\right|^2$;

$I_H(q_H r) = \dfrac{n^2}{q_H^2 r^2}\left|J_n(q_H r)\right|^2 + \left|J_n^*(q_H r)\right|^2$;

$I(q_0 r) = \dfrac{n^2}{q_0^2 r^2}\left|H_n^{(1)}(q_0 r)\right|^2 + \left|H_n^{(1)^*}(q_0 r)\right|^2$.

Equations (A.32) and (A.33) after integration become

$$P_c^{HE} = \frac{1}{16\pi}\left|D_n\right|^2 R_s c^2 r_0^2 \frac{k_0^2}{q_H^2} \times \left[\varepsilon_\perp \varepsilon_z \left(F_1^E + F_2^E \right) - \frac{q_H^2}{q_0^2} \frac{\left|J_n(q_E r_0)\right|^2}{\left|H_n^{(1)}(q_0 r_0)\right|^2} \left(\Phi_1 + \Phi_2 \right) \right],$$

$$P_c^{EH} = \frac{1}{16\pi}\left|C_n\right|^2 R_s c^2 r_0^2 \frac{k_z^2}{q_H^2} \times \left[F_1^H + F_2^H - \frac{q_H^2}{q_0^2} \frac{\left|J_n(q_H r_0)\right|^2}{\left|H_n^{(1)}(q_0 r_0)\right|^2} \left(\Phi_1 + \Phi_2 \right) \right].$$

According to definition of resonant system quality factor:

$$Q_c = \frac{\omega W_{em}}{P_c}. \tag{A.34}$$

On the basis of (A.34), the *Q*-factor of the resonator Q_c for HE- and EH- modes can be written as

$$Q_c^{HE} = \frac{2\pi}{c}\frac{k_0 \cdot h \cdot R_E}{R_s}; \tag{A.35}$$

$$Q_c^{EH} = \frac{2\pi}{c}\frac{k_0 \cdot h \cdot R_H}{R_s} \tag{A.36}$$

where

$$R_H = 1 + \frac{F_1^H + \frac{1}{2}F_2^H - \frac{\left|J_n(q_H r_0)\right|^2}{\left|H_n^{(1)}(q_0 r_0)\right|^2}\left(\Phi_1 + \frac{1}{2}\Phi_2\right)}{\frac{k_z^2}{q_H^2}\left(F_1^H + F_2^H\right) - \frac{k_z^2}{q_0^2}\frac{\left|J_n(q_H r_0)\right|^2}{\left|H_n^{(1)}(q_0 r_0)\right|^2}\left(\Phi_1 + \Phi_2\right)};$$

$$R_E = \frac{F^E - \frac{\left|J_n(q_E r_0)\right|^2}{\left|H_n^{(1)}(q_0 r_0)\right|^2}\left[\left(\frac{k_z^2}{q_H^2}+1\right)\Phi_1 + \frac{1}{2}\left(\frac{2k_z^2}{q_H^2}+1\right)\Phi_2\right]}{\varepsilon_\perp \varepsilon_z \frac{k_0^2}{q_H^2}\left(F_1^E + F_2^E\right) - \frac{k_0^2}{q_H^2}\frac{\left|J_n(q_E r_0)\right|^2}{\left|H_n^{(1)}(q_0 r_0)\right|^2}\left(\Phi_1 + \Phi_2\right)}$$

$$F^E = \varepsilon_z\left[\left(\frac{k_z^2}{q_H^2}+1\right)F_1^E + \frac{1}{2}\left(\frac{2k_z^2}{q_H^2}+1\right)F_2^E\right].$$

The losses in the dielectric resonator material are defined by the power $P_d = \omega W_{em}^I \mathrm{tg}\delta$, which can help to calculate Q_d, analogically to Eq.(A.34)

$$Q_d = \frac{1}{\mathrm{tg}\delta}\frac{W_{em}}{W_{em}^I}. \tag{A.37}$$

According (A.37). the quality factor Q_d for HE - and EH - modes is defined by the expressions:

$$Q_d^{HE} = \frac{1}{\mathrm{tg}\delta}\left(1\text{-}R_0^E\right), \tag{A.38}$$

$$Q_d^{EH} = \frac{1}{\mathrm{tg}\delta}\left(1\text{-}R_0^H\right) \tag{A.39}$$

in which

$$R_0^H = \frac{\left|J_n(q_H r_0)\right|^2}{\left|H_n^{(1)}(q_0 r_0)\right|^2} \times \frac{\left(\frac{k_z^2}{q_0^2}+1\right)\Phi_1(q_0 r_0)+\frac{1}{2}\left(\frac{2k_z^2}{q_0^2}+1\right)\Phi_2(q_0 r_0)}{\left(\frac{k_z^2}{q_H^2}+1\right)F_1(q_H r_0)+\frac{1}{2}\left(\frac{2k_z^2}{q_H^2}+1\right)F_2(q_H r_0)} \; ;$$

$$R_0^E = \frac{1}{\varepsilon_z}\frac{\left|J_n(q_E r_0)\right|^2}{\left|H_n^{(1)}(q_0 r_0)\right|^2} \times \frac{\left(\frac{k_z^2}{q_0^2}+1\right)\Phi_1(q_0 r_0)+\frac{1}{2}\left(\frac{2k_z^2}{q_0^2}+1\right)\Phi_2(q_0 r_0)}{\left(\frac{k_z^2}{q_H^2}+1\right)F_1(q_E r_0)+\frac{1}{2}\left(\frac{2k_z^2}{q_H^2}+1\right)F_2(q_E r_0)} \; .$$

The eigen Q-factor of WGMR with the conducting endplates can be defined with the expression

$$\frac{1}{Q_0} = \frac{1}{Q_c} + \frac{1}{Q_d}, \tag{A.40}$$

where Q_c and Q_d can be calculated with the Eq. (A.35), (A.36), (A.38) and (A.39). The expression (A.40) is written without considering radiation losses. They can be neglected only in the case when the diameter of the conducting plates is much larger than r_0 (diameter of the dielectric disk). Expression for the eigen Q-factor in the case HE- and EH- modes one can write:

$$Q_0^{HE\,(EH)} = \frac{2\pi k_0 h R_{E\,(H)}\left(1\text{-}R_0^{E\,(H)}\right)}{cR_s\left(1\text{-}R_0^{E\,(H)}\right)+2\pi k_0 h R_{E\,(H)}\mathrm{tg}\delta} \tag{A.41}$$

Appendix B: Theoretical electrodynamics of radially two-layered WGMR with CEP

Consider a two-layered (along radius) WGMR with CEP in which the layers are made of different uniaxial single crystals with axes of anisotropy directed in parallel with the resonator longitudinal axis (Fig. 3.17(b)). In this case, the tensors of dielectric and magnetic permittivity are as follows

$$[\varepsilon_{ij}]=\begin{cases}\begin{pmatrix}\varepsilon_{\perp\nu} & 0 & 0\\ 0 & \varepsilon_{\perp\nu} & 0\\ 0 & 0 & \varepsilon_{\parallel\nu}\end{pmatrix}, & \nu=1, \quad r\le r_1\\ , & \nu=2,\ r_1<r\le r_2\\ \delta_{ij}, & \nu=3, \quad r>r_2\end{cases}, \qquad \mu_\nu=\begin{cases}\mu_1, & \nu=1, \quad r\le r_1\\ \mu_2, & \nu=2,\ r_1<r\le r_2\\ 1, & \nu=3, \quad r>r_2\end{cases}, \tag{B.1}$$

where $\varepsilon_{\parallel\nu}$ and $\varepsilon_{\perp\nu}$ are the components of [εij] in parallel and perpendicular directions to optical axis of crystal for ν-layer; r_1 and r_2 are the radii of resonator layers; δ_{ij} is the Kronecker delta.

The modes in such a resonator are described by solutions of a set of Maxwell's equations that satisfy the following conditions:

(i) the tangential components of electromagnetic field strengths on the medium boundaries $r = r_1$ and $r = r_2$ are continuous;

(ii) the tangential components of electrical fields are equal to zero on the resonator ideally CEP;

(iii) the electromagnetic fields are finite at $r = 0$; (iv) the fields go to zero for $r \to \infty$.

The axial components of electromagnetic fields in the radially two-layered QDR have the forms

$$E_{z\nu}=G_{E\nu}(r)\cos(k_z z)\mathrm{e}^{\mathrm{i}(n\varphi-\omega t)}; \qquad H_{z\nu}=G_{H\nu}(r)\sin(k_z z)\mathrm{e}^{\mathrm{i}(n\varphi-\omega t)}, \tag{B.2}$$

where $G_{j\nu}=\begin{cases}A_{jn}J_n(q_{j1}r), & r\le r_1\\ B_{jn}J_n(q_{j2}r)+C_{jn}N_n(q_{j2}r), & r_1\le r\le r_2\\ D_{jn}H_n^{(1)}(q_0 r), & r\ge r_2\end{cases}$ characterizes the distribution of the field for the ν-th resonator layer along a radius. Here A_{jn}, B_{jn}, C_{jn}, D_{jn} are constants determined by the above-mentioned boundary and excitation conditions of electromagnetic modes in the QDR; the index j accepts a value E or H; $J_n(z)$, $N_n(z)$, $H_n^{(1)}(z)$ are the Bessel, Neumann and first kind Hankel cylindrical functions; $n = 0; 1; 2;\ldots$ is the azimuth wave number; $\omega = \omega' - \mathrm{i}\omega''$ is the complex cyclical frequency. The radial ($q_{j\nu}$ is for inside dielectric layers and q_0 is

for outside of dielectrics) and axial k_z components of wave number for the QDR fields are of the form

$$q_{H\nu}^2 = \mu_\nu \varepsilon_{\perp\nu} k_0^2 - k_z^2; \qquad q_{E\nu}^2 = \frac{\varepsilon_{\parallel\nu}}{\varepsilon_{\perp\nu}} q_{H\nu}^2; \qquad q_0^2 = k_0^2 - k_z^2; \qquad k_z = \frac{m\pi}{l}, \tag{B.3}$$

where $k_0 = \omega / c$, c is a light velocity; $m = 0; 1; 2;\ldots$ is the axial index.

The transversal components of electromagnetic field are expressed through $E_{z\nu}$ and $H_{z\nu}$:

$$q^2 E_{\varphi\nu} = \frac{1}{r}\frac{\partial}{\partial\varphi}\frac{\partial}{\partial z} E_{z\nu} - \mathrm{i}\mu_\nu \omega \frac{\partial}{\partial r} H_{z\nu}; \qquad q^2 E_{r\nu} = \frac{\partial}{\partial r}\frac{\partial}{\partial z} E_{z\nu} + \mathrm{i}\mu_\nu \frac{\omega}{r}\frac{\partial}{\partial\varphi} H_{z\nu}; \tag{B.4}$$

$$q^2 H_{\varphi\nu} = \mathrm{i}\varepsilon_{\perp\nu}\omega \frac{\partial}{\partial r} E_{z\nu} + \frac{1}{r}\frac{\partial}{\partial\varphi}\frac{\partial}{\partial z} H_{z\nu}; \quad q^2 H_{r\nu} = \frac{\partial}{\partial r}\frac{\partial}{\partial z} H_{z\nu} - \mathrm{i}\varepsilon_{\perp\nu}\frac{\omega}{r}\frac{\partial}{\partial\varphi} E_{z\nu}, \tag{B.5}$$

where $q^2 = q_{H\nu}^2$ at ν = 1;2 and $q^2 = q_0^2$ at ν = 3.

The spectral characteristics of anisotropic radially two-layered resonator are determined by solutions of the following dispersion equation:

$$\begin{aligned} &\chi_0\chi\left(\gamma_\beta^E - \gamma_\alpha^E\right)\left(\vartheta_\alpha^H - \vartheta_\beta^H\right) Z_J^H Z_N^H + \left(\chi_0^2 - \gamma_\beta^E\gamma_\beta^H\right)\left(\vartheta_\alpha^E\vartheta_\alpha^H - \chi^2\right) Z_J^E Z_J^H \\ &+ \left(\chi_0^2 - \gamma_\alpha^E\gamma_\alpha^H\right)\left(\vartheta_\beta^E\vartheta_\beta^H - \chi^2\right) Z_N^E Z_N^H + \chi_0\chi\left(\vartheta_\beta^E - \vartheta_\alpha^E\right)\left(\gamma_\alpha^H - \gamma_\beta^H\right) Z_J^E Z_N^E \\ &+ \left(\chi_0^2 - \gamma_\alpha^E\gamma_\beta^H\right)\left(\chi^2 - \vartheta_\beta^E\vartheta_\alpha^H\right) Z_N^E Z_J^H + \left(\chi_0^2 - \gamma_\beta^E\gamma_\alpha^H\right)\left(\chi^2 - \vartheta_\alpha^E\vartheta_\beta^H\right) Z_J^E Z_N^H = 0. \end{aligned} \tag{B.6}$$

In this equation the notations are: $\chi_0 = nk_z\left(q_0^{-2} - q_{H2}^{-2}\right)/k_0 r_2^2$, $\chi = nk_z\left(q_{H1}^{-2} - q_{H2}^{-2}\right)/k_0 r_1^2$; $\vartheta_\xi^j = \sigma_2^j \xi_{21}^j - \sigma_1^j \alpha_{11}^j$; $\gamma_\xi^j = \sigma_2^j \xi_{22}^j - \alpha_0$, where ξ accepts a value α or β; $\sigma_\nu^j = \varepsilon_{z\nu}$ at $j = E$ and $\sigma_\nu^j = \mu_\nu$ at $j = H$; $\alpha_{p\nu}^j = \frac{1}{q_{jp} r_\nu}\frac{J_n'(q_{jp} r_\nu)}{J_n(q_{jp} r_\nu)}$, where $p = 1, 2$; $\alpha_0 = \frac{1}{q_0 r_2}\frac{H_n^{(1)\prime}(q_0 r_2)}{H_n^{(1)}(q_0 r_2)}$; $\beta_{2\nu}^j = \frac{1}{q_{j2} r_\nu}\frac{N_n'(q_{j2} r_\nu)}{N_n(q_{j2} r_\nu)}$, the prime denotes derivative with respect to the argument; $Z_R^j = \frac{R_n(q_{j2} r_1)}{R_n(q_{j2} r_2)}$, where R is the J or N.

There are independent EH and HE modes in the resonator outside of the frequency degeneration area. In the case when the following condition

$$\frac{\left|\chi^2\left(Z_J^E - Z_N^E\right)\left(\gamma_\beta^H Z_J^H - \gamma_\alpha^H Z_N^H\right) + \left(\vartheta_\alpha^E Z_J^E - \vartheta_\beta^E Z_N^E\right)\left(\gamma_\alpha^H \vartheta_\beta^H Z_N^H - \gamma_\beta^H \vartheta_\alpha^H Z_J^H\right)\right|}{\left|\chi_0\left[\left(\vartheta_\alpha^H Z_J^H - \vartheta_\beta^H Z_N^H\right)\left(\vartheta_\beta^E Z_N^E - \vartheta_\alpha^E Z_J^E\right) + \chi^2\left(Z_J^H - Z_N^H\right)\left(Z_J^E - Z_N^E\right)\right] + \chi\left(\vartheta_\alpha^E - \vartheta_\beta^E\right)\left(\gamma_\alpha^H - \gamma_\beta^H\right) Z_J^E Z_N^E\right|} \tag{B.7}$$

is realized, HE modes occur and otherwise EH modes.

The *Q*-factor of a resonator with eigen-modes is given by the expression $Q = \omega / \omega'$.

Acknowledgements

At first, I like to thank my supervisor **Dr. Norbert Klein** for many scientific discussions we had about strategy and results of this thesis, and for his contribution to develop perturbation theory describing the experimental results with nanolitre samples.

During my work in the laboratory, the help and support of my Ukrainian college **Dr. Alexander Barannik**, Institute of Radiophysics and Electronics, Kharkov (IRE), who stayed for a few months at Forschungszentrum Jülich in the framework of INTAS grants, is highly appreciated.

For scientific discussion I would like to express my thanks to **Dr. Svetlana Vitusevich** from our group at Forschungszentrum Jülich and to **Professor Nickolay Cherpak** at IRE.

The technical support in conjunction with the micropipette spotting system by **Dr. Sven Ingebrandt**, in particular software and hardware adjustments performed by **DI Dieter Lomparski**, is greatly acknowledged.

For scientific discussion and for giving useful advices for work in the biochemical laboratory I would like to thank my colleges from IBN2-BE, FZ Jülich **Dr. Ranjita Ghosh-Moulick**, and **MSc. Xuan-Thang Vu**.

I would like to acknowledge the help of my colleagues **Dr. Serhiy Danylyuk** and **MSc. Viktor Sidoryuk**.

Finally, I like to express my thanks to our director **Prof. Andreas Offenhäusser**, who gave me the opportunity to perform my thesis in the Institute for Bio-and Nanosystems (IBN 2) at Forschungszentrum Jülich, for his support and concern.

Personal publication list

1. E. Shaforost, A. Barannik, and N. Klein “Whispering-gallery mode resonators for liquid droplet detection”, MSMW’07 Symposium Proceedings, Kharkov, Ukraine, June 25-30, 2007, pp. 919-921.

2. A.A Barannik, N.T. Cherpak, Yu.V. Prokopenko, Yu.F. Filipov, E.N. Shaforost, and I.A. Shipilova, “Two-layered disc quasi-optical dielectric resonators: Electrodynamics and applied perspectives for complex permittivity measurement of lossy liquids”, *Meas. Sci. Technol.*, vol. 18, N7, July, 2007, pp. 2231-2238.

3. E.N. Shaforost, A.A. Barannik, S. Vitusevich, and A. Offenhaeusser “Open WGM dielectric resonator technique for characterization of nL-volume liquids”, *Proceedings of the 38th European Microwave Conference*, EuMC-2008, Amsterdam, 27-31 October, 2008, pp. 1129–1132.

4. E.N. Shaforost, A.A. Barannik, N. Klein, S.A. Vitusevich, A. Offenhaeusser “Nanolitre liquid characterization by open whispering-gallery mode dielectric resonators at

millimeter wave frequencies", *Journal of Applied Physics*, vol. 104, 2008, art. no. 074111, 7 pages.

5. E.N. Shaforost, A.A. Barannik, N. Klein, S.A. Vitusevich, and A. Offenhaeusser "Nanolitre liquid characterization by open whispering-gallery mode dielectric resonators at millimeter wave frequencies", *Virtual Journal of Biological Physics Research*, vol. 16, N8, Oct 15, 2008, 7 pages.

6. E.N. Shaforost, N. Klein, A.A. Barannik, S.A. Vitusevich, and N.T. Cherpak "High-sensitivity microwave characterisation of organic molecule solutions of nanolitre volume", *Appl. Phys. Lett*., vol. 94, 2009, art. no. 112901, 3 pages.

Bibliography

1. Y. Ozaki, A.A. Christy, and W. F. McClure, “Near infrared spectroscopy in food science and technology,” *John Wiley,* 2006

2. B. Schrader, “Infrared and Raman spectroscopy”, *John Wiley*, 1995

3. M. Dressel, and G. Gruner, “Electrodynamics of Solids”, *Cambridge University Press*, 2002

4. D. Mittleman, “Sensing with Terahertz Radiation”, *Springer*, 2007

5. F. Kremer, and A. Schönhals, “Broadband dielectric spectroscopy”, *Springer, Berlin*, 2002

6. J.B. Hasted, “Aqueous Dielectrics”, *London: Chapman and Hall*, 1973

7. W.J. Ellison, K. Lamkaouchi, and J.M. Moreau, “Water: A dielectric reference”, *Journal of Molecular Liquids*, 1996, vol. 68, issue: 2-3, pp. 171-279

8. U. Kaatze, “Reference liquids for the calibration of dielectric sensors and measurement instruments”, *Meas. Sci. Technol.*, 2007, vol. 18, issue: 4, pp. 967-976

9. N. Klein, “Electrodynamic Properties of Oxide Superconductors”, Habilitationschrift, Forschungszentrum Jülich, *Jülich Report* 3773, 1997.

10. J. M. G. Barthel, H. Krienke, and W. Kunz, “Physical chemistry of electrolyte solutions”, *Darmstadt : Steinkopff*, 1998

11. A.V. Hippel, “Dielectric material and applications”, *New York: John Wiley & Sons*, 1961

12. P. Debye, “Polar molecules”, *New York, NY: Dover Publ.*, 1929

13. J. Barthel and R. Buchner, “High frequency permittivity and its use in the investigation of solution properties”, Pure&Appl.Chem., 1991, vol. 63, issue: 10, pp. 1473-1482

14. U. Kaatze, “The dielectric properties of water in its different states of interaction”, *J. Solut. Chem.*, 1997, vol. 26, issue: 11, pp. 1049–1212

15. W.J. Ellison, “Permittivity of pure water, at Standard Atmospheric pressure, over the frequency range 0-25 THz and the temperature range 0-100° C”, *J. Phys. Chem. Data*, 2007, vol. 36, issue: 1, pp. 1-18

16. U. Kaatze, “The dielectric spectrum of water in the microwave and near-millimeterwave wavelength region”, *Chem. Phys. Lett.*, 1986, vol. 132, issue: 3, pp. 291-293

17. P.S. Ray, “Broadband Complex Refractive Indices of Ice and Water”, *Appl. Opt.*, 1972, vol. 11, issue: 8, pp. 1836-1844

18. H.J. Liebe, G.A. Hufford, and T. Manabe, “A model for the complex permittivity of water at frequencies below 1 THz”, *Int. J. Infrared Millim. Waves*, 1991, vol. 12, issue: 7, pp. 659-675

19. R. Buchner, J. Barthel, and J. Stauber, “The dielectric relaxation of water between 0°C and 35°C”, *Chem. Phys. Lett.*, 1999, vol. 306, issue: 1-2, pp. 57-63

20. G. H. Haggis, J.B. Hasted, and T.J. Buchanan, “The dielectric properties of water in solutions” *J. Chem. Phys.*, 1952, vol. 20, issue: 9, pp. 1452-1465

21. J. Baker-Jarvis, M. D. Janezic, J. S. Grosvenor, and R. G. Geyer, “Transmission/Reflection and Short-Circuit Methods for Measuring Permitivity and Permeability”, *NIST Technical Note* 1355-R, December 1993

22. M. Afsar, J.B. Birch, R.N. Clarke, and Ed. G.W. Chantry; “Measurement of the Properties of Materials”, *Proc. IEEE*, 1986, vol. 74, issue: 1, pp. 183-199

23. http://cp.literature.agilent.com/litweb/pdf/5989-2589EN.pdf, “Basics of measuring dielectric properties of materials”, *Agilent Application Note* 5989-2589EN, 2005

24. M.N. Afsar, N. Suwanvisan, and Y. Wang, “Permittivity Measurements of low and high loss liquids in the frequency range of 8-40 GHz using waveguide transmission line technique”, *Microwave and Opt. Tech. Lett.*, 2006, vol. 48, issue: 2, pp. 275-281

25. R. Nozaki, and T.K. Bose, “Broadband complex permittivity measurements by time domain spectroscopy”, *IEEE Trans. Instrum. Meas.*, 1990, vol. 39, issue: 6, pp. 945-951

26. Y.Z. Wei, and S. Sridhar, “Radiation-corrected open-ended coax line technique for dielectric measurements of liquids up to 20 GHz”, IEEE Trans. Microwave Theory.Techn, 1991, vol. 39, issue: 3, pp. 526-531

27. D. V. Blackham, and R. D. Pollard, “An Improved Technique for Permittivity Measurements Using a Coaxial Probe”, *IEEE Trans. on Instr. Meas.*, 1997, vol. 46, issue: 5, pp. 1093-1099

28. K. Murata, A. Hawana, and R. Nozaki, “Broadband complex permittivity measurement techniques of materials with thin configuration at microwave frequencies”, *J. Appl. Phys.*, 2005, vol. 98, issue: 8, art. no. 084107

29. Mingzhong Wu, Xi Yao, and Liangying Zhang, “An improved coaxial probe technique for measuring microwave permittivity of thin dielectric materials”, *Meas. Sci. Technol.*, 2000, vol. 11, issue: 11, pp. 1617-1622

30. D. Pozar, “Microwave Engineering”, *John Wiley*, 2005

31. A.P. Gibson, K.N. Sing, B.M. Badaruzzaman, H.S. Chua, A.D. Haig, G. Parkinson, P. Ainsworth, and A. Plunkett, “An overview of microwave techniques for the efficient

measurements of food materials", *Food Manufacturing Efficiency*, 2008, vol 2, issue: 1, pp. 1-8

32. V.V. Varadan, R.D. Hollinger, D.K. Ghodgaonkar, and V.K. Varadan, "Free-space, broadband measurements of high-temperature, complex dielectric properties at microwave frequencies", "Free-space, broadband measurements of high-temperature, complex dielectric properties at microwave frequencies", *IEEE Transactions on Instrumentation and Measurement*, 1991, vol. 40, issue: 5, pp. 842-846

33. R.A. Waldron, "Perturbation theory of resonant cavities", *The Institution of Electrical Engineers (London)*, 1960

34. R.A. Waldron, "The theory of waveguides and cavities", *London, U.K.: Maclaren and Sons*, 1967

35. A. Parkash, J.K. Vaid, and A. Mansingh, "Measurement of dielectric parameters at microwave frequencies by cavity perturbation technique", *IEEE Trans. Microwave Theory Techn.*, 1979, vol. MTT-27, issue: 9, pp. 791-795

36. L.G. Matus, C.B. Boss, and A.N. Riddle, "Tuning and matching the TM_{010} cavity", *Rev. Sci. Instrum.*, 1983, vol. 54, issue: 12, pp. 1667-1673

37. K.H. Hong and J.A. Roberts, "Microwave properties of liquids and solids using a resonant microwave cavity as a probe", *J. Appl. Phys.*, 1974, vol. 45, issue: 6, pp. 2452-2456

38. R.J. Cook, "Microwave cavity methods", in *High Frequency Dielectric Measurement* (*Conf. Proc.*, March 1972); J. Chamberlain, and G.W. Chantry, Eds. Guildford, U.K.: *IPC Science and Technology Press*, 1973, pp. 12-27

39. E. Ni and U. Stumper, "Permittivity measurements using a frequency tuned microwave TE_{01} cavity resonator", *Proc. Inst. Elec. Eng.*, pt. H, 1985, vol. 132, issue: 1, pp. 27-32

40. C.B. Rosenberg, N.A. Hermitz, and R.J. Cook, "Cavity resonator measurements of the complex permittivity of low-loss liquids", *Proc. Inst. Elec. Eng.*, pt. H, 1982, vol. 129, issue: 2, pp. 71-76

41. A-J. Berteaud, F. Hoffman, and J-F. Mayault, "Complex frequency perturbation of a microwave cavity containing a lossy liquid", *J. Microwave Power*, 1975, vol. 10, issue: 4, pp. 309-313

42. A. Sen, P.K. Saha, and B.R. Nag, "New cavity perturbation technique for the measurement of dielectric constant", *Rev. Sci. Instrum.*, 1979, vol. 50, issue: 12, pp. 1594-1597

43. M. Stockhausen, and M. Kessler, "Concerning measurements of high complex permittivity by the resonator perturbation method", *J. Phys.E: Sci.Instrum.*, 1980, vol. 13, issue: 7, pp. 732-736

44. S. Li, C. Akyel, and R.G. Bosisio, "Precise calculations and measurements on the complex dielectric constant of lossy materials using TM_{010} cavity perturbation techniques", *IEEE Trans. Microwave Theory Tech.*, 1981, vol. MTT-29, issue: 10, pp. 1041-1048

45. R.N. Clarke, and C.B. Rosenberg, "Fabry-Perot and open resonators at microwave and millimeter wave frequencies, 2-300 GHz," *J.Phys. E: Sci. Instrum.*, 1982, vol. 15, issue: 1, pp. 9-24

46. A.C. Lynch, "Measurement of permittivity by means of an open resonator II. Experimental", *Proc.Roy.Soc., Lond. A*, 1982, vol. 380, issue: 1778, pp.73-76.

47. A.L. Cullen, and P.K. Yu, "The accurate measurement of permittivity by means of an open resonator,"*Proc. Roy. Soc. Lond. A*, 1971, vol. 325, issue: 1563, pp. 493-509

48. R.W. Boyd, and J.E. Heebner, "Sensitive disk resonator photonic biosensor", *Appl.Opt.*, 2001, vol. 40, issue: 31, pp. 5742-5747

49. S. Arnold, M. Khoshima, I. Teraoka, S. Holler, and F. Vollmer, "Shift of the whispering-gallery modes in microspheres by protein adsorption", *Opt.Lett.*, 2003, vol. 28, issue: 4, pp. 272-275

50. Ch.Y. Chao, and L.J. Guo, "Biochemical sensors based on polymer microrings with sharp asymmetrical resonance", *Appl. Phys. Lett.*, 2003, vol 83, issue: 9, pp. 1527-1529

51. A.N. Oraevsky, "Review: Whispering-gallery waves", *Quantum Electronics*, 2002, vol. 32, issue: 5, pp. 377-400

52. Y. Kobayashi, N. Fukuoka, and S. Yoshida, "Resonant modes in a shielded dielectric rod resonator", *Electronics & Communications in Japan*, 1981, vol. 64-B, issue: 11, pp. 44-51

53. P. Guillon, and Y. Garault, "Accurate resonant frequencies of dielectric resonators", *IEEE Trans. on Micr. Theo. and Tech.*, Nov. 1977, vol. MTT-25, issue: 11, pp.916-922

54. C. Zuccaro, M. Winter, N. Klein**,** and K. Urban, "Microwave absorption in single crystals of lanthanum aluminate", *Journal of Applied Physics*, 1997, vol. 82, issue: 11, pp. 5695-704

55. N. Klein**,** C. Zuccaro**,** U. Dähne, H. Schulz, N. Tellmann, R. Kutzner, A.G. Zaitsev, and R. Wördenweber, "Dielectric properties of rutile and its use in high temperature superconducting resonators", *Journal of Applied Physics*, 1995, vol. 78, issue: 11, pp. 6683-6686

56. J.G. Hartnett, M.E. Tobar, E.N. Ivanov, and J. Krupka, "Room temperature measurement of the anisotropic loss tangent of sapphire using the whispering gallery mode technique", *IEEE Transactions on Ultrasonics, Ferroelectrics and Frequency Control*, 2006, vol. 53, issue: 1, pp. 34-38

57. C. Vedrenne, and J. Arnaud, "Whispering-Gallery Modes in Dielectric Resonators", *Proc. Inst. Elec. Eng., pt.H*, 1982, vol. 129, issue: 4, pp. 183-187

58. N. Klein, "Microwave Communication Systems: Novel Approaches for Passive Devices" in "*Nanoelectronics and Information Technology*", ed. by R. Waser, *Wiley*, 2003

59. S. A. Vitusevich, K. Schieber, I. S. Ghosh , N. Klein, and M. Spinnler, "Design and characterization of an all-cryogenic low phase-noise sapphire K-band oscillator for satellite communication", *IEEE Trans. Micr. Theor. Tech*, 2003, vol. 51, issue: 1, pp. 163-169

60. D. Cros, and P. Guillon, "Whispering gallery dielectric resonator modes for W-band devices", *IEEE Trans. Microwave Theory Tech.*, 1990, vol. 38, issue: 11, pp. 1667-1674

61. N. Klein, U. Dähne, U.Poppe, N. Tellmann, K. Urban, S. Orbach, S. Hensen, G. Müller, and H. Piel, "Microwave surface resistance of epitaxial $YBa_2Cu_3O_{7-x}$ thin films measured at 18.7 GHz by a dielectric resonator technique", *Journal of Superconductivity*, 1992, vol. 5, issue: 2, pp. 195-201

62. N.T. Cherpak, A.A. Barannik, Yu.V. Prokopenko, Yu.F. Filipov, and S. Vitusevich, "Accurate Microwave Technique of Surface Resistance Measurement of Large-area HTS Films using Sapphire Quasioptical Resonator", *IEEE Trans. on Appl. Supercond.*, 2003, vol. 13, issue: 2, pp. 3570-3573

63. J. Krupka, K. Derzakovski, A. Abramovich, M.E. Tobar, and R.G. Geyer, "Use of whispering-gallery modes for complex permittivity determinations of ultra-low-loss dielectric materials", *IEEE Trans. Micr. Theor. Techn.*, 1999, vol. 47, issue: 1, pp. 752-759

64. R.G. Geyer, J. Krupka, and M. Tobar, "Microwave dielectric properties of low-loss materials at low temperature", *Ceramic Transactions*, 2000, vol. 103, pp. 216-229

65. J. Krupka and G. Annino, "WGM in rutile resonator in mm frequencies", *Proc. of 13th International Conference on Microwaves, Radar and Wireless Communications* **(**MICON 2000), 2000, vol. 1-2, pp. 41-44

66. G. Annino G., M. Cassettari, M. Fittipadi, I. Longo, M. Martinelli, C. A. Massa, and L. A. Pardi, "High field, multifrequency EPR spectroscopy using whispering gallery dielectric resonators", *J. Magn. Reson*, 2000, vol. 143, issue: 1, pp. 88-94

67. G. Annino, D. Bertolini, M. Cassetary, M. Fittipabli, I. Longo, and M. Martinelly, "Dielectric properties of materials using whispering gallery dielectric resonators: Experiments and perspectives of ultra-wideband characterization", *Journal of Chemical Physics*, 2000, vol. 112, issue: 5, pp. 2308-2314

68. A. Ya. Kirichenko, and A.E. Kogut, "The oscillator mode for investigation of dielectric properties of a wide class of liquids in 8-mm wave range", *the 5-th Intern. Kharkov Symp. on Phys. And Enginering, MSMW,Kharkov, Ukraine, June 21-26*, 2004,: Proc. -2., pp.790-792

69. N.T. Cherpak, A.A. Lavrinovich, and E.N. Shaforost, "Quasi-optical dielectric resonators with small cuvette and capillary filled with ethanol-water mixtures", *Int. J. Infr. Millim.Waves*, 2006, vol. 27, issue: 1, pp. 117-135

70. J. A. Stratton, "Electromagnetic theory", *New York, NY: MacGraw Hill*, 1941

71. D. Kajfez, “Dielectric resonators”, *Dedham, MA: Artech House*, 1986

72. E. Shaforost, A. Barannik, and N. Klein, “Whispering-gallery mode resonators for liquid droplet detection”, *MSMW’07 Symposium Proceedings, Kharkov, Ukraine, June 25-30,* 2007, pp.919-921

73. P.J. Petersan, and S.M.Anlage, “Measurement of resonant frequency and quality factor of microwave resonators: Comparison of methods”, *J. Appl. Phys.*, 1998, vol. 84, issue: 6, pp.3392-3402

74. Sh. Shino, and I. Itanami, “Low-loss rectangular dielectric image line for millimeter-wave integrated circuits”, *IEEE Trans. Microwave Theory Techn*., 1978, vol. 26, issue: 10, pp. 747–751

75. R.M. Knox, “Dielectric waveguide microwave integrated circuits—An overview”, *IEEE Trans. Microwave Theory Tech.*, 1976, vol. MTT-24, issue: 11, pp. 806-814

76. R. M. Knox, and P. P. Toulios, “Integrated circuits for the mittirneter through optical frequency range”, *Proc. of Ihe Symp. Submillimeter Waves, New York, NY,* Mar. 1970

77. E.N. Shaforost, A.A. Barannik, S. Vitusevich, and A. Offenhaeusser, “Open WGM dielectric resonator technique for characterization of nL-volume liquids”, *Proceedings of the 38th European Microwave Conference, EuMC-2008, Amsterdam*, Oct. 2008, pp. 1129–1132

78. Yu.V. Prokopenko, Yu.F. Filipov, and N.T. Cherpak, “Quasi-optical dielectric resonator with uniaxial anisotropy and conducting end walls. Field structure and Q-factor”, *Radiofizika i Elektronika (Institute of Radiophysics and Electronics, NAS of Ukraine, Kharkiv),* 1999, vol. 4, issue: 2, pp. 50-54

79. Yu.V. Prokopenko, and Yu.F. Filipov, “Anisotropic disk dielectric resonator with conducting end faces”, *Technical Physics*, 2002, vol. 47, issue: 5, pp. 731-736

80. B.W. Hakki, and P.D. Coleman, “A dielectric resonator method of measuring inductive capacities in the millimeter range”, *IEEE Trans. Microwave Theory Tech.*, 1960, vol. 8, issue: 4, pp. 402-410

81. S. J. Fiedziuszko, and P.D. Heidemann, “Dielectric resonator used as a probe for high Tc superconductor measurements”, IEEE MTT-S International Microwave Symp. Dig., 1989, vol. 2, pp. 555-558

82. A.A.Barannik, T.A. Smirnova, Yu.V.Prokopenko, Yu.F.Filipov, and N.T.Cherpak, “Ring quasioptical dielectric resonator with conducting endplates”, *Radiofizika i Elektronika*, IRE NASU, Kharkiv, 2001, vol.6, issue: 2, pp. 201-205 (in Russian)

83. N.T. Cherpak, A.A. Barannik, Yu.V. Prokopenko, T.A. Smirnova, and Yu.F. Filipov, “A new technique of dielectric characterization of liquids”, in *Nonlinear Dielectric Phenomena in Complex Liquids*, S.J. Rzoska, and V.P. Zhelezny, Ed. The Netherlands: *Kluwer Academic Publishers*, 2004, pp. 63-76

84. S. Mashimo, “Structure of water in pure liquid and biosystems”, *J. Non-Cryst. Solids*, 1994, vol. 172–174, pp. 1117–1120

85. E.H. Grant, R.J. Sheppard, and G.P. South, “Dielectric behavior of biological molecules in solution”, in “Monographs of physical biochemistry”, *Clarendon Press. Oxford University press*, 1978

86. Y. Hayashi, N. Miura, N. Shinyashiki, S. Yagihara, and S.Mashimo, “Globule–coil transition of denaturated globular protein investigated by a microwave dielectric technique” *Biopolymers*, 2000, vol. 54, issue: 6, pp. 388–397

87. U. Kaatze, and Yu. Feldman, “Broadband dielectric spectrometry of liquids and biosystems. Review article”, *Meas. Sci. Technol*., 2006, vol. 17, R17-R35

88. Y. Hayashi, N. Miura, J. Isobe, N. Shinyashiki, and S. Yagihara, “Molecular dynamics of hinge-bending motion of IgG vanishing with hydrolysis by papain”, *Biophys. J.*, 2000, vol. 79, issue: 2, pp. 1023–1029

89. N. Miura, Y. Hayashi, N. Shinyashiki, and S. Mashimo, “Observation of unfreezable water in aqueous solution of globule protein by microwave dielectric measurement”, *Biopolymers*, 1995, vol. 36, issue: 1, pp. 9–16

90. A. Caduff, L. Livshits, Y. Hayashi, and Y. Feldman, “Cell membrane response on D-glucose studied by dielectric spectroscopy. Erythrocyte and ghost suspensions”, *J. Phys. Chem. B*, 2004, vol. 108, issue: 36, pp. 13827–13830.

91. S. Mashimo, S. Kuwabara, S. Yagihara, and K. Higasi, “The dielectric relaxation of mixtures of water and primary alcohol”, *J. Chem. Phys.*, 1989, vol. 90, issue: 6, pp. 3292-3294

92. D. Bertolini, M. Cessettari, and G. Salvetti, “The dielectric properties of alcohol water solutions, 1. the alcohol rich region”, *J. Chem. Phys.*, 1983, vol. 78, issue: 1, pp. 365-372

93. J.Z. Bao, M.L. Swicord, and C.C. Davis, “Microwave dielectric characterization of binary mixtures of water, methanol, and ethanol”, *J. Chem. Phys.*, 1996, vol. 104, issue: 12, pp. 4441-4450

94. P. Petong, R. Potter, and U. Kaatze, “Water-ethanol mixtures at different compositions and temperatures. A dielectric relaxation study”, *Phys. Chem. A*, 2000, vol. 104, issue: 32, pp. 7420-7428

95. Y.Y. Akhadov, “Dielectric properties of binary solutions”, *Pergamon, New York*, 1980

96. J.H. Guo, Y. Luo, A.Augustsson, S. Kashtanov, J.E. Rubensson, D.K. Shuh, H, Angren, and J. Nordgren, “Molecular structure of alcohol-water mixtures”, *Phys. Rev. Lett.*, 2003, vol. 91, issue: 15, art. no. 157401

97. M. K. Kroeger, “Clustering and dielectric behavior of alcohols”, *J. Mol. Liquids*, 1987, vol. 36, issuepp. 101-118

98. H. Frölich, “Theory of Dielectrics”, *Oxford, U.K.*, 1958

99. E.N. Shaforost, A.A. Barannik, N. Klein, S.A. Vitusevich, and A. Offenhaeusser “Nanolitre liquid characterization by open whispering-gallery mode dielectric resonators at millimeter wave frequencies”, *Journal of Applied Physics*, 2008, vol. 104, art. no. 074111

100. R.L. Smith, S.B. Lee, H. Komori, and K. Arai, “Relative permittivity and dielectric relaxation in aqueous alcohol solutions”, *International Symposium on Molecular Thermodynamics and Molecular Simulation, MTMS 97, Tokio*, 1998, vol. 144, issue: 1-2, pp. 315-322

101. K. Heinziger, *Physica B* 1985, vol. 131, pp. 196

102. J.M. Caillol, D. Levesque, and J.J. Weis, “Theoretical calculation of ionic solution properties”, *J.Chem.Phys.*, 1986, vol. 85, issue: 11, pp. 6645-6657

103. J.Anderson, J.Ullo, and S. Yip, “Molecular dynamics simulation of the concentration-dependent dielectric constants of aqueous NaCl solutions”, *Chem.Phys.Lett.*, 1988, vol.152, issue: 6, pp. 447-452

104. S. Chowdhuri, and A. Chandra, “Molecular dynamics simulations of aqueous NaCl and KCl solutions: effects of ion concentration on the single-particle, pair, and collective dynamical properties of ions and water molecules”, *J. Chem Phys.*, 2001, vol. 115, issue: 8, pp. 3732-3741

105. A. Stogryn, “Equations for Calculating the Dielectric Constant of Saline Water (Correspondence)”, *IEEE Trans. Microwave Theory Techn.*, 1971, vol. 19, issue: 8, pp. 733-736

106. L.A. Klein, and C.T. Swift, “An improved model for the dielectric con-stant of sea water at microwaves frequencies”, *IEEE Trans. Antennas Propagat.*, 1977, vol. 25, issue: 1, pp. 104-111

107. K. Nörtemann, J. Hilland, and U. Kaatze “Dielectric properties of aqueous NaCl solutions at microwave frequencies”, *J. Phys. Chem. A*, 1997, vol. 101, issue: 37, pp. 6864-6869

108. T. Meisner, and F. Wentz, “The complex dielectric constant of pure and sea water from microwave satellite observations”, *IEEE Trans. On Geosci. Remote Sens.*, 2004, vol. 43, issue: 29, pp. 1836-1849

109. R. Pethig, and D.B. Kell, “The passive electrical properties of biological systems: their significance in physiology, biophysics and biotechnology”, *Phys. Med. Biol.*, 1987, vol.32, issue: 8, pp. 933-970

110. J.L. Oncley, “Dielectric behavior and atomic structure of serum albumin”, *Biophys.Chem*, 2003, vol. 100, issue: 1-3, pp. 151-158

111. V.V. Meriakri, E.E. Chigrai, D. Kim, I.P. Nikitin, L.I. Pangonis, M.P. Parkhomenko, and J.H. Won, “Dielectric properties of glucose solutions in the millimetre-wave range and control of glucose content in blood”, *Meas.Sci.Technol.*, 2007, vol. 18, issue: 4, pp. 977-982

112. K. Fuchs, and U. Kaatze, “Molecular dynamics of carbohydrate aqueous solutions: dielectric relaxation as a function of glucose and fructose concentration”, *J.Phys.Chem.B*, 2001, vol. 105, issue: 10, pp. 2036-2042

113. A.A Barannik, N.T. Cherpak, Yu.V. Prokopenko, Yu.F. Filipov, E.N. Shaforost, and I.A. Shipilova, “Two-layered disc quasi-optical dielectric resonators: Electrodynamics and applied perspectives for complex permittivity measurement of lossy liquids”, *Meas. Sci. Technol.*, 2007, vol. 18, issue: 7, pp. 2231-2238

114. R. Pethig, “Protein-water interactions determined by dielectric methods”, *Annu.Rev.Phys.Chem.*,1992, vol. 43, pp. 177-205

115. M. Nagel, F. Richter, P. Haring-Bolıvar, and H. Kurz, “A functionalized THz sensor for marker-free DNA analysis”, *Phys Med Biol.*, 2003, vol. 48, issue: 22, pp. 3625-3636

116. B. M. Fischer, M. Walther, and P Uhd Jepsen, “Far-infrared vibrational modes of DNA components studied by terahertz time-domain spectroscopy”, *Phys Med Biol.*, 2002, vol. 47, issue: 21, pp. 3807-3814

117. M. Brucherseifer, M. Nagel, P. Haring Bolivar, and H. Kurz, “Label-free probing of the binding state of DNA by time-domain terahertz sensing”, *Appl. Phys. Lett.*, 2000, vol. 77, issue 24, pp. 4049-4051

118. J.C. Booth, J. Mateu, M. Janezic, J. Baker-Jarvis, and J.A. Beall, “Broadband Permittivity Measurements of Liquid and Biological Samples using Microfluidic Channels”, *IEEE MTT-S International Microwave Symposium Digest*, 2006, vol. 4, pp. 1750-1753

119. G.R. Facer, D.A. Notterman, and L.L. Sohn, “Dielectric spectroscopy for bioanalysis: From 40 Hz to 26.5 GHz in a microfabricated wave guide”, *Appl.Phys.Let.*, 2001, vol. 78, issue 7, pp. 996-998

120. J. Kim, A. Babajanyan, A. Hovsepyan, K. Lee, and B. Friedman, “Microwave dielectric resonator biosensor for aqueous glucose solution”, *Rev. Sc. Instrum.*, 2008, vol. 79, art. no. 086107

121. E.N. Shaforost, N. Klein, A.A. Barannik, S.A. Vitusevich, and N.T. Cherpak “High-sensitivity microwave characterisation of organic molecule solutions of nanolitre volume”, *Appl. Phys. Lett.*, 2009, vol. 94, art. no. 112901

122. J. Liang, F. Kohsaka, T. Matsuo, and T. Ueda, “Wet Etched High Aspect Ratio Microstructures on Quartz for MEMS Applications”, *IEEJ Transactions on Sensors and Micromachines*, 2007, vol. 127, issue: 7, pp. 337-342

123. J. Krupka, R.G. Geyer, M. Kuhn, and J.H. Hinken," Dielectric properties of single crystals of Al2O3 , LaAlO3, NdGaO3, SrTiO3, and MgO at cryogenic temperatures", *IEEE Trans. Micr. Theor. Techn.*, 1994, vol. 42, issue: 10, pp. 1886-1890